Measurement of inclusive Ξ^- and $\Sigma(1385)^{\pm}$ baryon production in neutral current deep inelastic scattering at HERA

Dissertation
zur Erlangung des Doktorgrades
des Fachbereichs Physik
der Universität Hamburg

vorgelegt von
Andy Ziegler
aus Hamburg

Hamburg
2002

Gutachter der Dissertation:	Prof. Dr. E. Lohrmann Prof. Dr. V. Blobel
Gutachter der Disputation:	Prof. Dr. E. Lohrmann Prof. Dr. R. Klanner
Datum der Disputation:	17. Dezember 2002
Vorsitzender des Prüfungsausschusses:	Dr. E. Fretwurst
Vorsitzender des Promotionsausschusses:	Prof. Dr. G. Huber
Dekan des Fachbereichs Physik:	Prof. Dr. F.-W. Büßer

Zusammenfassung

Die Ξ^- und $\Sigma(1385)^{\pm}$ Baryon Produktion in inklusiver tief unelastischer Positron-Proton-Streuung ist mit dem ZEUS Detektor bei HERA gemessen worden. Die für die Messung analysierten Daten entsprechen einer Luminosität von 99 pb^{-1}.

Die Wirkungsquerschnitte für Ξ^- und $\overline{\Xi}^+$ bzw. $\Sigma(1385)^{\pm}$ und $\overline{\Sigma}(1385)^{\mp}$ wurden gemessen, und zwar in einem Bereich der Virtualität des ausgetauschten Photons, Q^2, von $20 < Q^2 < 200$ GeV^2 und in einem beschränkten kinematischen Bereich der Bjorken Skalenvariablen, x, von $3 \cdot 10^{-4} < x < 2 \cdot 10^{-2}$, der Elastizität, y, von $0.04 < y < 0.7$, dem transversalen Impuls, $p_T(\Xi^-)$ bzw. $p_T(\Sigma\,(1385)^{\pm})$, von $1.0 < p_T < 5.0$ GeV und der Pseudorapidität, $\eta(\Xi^-)$ bzw. $\eta(\Sigma\,(1385)^{\pm})$, von $-1.5 < \eta < 1.5$ im Laborsystem. Der gemessene Wirkungsquerschnitt in diesem kinematischen Bereich für Baryon und Antibaryon zusammen ist $\sigma(e^+p \to e^+\Xi^- X) = 85 \pm 7(\text{stat.})^{+13}_{-8}(\text{syst.})$ pb bzw. $\sigma(e^+p \to e^+\Sigma\,(1385)^{\pm} X) = 110 \pm 20(\text{stat.})^{+17}_{-10}(\text{syst.})$ pb. Die Baryon-Antibaryon Paare Ξ^- und $\overline{\Xi}^+$, $\Sigma(1385)^-$ und $\overline{\Sigma}(1385)^+$ sowie $\Sigma(1385)^+$ und $\overline{\Sigma}(1385)^-$ werden zu gleichen Teilen produziert.

Die gemessenen Wirkungsquerschnitte wurden mit drei Monte Carlo Simulationen verglichen, die auf verschiedenen Modellen beruhen, und zwar (1) auf dem Farb-Dipol-Modell (CDM), (2) auf Matrixelementberechnungen der nullten und ersten Ordnung mit darauffolgender Parton Schauer Berechnung (MEPS) und (3) auf dem Monte Carlo Generator HERWIG. Die Fragmentation wird für das CDM und MEPS Monte Carlo mittels JETSET simuliert, das auf dem Lund-String Modell beruht. Die CDM und MEPS Modelle mit dem standardmäßigen JETSET Seltsamkeitsunterdrückungsfaktor ($\gamma_s = 0.3$) überschätzen den gemessenen Ξ^- und $\Sigma(1385)^{\pm}$ Wirkungsquerschnitt. Das HERWIG Monte Carlo überschätzt den Wirkungsquerschnitt sogar noch mehr als das CDM und MEPS Monte Carlo. Auch ein niedrigerer Wert von $\gamma_s = 0.2$ führt nicht zu einer Übereinstimmung mit den gemessenen Daten. Die Parameter $PARJ(4)$ und $PARJ(18)$ von JETSET ändern die Produktionswahrscheinlichkeit von Baryonen in Abhängigkeit des Baryonenspins. Durch die Änderung dieser Parameter ($\gamma_s = 0.2$, $PARJ(4) = 0.025$ und $PARJ(18) = 0.5$) wird eine Übereinstimmung zwischen Monte Carlo und Messung erreicht. Ebenfalls wurde der Einfluss der geänderten Parameter auf die Vorhersage des K^0_S, Λ und $\phi(1020)$ Wirkungsquerschnitts hin untersucht. Das Ergebnis zeigt, das der neue Satz von JETSET Parametern die Messung von Ξ^- und $\Sigma(1385)$ Baryonen beschreibt und auch mit bisherigen Messungen von K^0_S, Λ und $\phi(1020)$ bei HERA übereinstimmt.

Die Form der gemessenen differentiellen Ξ^- bzw. $\Sigma(1385)^{\pm}$ Baryon Wirkungsquerschnitte als Funktion von Q^2, x, η und p_T wurden angemessen von HERWIG, CDM und MEPS reproduziert.

Abstract

The Ξ^- and $\Sigma(1385)^{\pm}$ baryons in inclusive neutral current deep inelastic e^+p scattering have been measured with the ZEUS detector at HERA using an integrated luminosity of 99 pb^{-1}.

Cross sections have been measured for Ξ^- and $\overline{\Xi}^+$ as well as for $\Sigma(1385)^{\pm}$ and $\overline{\Sigma}(1385)^{\mp}$ baryons for photon virtualities, Q^2, in the range of $20 < Q^2 < 200$ GeV^2 and in restricted kinematic regions in the Bjorken scaling variable, x, of $3 \cdot 10^{-4} < x < 2 \cdot 10^{-2}$, elasticity, y, of $0.04 < y < 0.7$, transverse momentum, $p_T(\Xi^-)$ and $p_T(\Sigma\,(1385)^{\pm})$, of $1.0 < p_T < 5.0$ GeV and pseudorapidity, $\eta(\Xi^-)$ and $\eta(\Sigma\,(1385)^{\pm})$, of $-1.5 < \eta < 1.5$, respectively, in the laboratory system. The sum of baryon and anti-baryon cross sections in this restricted kinematic region have been measured to be $\sigma(e^+p \to e^+\Xi^- X) = 85 \pm 7(\text{stat.})^{+13}_{-8}(\text{syst.})$ pb and $\sigma(e^+p \to e^+\Sigma\,(1385)^{\pm}\,X) = 110 \pm 20(\text{stat.})^{+17}_{-10}(\text{syst.})$ pb. Baryons and anti-baryons (Ξ^- and $\overline{\Xi}^+$; $\Sigma(1385)^-$ and $\overline{\Sigma}(1385)^+$ as well as $\Sigma(1385)^+$ and $\overline{\Sigma}(1385)^-$) are produced with equal cross sections.

The measured cross sections have been compared with three Monte Carlo simulations, based on (1) the colour-dipole-model (CDM), on (2) calculations of the zeroth and first order matrix elements complemented by parton shower calculations (MEPS) and on (3) HERWIG. In CDM and MEPS the fragmentation is modelled using JETSET, which is based on the Lund-string model. The CDM and MEPS Monte Carlo models with the default strange-quark suppression factor ($\gamma_s = 0.3$) overestimate the measured Ξ^- and $\Sigma(1385)^{\pm}$ cross sections, while HERWIG overestimates the cross sections even more. Even a lower value of the strangeness suppression factor of $\gamma_s = 0.2$ does not lead to an agreement between experimental data and both CDM and MEPS. The parameters $PARJ(4)$ and $PARJ(18)$ of JETSET set the probability of producing a baryon with a certain spin during fragmentation. The change of these parameters ($\gamma_s = 0.2$, $PARJ(4) = 0.025$ and $PARJ(18) = 0.5$) produces agreement between Monte Carlo and experimental data. Also, the influence of the new set of JETSET parameters on the predicted cross sections of K^0_s, Λ and $\phi(1020)$ production has been investigated and found to be in reasonable agreement with all strange particle measurements at HERA so far.

The shapes of the measured differential Ξ^- and $\Sigma(1385)^{\pm}$ baryon cross sections as a function of Q^2, x, η and p_T are reasonably reproduced by the HERWIG, CDM and MEPS Monte Carlos.

Contents

1 Introduction **1**

2 Introduction to strange baryon production in DIS **5**

2.1 Electron-proton-scattering at HERA 5

2.2 Strange quark production in DIS and fragmentation to hadrons 6

3 Experimental conditions and procedures **9**

3.1 Running conditions 9

3.2 Central tracking detector 10

3.3 Uranium-scintillator calorimeter 11

3.4 Small Angle Rear Tracking Detector 12

3.5 Luminosity Measurement 12

3.6 Trigger 13

3.6.1 General 13

3.6.2 Trigger for DIS 13

4 Offline Analysis **15**

4.1 Event reconstruction 15

4.2 Event selection 16

4.3 Event simulation 17

5 Reconstruction of Ξ^- and $\Sigma(1385)$ baryons **19**

5.1 Λ candidate identification 20

5.2 Identification of Ξ^- baryons with reconstructed displaced tertiary vertices . 24

5.3 Identification of Ξ^- and $\Sigma(1385)$ baryons with primary vertex fitted tracks 36

6 Definition of cross sections and systematic uncertainties 53

7 Inclusive Ξ^- and $\Sigma(1385)$ baryon cross sections in a restricted kinematic region 57

7.1 Total inclusive Ξ^- and $\Sigma(1385)$ baryon cross sections in a restricted kinematic region 57

7.1.1 Total inclusive Ξ^- baryon cross section in a restricted $p_T(\Xi^-)$ and $\eta(\Xi^-)$ kinematic region 57

7.1.2 Total inclusive $\Sigma(1385)$ baryon cross sections in a restricted $p_T(\Sigma\,(1385))$ and $\eta(\Sigma\,(1385))$ kinematic region 58

7.1.3 Comparison of the measurement and prediction of the total inclusive cross sections 59

7.2 Inclusive Ξ^- and $\Sigma(1385)$ baryon cross sections in bins of Q^2, x, p_T and η 65

7.2.1 Inclusive Ξ^- baryon cross sections in bins of Q^2, x, $p_T(\Xi^-)$ and $\eta(\Xi^-)$ 65

7.2.2 Inclusive $\Sigma(1385)$ baryon cross sections in bins of Q^2, x, $p_T(\Sigma\,(1385))$ and $\eta(\Sigma\,(1385))$ 68

7.3 Total Ξ^- and $\Sigma(1385)$ baryon cross section in a range of virtuality of the exchanged photon of $20 < Q^2 < 200$ GeV^2 70

8 Summary and conclusions 71

A Mass distribution $m(\Lambda\pi)$ in bins of Q^2, x, p_T and η 75

A.1 Mass distribution $m(\Lambda\pi)$ with dtv approach in bins of Q^2, x, p_T and η . . . 75

A.2 Mass distribution $m(\Lambda\pi)$ with pvt approach in bins of Q^2, x, p_T and η . . . 75

Chapter 1

Introduction

The hadron-electron-ring-collider HERA offers a unique possibility to investigate the proton structure. The structure function F_2 has been measured with high precision [45] and first measurements of the charm structure function F_2^c exist [39, 18]. Relatively little is known about the strange structure function F_2^s. To complicate matters, the strange sea is not the sole origin of strangeness in positron-proton-scattering (e^+p-scattering). A non-negligible amount of strange quarks appears in fragmentation, which is a transformation of quarks and gluons to colourless hadrons in the non-perturbative region of QCD. This soft process cannot be calculated perturbatively and has to be simulated using phenomenological fragmentation models. Thus, any conclusions about the origin of strange quarks requires a well developed model of fragmentation.

A successful model describing the fragmentation is the Lund string fragmentation [3] which is implemented in the JETSET program [36]. This model defines the probabilities P_s, P_u and P_d of creating s, u and d quarks, respectively, in the colour field during the fragmentation process. These probabilities are connected with the mass of the quarks. Since u and d quarks have nearly the same mass compared with the mass of a strange quark, the probability of creating a light quark (u and d) is assumed to be equal: $P_u = P_d$. A central variable of the Lund string model which concerns the strange quark production is the strangeness suppression factor, γ_s, defined by $\gamma_s = P_s/P_u$. The value $\gamma_s = 0.3$ was found by LEP experiments [2, 16] and is normally used as a default parameter in the model. However, measurements of strange particles at the e^+e^- collider LEP are not all consistent. OPAL concludes [33, 32] that the default value is too high to accommodate their measurements.

Strange particle production has been studied at HERA using the same fragmentation model. The K^0 mesons and Λ baryons[1] have been measured in deep inelastic scattering (DIS) [43, 20] and photoproduction [19, 42]. The production of $\phi(1020)$ mesons, which have strangeness zero, but are a nearly pure $s\overline{s}$ state, has been measured at HERA [14]

[1] In the following when a particle (or particle decay) is mentioned the anti-particle (or anti-particle decay) is also meant unless explicitly stated.

too. The results of these measurements, and their contribution to the understanding of strange quark production in the fragmentation, are reviewed shortly.

The *Neutral strange particle production in deep inelastic scattering at HERA* has been studied by the ZEUS Collaboration [43]. This publication presents measurements of K^0 meson and Λ baryon production in the kinematic range $10 < Q^2 < 640$ GeV^2, $0.0003 < x < 0.01$ and $y > 0.04$. The kinematic region of the K^0 and Λ is restricted to $p_T > 0.5$ GeV and $|\eta| < 1.3$. The K^0 and Λ multiplicity and their momentum and angular distributions in the kinematic region are compared to Monte Carlo models based on the results of lower energy experiments. The differential K^0 and Λ multiplicity as a function of p_T and η are compared to predictions of the colour-dipole-model (CDM) [5] and first order matrix elements complemented by parton shower calculations (MEPS). The CDM was generated with JETSET [36] for different strangeness suppression factors: the default values, $\gamma_s = 0.3$, which predicts a multiplicity higher than the measured one, and with a smaller suppression factor, $\gamma_s = 0.2$, which reduces the predicted K^0 and Λ multiplicity to a value closer to that observed in the data (Tab. 1.1). The measured shapes are reasonably described by both parameters. In addition the mean K^0 multiplicity and the ratio of K^0 to charged particle multiplicity $N(K^0)/N(\text{tracks})$ as a function of the Q^2 of the event is measured, from which it is concluded that the mean K^0 multiplicity shows no Q^2 dependence at fixed centre-of-mass energy of the virtual photon-proton system.

	$N(K^0)$/event	$N(\Lambda)$/event
Data	$0.289 \pm 0.015 \pm 0.014$	$0.038 \pm 0.006 \pm 0.002$
CDM		
with $\gamma_s = 0.3$	0.342 ± 0.005	0.066 ± 0.003
with $\gamma_s = 0.2$	0.264 ± 0.003	0.050 ± 0.002

Table 1.1: Results [43] of the K^0 and Λ measurement for events with $10 < Q^2 < 640$ GeV^2, $0.0003 < x < 0.01$, $y > 0.04$ and for K^0 with $0.5 < p_T(K^0) < 4.0$ GeV and $|\eta(K^0)| < 1.3$ and for Λ with $0.5 < p_T(\Lambda) < 3.5$ GeV and $|\eta(\Lambda)| < 1.3$. The two CDM samples have been generated with a different strangeness suppression factor γ_s.

Strangeness production in deep-inelastic positron-proton scattering at HERA has been investigated by the H1 Collaboration [20]. K^0 meson and Λ baryon production are measured in the kinematic range $10 < Q^2 < 70$ GeV^2, $10^{-4} < x < 10^{-2}$, $0.05 < y < 0.6$, $0.25 < p_T^2 < 4.5$ GeV^2 and $|\eta| < 1.3$. Comparisons are made with Monte Carlo predictions using JETSET with the default strangeness suppression parameter, $\gamma_s = 0.3$, a reduced parameter, $\gamma_s = 0.2$, and the set of parameters extracted by the DELPHI Collaboration: one of it is $\gamma_s = 0.23$. The measured multiplicity in bins of η and p_T^2 is significantly better described by the DELPHI parameters and by $\gamma_s = 0.2$. The mean number of K^0 mesons observed per event is measured as a function of x in three Q^2 regions. No evidence of any systematic deviation as a function of either Q^2 or x between data and the Monte Carlo predictions are seen. The observed ratio of the number of K^0 mesons produced to the number of charged particle multiplicity in bins of Q^2 shows a better agreement with the

DELPHI than with the default parameters. These results are directly comparable with the measurements of the ZEUS Collaboration described above. Both sets of data are in reasonable agreement.

The photoproduction of K^0 mesons with $p_T(K^0) > 0.5$ GeV and $|\eta(K^0)| < 1.5$ has been measured [42] for events in the photon-proton centre of mass energy range $134 < W < 277$ GeV with at least one reconstructed jet with an energy $E_T(\text{jet}) > 8$ GeV and $|\eta(\text{jet})| < 0.5$. The differential $p_T(K^0)$ distribution that was measured cannot distinguish between the Monte Carlo predictions using JETSET with $\gamma_s = 0.3$ and $\gamma_s = 0.2$. The differential $\eta(K^0)$ distribution shows that for $\eta(K^0) < 0.5$ the data are in agreement with the reduced value of γ_s. However, at higher $\eta(K^0)$ a tendency of the Monte Carlo to be too low compared with the data is worsened with the reduced suppression factor.

Inclusive K^0 and Λ photoproduction has been investigated at HERA by the H1 Collaboration [19] at an average photon-proton centre of mass energy of 200 GeV in the transverse momentum range $0.5 < p_T < 5$ GeV. The measured K^0 and Λ cross section in bins of p_T and η are compared to Monte Carlo predictions using JETSET with the standard setting, $\gamma_s = 0.3$, as well as a reduced strangeness suppression parameter, $\gamma_s \simeq 0.2$. The measured K^0 meson cross section is in reasonable agreement with the Monte Carlo prediction using the lower setting, whereas the default prediction overestimates the cross sections. However, the measured Λ baryon cross section lies significantly above the Monte Carlo prediction for both parameter setting. A comparison to DIS shows that photoproduction and DIS rates are compatible in a region where expected.

The *Inclusive $\phi(1020)$-meson production in neutral current deep inelastic scattering at HERA* has been studied by the ZEUS Collaboration [14]. The ϕ state is a nearly pure $s\overline{s}$ state and due to its two strange quarks, it is more sensitive to the presence of strange quarks in the hard scattering than particles containing only one strange quark like K^0 and Λ. The selected events are in the kinematic range of $10 < Q^2 < 100$ GeV^2, $0.0002 < x < 0.01$, $0.04 < y < 0.95$ and the kinematic region for the ϕ mesons is restricted to $1.7 < p_T(\phi) < 7$ GeV and $-1.7 < \eta(\phi) < 1.6$. The measured cross section in this region is lower than the predicted by the default JETSET suppression factor $\gamma_s = 0.3$ but very well described by $\gamma_s = 0.22$. The shapes of the cross sections for $p_T(\phi)$ and Q^2 are reasonable reproduced while significant differences exist for the $\eta(\phi)$ and $x_p(\phi) = 2|\vec{p}(\phi)|/Q$ distributions. In addition this measurement indicates the presence of the strange sea contribution at HERA as well as for the first time in the kinematic region $x < 0.006$.

Although the Lund string fragmentation model is quite successful this review shows that the Lund fragmentation model as implemented in JETSET does not satisfy the measurements of strange quark production with the default setting. All measurements of particles with strange quarks — except the cross section measurement of Λ baryons in photoproduction by H1 — have shown that the default strangeness suppression parameter is generally too high and a value of $\gamma_s \approx 0.2$ is preferred. However, it should be kept in mind, that the strangeness suppression factor is not the sole parameter which tunes the fragmentation. More parameters exist which e.g. set the rate of meson and baryon production depending

on the spin of the final particle.

This thesis describes the measurement of inclusive Ξ^- and $\Sigma(1385)$ baryon production in e^+p neutral current deep inelastic scattering at HERA with the ZEUS detector. Since Λ baryon production has so far been the only measurement of strange baryons at HERA this analysis is a further test of the Lund string fragmentation model for baryons as well as for the strangeness suppression factor. Also both Ξ^- and $\Sigma(1385)$ baryons provide features different from Λ baryon production:

- The strongly decaying resonance $\Sigma(1385)$ has spin 3/2. The previous measured Λ baryon has spin 1/2.
- The Ξ^- baryon is a weakly decaying particle with spin 1/2 and contains two strange quarks. Therefore it is much more sensitive to the production of strange quarks.

It will be interesting to see if a strangeness suppression factor of $\gamma_s \simeq 0.2$ predicts a correct cross section simultaneously for Ξ^- and $\Sigma(1385)$ baryon production, because the two particles differ in two interesting features: spin and strangeness. The simultaneous measurement of Ξ^- and $\Sigma(1385)$ will answer the question, if the spin of baryons produced during fragmentation is simulated properly. In addition the Ξ^- is more sensitive to the strangeness suppression factor than all other particles measured so far, because it contains two strange quarks.

Chapter 2

Introduction to strange baryon production in DIS

2.1 Electron-proton-scattering at HERA

Electron-proton-scattering[1] can be described by an exchange of a gauge boson (γ, Z^0, $W^{\pm}$)[2]. Depending on the charge of the exchanged boson the interaction is called neutral or charged current scattering.

Three independent Lorentz invariant quantities are sufficient for determining the kinematics in inclusive electron-proton-scattering, $ep \to e'X$, where the hadronic final state, X, is not specified. The electron-proton centre-of-mass energy $\sqrt{s}$ is fixed by the beam energies of the HERA collider. The other two independent quantities can be chosen out of the following: the virtuality, Q^2, of the gauge boson, which is the negative square of the momentum transfer, q, and the dimensionless scalar variables x and y. These quantities are defined as

$$\begin{aligned} s &= (p_p + p_e)^2 \\ Q^2 = -q^2 &= -(p_e - p_{e'})^2 \\ x &= Q^2/2p_p q \\ y &= p_p q / p_p p_e \end{aligned}$$

The four-vectors of the incoming proton, the incoming electron and the scattered electron are denoted p_p, p_e and $p_{e'}$, respectively.

The quantities x and y have a clear meaning in the quark-parton-model (QPM) [11]. In this model the proton consists of pointlike objects which are called partons. Then x is the fraction of the momentum of the parton involved in the collision compared to the momentum of the proton, and the relative energy loss of the electron in the rest frame of

[1] All described aspects of the electron-proton scattering are valid for positron-proton scattering as well.
[2] An introduction to HERA physics can be found elsewhere [38].

the proton corresponds to y. The quantities x and y are related by

$$Q^2 = x \cdot y \cdot s$$

if the masses of the proton and electron are neglected.

The virtuality can be used to separate the electron-proton-scattering into two regions. Interactions with a low virtuality ($Q^2 \approx 0$) are called photoproduction, the other region is called deep inelastic scattering (DIS) and includes all events with $Q^2 \gg 1$ GeV^2. Since the latter region is selected for this analysis, the kinematics and processes in the deep inelastic scattering are described in more detail.

Neutral current DIS events are characterised by the scattered electron, which has to be identified by the experiment to determine the kinematic quantities. Also, it allows DIS and photoproduction events to be distinguished by calculating the quantity

$$E - P_Z,$$

where (E, P_X, P_Y, P_Z) is the four-vector of the sum of all particles in the hadronic final state. For the proton, the energy and momentum contribution in the Z-direction are nearly equal in size and sign. Thus, the electron contributes most to this observable. In neutral current DIS events this quantity has to be $E - P_Z \approx 55$ GeV while events from photoproduction peak far below 30 GeV.

The proton structure can be parameterised by the structure functions $F_i(x, Q^2)$, which represent the densities of partons in the nucleon found at given values of x and Q^2. The double differential cross section is given by

$$\frac{d^2\sigma}{dxdQ^2} = \frac{4\pi\alpha^2}{xQ^4}\left[xy^2F_1 + (1-y)F_2\right],$$

where α is the fine structure constant. The structure of the proton is relatively well determined and parameterised by several parton distribution functions (PDFs) [26, 17, 30, 31].

2.2 Strange quark production in DIS and fragmentation to hadrons

The aim of this analysis is the measurement of the production of the strange baryons Ξ^- and $\Sigma(1385)$. The observation of strangeness in the final state of neutral current DIS raises the question of its origin. Possible sources are:

- Flavour excitation. Inside the proton the gluons, g, can fluctuate into quark-antiquark pairs. After a fluctuation of a $g \to s\bar{s}$, one of the strange quarks could receive a large momentum transfer by the exchanged photon so that the pair cannot recombine. This hit quark leaves the proton remnant, and it fragments (Fig. 2.1(a)).

- Boson-gluon fusion (BGF). A gluon of the proton couples with the exchanged photon via a virtual strange-antistrange quark (Fig. 2.1(b)).
- Fragmentation. If strange quarks arise during fragmentation, the quarks are not directly involved in the hard scattering process but emerge from gluon splitting in the parton shower (Figs. 2.1(a)–(b))
- Decays of heavier quarks. Strange quarks in the final state can result from decays of charm quarks which themselves can come from a decayed beauty quark. This contribution can be neglected because the cross section for light quark production in DIS is much higher than the cross section to produce the heavier charm and beauty quarks in DIS due to their higher masses [40].

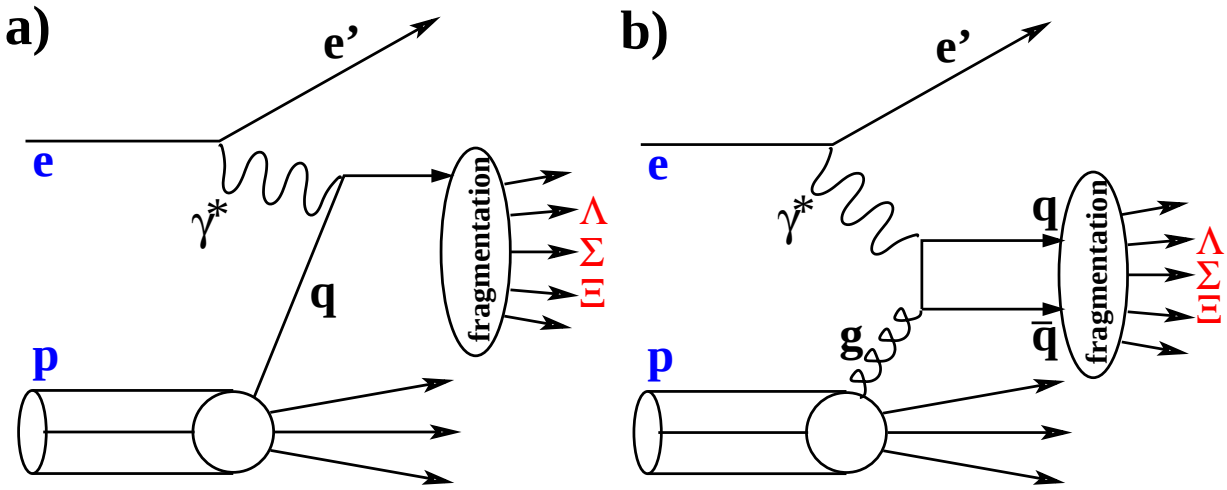

Figure 2.1: Origin of strange quarks in DIS which can build a strange baryon (e.g. Λ, Ξ^- or $\Sigma(1385)$): (a) a quark, q, in the proton receives a large momentum transfer according to QPM or (b) a quark-antiquark pair, $q\overline{q}$, emerges from the BGF process. The strangeness in the final state can have its origin in the hard process if the quark, q, is a strange quark, $q = s$, or in the fragmentation.

Independent of the origin of the strange quark it has to fragment into hadrons. In the non-perturbative region of QCD the transformation of quarks and gluons to colourless hadrons is not calculable but must be simulated using fragmentation models. A successful model which describes the fragmentation process to mesons and baryons is the Lund string scheme [3, 4]. Meson production can be modelled by an iterative approach[3] starting from the given initial quark q_0. It is assumed that a new $q_1\bar{q}_1$ pair may be created forming a meson $q_0\bar{q}_1$ and leaving q_1 behind. The Lund model uses the idea of quantum mechanical tunneling in

[3]This iterative approach is used in the Monte Carlo program JETSET [3] which models the fragmentation process based on the Lund string scheme. Since this program is used later the fragmentation is explained using this iterative approach.

such a way that the generated $q_i\bar{q}_i$ quark pair leads to the breakup of a string. The basic idea is that both generated quarks are created at the same point but then tunnel into the classically allowed region with a certain distance. The further fragmentation follows the same procedure for the quark q_1 which is left behind after the first step of the iteration.

Parameters that are necessary for this iterative process are

1. the probability to produce the various possible combinations of $q_i\bar{q}_i$ quark pairs like $u\bar{u}$, $d\bar{d}$, $s\bar{s}$ etc. and
2. the probabilities to form a specific meson out of a given $q_{i-1}\bar{q}_i$ quark pair.

The first parameter is important for the production of strangeness because it sets the rate of strange quark production in the simulated fragmentation. The ratios of $q_i\bar{q}_i$ quark pair production can be estimated using a model estimate, which depends on the quark pair mass that is produced. The relative suppression ratios for the flavours u, d, s and c are estimated to be $u : d : s : c \approx 1 : 1 : 0.3 : 10^{-11}$. Charm and heavier quarks are not expected to be produced in the soft fragmentation. Since the suppression of $s\bar{s}$ production cannot be calculated perturbatively, it remains as a free phenomenological parameter with $u\bar{u} : d\bar{d} : s\bar{s} = 1 : 1 : \gamma_s$ with the strangeness suppression factor, γ_s. In the Lund model, the baryon production is modelled in a general framework called "popcorn" model [4], in which baryons appear from the successive production of several $q_i\bar{q}_i$ pairs.

Chapter 3

Experimental conditions and procedures

3.1 Running conditions

The data for this analysis were collected at the positron-proton collider HERA using the ZEUS detector. HERA collided 27.5 GeV positrons and 820 GeV (920 GeV) protons during the 1996 to 1997 (1999 to 2000) running periods. The positron-proton centre-of-mass energy, $\sqrt{s}$, of the collision was $\sqrt{s} = 300$ GeV (318 GeV). This measurement is based on an accumulated Luminosity, $\mathcal{L}$, of $\mathcal{L} = 39.0 \pm 0.5$ pb^{-1} (60 ± 1 pb^{-1}).

ZEUS is a multipurpose detector which is described in detail elsewhere [46]. The ZEUS coordinate system is a right-handed Cartesian system, with the Z axis pointing in the proton beam direction, and the X axis pointing towards the centre of HERA. The coordinate origin is at the nominal interaction point. The polar angle θ is defined with respect to the positive Z-direction. The pseudorapidity, η, is given by $-\ln(\tan\frac{\theta}{2})$. The key components for this analysis are

1. the central tracking detector, which measures the momentum of charged particles in a magnetic field of 1.43 T,

2. the uranium-scintillator calorimeter, which measures the energy of the particles in the final state,

3. the small angle rear tracking detector, which allows the position of the scattered electron close to the positron beam direction to be determined with a higher precision than the calorimeter and

4. the luminosity monitoring system, which allows the luminosity to be determined.

These components are introduced in more detail in the following sections.

3.2 Central tracking detector

The major component of importance to this analysis is the central tracking detector (CTD). The CTD is designed for charged particle detection and consists of a cylindrical drift chamber with nine superlayers (SL), each provided with a cell of eight sense wire layers. The magnetic field is perpendicular to the electric field and the cells are inclined at an angle of 45° with respect to the radial direction. Five of the superlayers have wires parallel to the chamber axis[1], and four SL possess wires which have a small stereo angle[2] of 5°. The stereo angle is chosen in such a way that the angular resolution in polar and azimuthal angles are roughly equal and the Z-position of a track can be reconstructed with an accuracy of about 2 mm. An additional Z-by-timing (ZbyT) system allows the Z-position to be calculated with a resolution of 4.4 cm [7]. For the ZbyT system both ends of the wires are read out and the Z-position is determined from the difference in the arrival time of the pulses at the two ends [46]. The resolution of the transverse momentum of a track traversing all CTD layers is $\sigma(p_T)/p_T = 0.0058p_T \oplus 0.0065 \oplus 0.0014/p_T$ with p_T being the track transverse momentum (in GeV) [21]. The CTD is filled with a gas mixture of argon, carbon dioxide and ethane.

A charged particle crossing the CTD creates primary ionisation electrons by interacting with the gas and ionises it. The electrons are accelerated along a drift path that results from the electric and magnetic field in the chamber. The high-voltage level, the gas mixture and the diameter of the sense wires were chosen such that the drift cells operate as proportional counters. The spatial coordinate (hit) is calculated from the arrival time of the signal pulse and the time-to-distance relationship given by the drift velocity. An ambiguity is introduced as to which side of the wire the hit originated from by the unknown drift direction of the primary ionisation electrons, only the absolute value of the drift time is known. Straight tracks from the interaction point have to cross at least one cell boundary within a superlayer since the cell is tilted by 45°. This feature almost always resolves the ambiguity when looking for a track segment in one superlayer.

The reconstruction of tracks and secondary vertices is described in detail elsewhere [22, 23]. For this analysis the reconstruction of tracks using only CTD hits is important since the combined use of CTD and other tracking detectors requires a good knowledge of their relative alignments, multiple scattering at the components boundaries, etc. which is not given. The routine to reconstruct CTD-only tracks is explained at length in its central points now. First an arc in the XY plane is reconstructed. A track „seed“ in an outer part of the CTD is the beginning of each track candidate. Three CTD hits from an axial superlayer are taken to be this seed and a broad virtual hit is added at the beam line ($X = Y = 0$) to help guide the trajectory inward. The track seed is extrapolated inward and additional hits are gathered with increasing precision as the trajectory parameters are updated. Once the trajectory spans several axial superlayers, only the innermost three

[1] These superlayers are called „axial superlayers“.
[2] These superlayers are called „stereo superlayers“.

superlayers are used for further extrapolation. This accommodates curvature variation resulting from magnetic field inhomogeneity inside the CTD volume.

The arc that is found in the XY plane is superimposed by an appropriate Z intercept and $\cot\theta$ slope. If a trajectory is already pinned on either side by axial hits eligible stereo superlayers are generally traversed. Another way to determine the missing two parameters can be done if the candidate has ZbyT measurements.

The important pass of the described pattern recognition accepts only the tracks that are successfully continued all the way down to SL 1. The longest tracks are found first and the process is repeated until the short SL 1 tracks are sought.

A 5 parameter helix model is fitted to each track candidate. The trajectory fit begins by first estimating a momentum based on the slope and curvature provided by the pattern recognitions described above. Then a trajectory is established by swimming through the magnetic field, starting from the innermost measured hit. Finally, the trajectory and its covariance matrix is extrapolated inward to perigee with the Z axis at $X = Y = 0$.

The tracks which were found can either come from the primary vertex or secondary vertices. Secondary vertices can either result from decays such as $\Lambda \to p + \pi^-$ or nuclear collisions by tracks in material such as the beampipe. To distinguish between tracks from the primary vertex and secondary vertices all reconstructed tracks of an event are used for a vertex finding procedure.

The procedure only uses tracks which have hits in SL 1 but need not be compatible with the beamline. Then, each pair of tracks which pass this requirement is tested for loose compatibility with forming a common vertex. The track pairs that are found are used to form track "clusters" which consists of tracks that are loosely consistent with a common vertex. A simple vertex fit is used to drop tracks until the vertex chi-square is acceptable. At least two tracks have to survive in one cluster, otherwise it dies. Each surviving cluster is a potential secondary vertex candidate and is used in the next stage.

Every single track which has at least hits in SL 1 is given an opportunity to "seed" a primary vertex candidate. Then this primary vertex candidate and all the secondary candidates are analysed together as a group and a "score" is evaluated. The primary vertex seed with the highest score is taken and put into the full vertex fit. This nonlinear iteration does not only solve for the final vertex position but also constrains the remaining trajectories to it.

3.3 Uranium-scintillator calorimeter

The uranium-scintillator calorimeter (CAL) is a compensation calorimeter that surrounds the CTD. It is divided into three parts, forward (FCAL), barrel (BCAL) and rear calorimeter (RCAL). The coverage is nearly hermetic (99.8% in forward and 99.5% in backward section). The calorimeter is longitudinally segmented into electromagnetic (EMC) and hadronic (HAD) sections. The energy resolution of the CAL under test beam conditions is $\sigma_E/E = 0.18/\sqrt{E}$ for electrons and $\sigma_E/E = 0.35/\sqrt{E}$ for hadrons (with E in GeV).

3.4 Small Angle Rear Tracking Detector

The small angle rear tracking detector (SRTD) [8] is a polystyrene scintillator strip detector. This component is designed to measure the impact position of the scattered electron and can be used for energy corrections in the rear direction. It covers the angular region between the rear tracking detector and the beampipe. The scintillator strips are arranged in two planes of four 24 cm $\times$ 44 cm quadrants each. The position of the scattered lepton position can be measured with a resolution of 3 mm.

3.5 Luminosity Measurement

The luminosity, $\mathcal{L}$, of a collider, the event rate per second, R, and the cross section, σ, are connected by the relation

$$R = \mathcal{L} \cdot \sigma \tag{3.1}$$

The value of the luminosity depends on the parameters of the beam and collider and can be calculated from these. Also, the luminosity can be determined by using a well known process and applying Eq. 3.1. At ZEUS, the luminosity is measured using bremsstrahlung and Eq. 3.1.

The electron radiates a high energy photon in the electromagnetic field of the proton. From the interaction point (IP), the bremsstrahlung photon and electron emerge at very small angles with respect to the incident electron direction. The spectra of the photon and electron can be described well by the Bethe-Heitler formula [10].

Since the photon and electron emerge at very small angles, both propagate inside the proton beam pipe. At about 80 m from the IP the photons can leave the pipe because the proton beam pipe is bent upwards. The off-beam energy electrons are deflected out of the beam pipe by a magnet and can leave the pipe at some distance from the IP. The exit window for the photons is installed at $Z = -92.5$ m, the position for the photon detector is at $Z = -107$ m. A detailed description of the luminosity measurement can be found elsewhere [6].

The luminosity is measured using the photon only. The photons cross a copper-beryllium window with $0.095X_0$ ($X_0 \equiv$ radiation length) thickness, then a 12.7 m long vacuum pipe, which ends at an absorber that shields against the large flux of direct synchrotron radiation. It is made out of a $2X_0$ carbon block. The photons are detected by a lead-scintillator sampling calorimeter which also measures the shower position. The transverse dimensions of the calorimeter are 18 cm $\times$ 18 cm and the depth is $22X_0$. The relative energy resolution is about $20\%/\sqrt{E\,(\mathrm{GeV})}$.

The luminosity can be measured with an uncertainty of about 1% which is dominated by the acceptance uncertainty.

3.6 Trigger

3.6.1 General

The online trigger system is designed to identify interesting physics events (DIS, photoproduction, etc.) which give an insight to HERA physics and suppress background-induced events efficiently. The total rate of interaction (about 10–100 kHz), dominated by proton-beam background interactions with the residual gas, is reduced by a three level trigger system to an output rate of ~ 5 Hz. The first level trigger (FLT) is a hardware trigger with an output rate below 1 kHz. A programmable transputer network builds the second level trigger (SLT). More sophisticated algorithms can be used to reject background events. The rate has to be kept below 100 Hz. Events which pass the third level trigger (TLT) are written to tape and available for offline reconstruction and this analysis.

3.6.2 Trigger for DIS

The DIS trigger selection is based on a chain which is well understood and simulated for Monte Carlo events.

On the first level trigger it was required that at least one of the following requirements was fulfilled:

- the total energy in the electromagnetic sections of the CAL had to be greater than 15 GeV,
- an isolated electron was identified in FCAL or BCAL; in addition, a track had been found in the CTD,
- an isolated electron was found in the RCAL; in addition, more than 2 GeV had to be found in the EMC section of RCAL,
- the total transverse energy was greater than 18 GeV,
- the total transverse energy was greater than 12 GeV and at least one track must have been found in the CTD,
- a track was found and the energy in the EMC section of RCAL was greater than 3.4 GeV or greater than 4.8 GeV in the EMC section of BCAL or
- a signal in SRTD and a track was found.

At the second level trigger, two requirements had to be fulfilled:

- more than 2.5 GeV in the EMC of RCAL or BCAL or more than 10 GeV in the hadronic or EMC section of FCAL or
- $E - P_Z + 2 * E_{lumi,\gamma} > 29$ GeV, where $E - P_Z = \sum E_i(1 - \cos\theta_i)$, E_i is the energy of the ith calorimeter cell, θ_i its polar angle and the sum runs over all cells and $E_{lumi,\gamma}$ is the energy deposited in the photon calorimeter of the luminosity monitor system.

For the third level trigger it is required that the DIS03 bit fired. That means:

- one of the available electron finders found a positron with an energy above 4 GeV,
- the incident point of the positron on the CAL was farther away from the beampipe than 26 cm (36 cm) in running period 1995–1997 (1999–2000) and
- $E - P_Z > 30$ GeV.

Chapter 4

Offline Analysis

4.1 Event reconstruction

The detector components that are necessary to select neutral current DIS events are the SRTD, CAL and CTD. The SRTD is used to determine the impact position of the scattered positron. The CAL measures the hadronic final state and the energy of the scattered positron as well as the impact position if outside of the fiducial volume of the SRTD. The CTD provides the positron track and the position of the primary vertex.

Neutral current DIS events are characterised by their scattered electron which has to be detected to determine the kinematic variables. This analysis uses the electron finder SINISTRA [1] which uses clusters of energy depositions, the ratio of deposited energy in the electromagnetic and hadronic sections of the calorimeter and the shower profile to determine the best electron candidate. The optimisation of the identification is done with a neural network.

Three reconstruction methods exist to reconstruct the kinematic variables Q^2, x and y:

- the electron method (this method is specified with the subscript e) only uses measurements of the energy, $E_{e'}$, and polar angle, θ, of the scattered positron. The quantities are given as

$$\begin{aligned} Q_e^2 &= 2E_e E_{e'}(1+\cos\theta) \\ x_e &= \frac{E_e}{E_p}\frac{E_{e'}(1+\cos\theta)}{2E_e - E_{e'}(1-\cos\theta)}, \\ y_e &= 1 - \frac{E_{e'}}{2E_e}(1-\cos\theta). \end{aligned}$$

- the double angle (DA) method [9] is based on the angles of the scattered positron, θ, and of the hadronic angle, γ, which is defined as

$$\cos\gamma = \frac{\left(\sum_h p_{xh}\right)^2 + \left(\sum_h p_{yh}\right)^2 - \left[\sum_h (E_h - p_{zh})\right]^2}{\left(\sum_h p_{xh}\right)^2 + \left(\sum_h p_{yh}\right)^2 + \left[\sum_h (E_h - p_{zh})\right]^2}$$

where $\sum_h$ is the sum over all „hadronic“ calorimeter cells, h, (i.e. the calorimeter cells belonging to the scattered positron are not taken into account) with four-momentum $(E_h, p_{xh}, p_{yh}, p_{zh})$. The kinematics can be obtained from

$$\begin{aligned} Q^2_{DA} &= 4E_e^2 \frac{\sin\gamma(1+\cos\theta)}{\sin\gamma+\sin\theta-\sin(\theta+\gamma)}, \\ x_{DA} &= \frac{E_e}{E_p}\frac{\sin\gamma+\sin\theta+\sin(\theta+\gamma)}{\sin\gamma+\sin\theta-\sin(\theta+\gamma)}, \\ y_{DA} &= \frac{\sin\theta(1-\cos\gamma)}{\sin\gamma+\sin\theta-\sin(\theta+\gamma)}. \end{aligned}$$

- the Jacquet-Blondel (JB) method [12] relies entirely on measurements of the hadronic system:

  $$y_{JB} = \frac{\sum_h (E_h - p_{zh})}{2E_e}.$$

  For low y_{JB} ($y_{JB} < 0.05$) the resolution is much better than with the electron method. However the resolution of Q^2_{JB} and x_{JB} is always worse than Q^2_e and x_e, respectively, thus Q^2_{JB} and x_{JB} are not used in this analysis.

4.2 Event selection

The following requirements are selected to filter out DIS events:

- $E_{e'} > 10$ GeV, where $E_{e'}$ is the corrected energy of the scattered positron in the calorimeter,
- $20 < Q^2_e < 200$ GeV^2,
- $3 \cdot 10^{-4} < x_e < 2 \cdot 10^{-2}$,
- $y_e < 0.7$,
- $y_{JB} > 0.04$,
- $41 < E - P_Z < 60$ GeV,
- a primary vertex position in the range $|Z_{vertex}| < 50$ cm,
- the impact point (X, Y) of the scattered positron on the calorimeter has a distance to the beam line of $r_e > 26$ cm (36 cm) for the 1996 to 1997 (1999 to 2000) period.

The reconstruction of the Q^2 and x variables was performed using the electron method, since it has the best energy resolution at the relatively low Q^2 values used in this thesis [14].

These cuts are fulfilled by 2214189 events.

4.3 Event simulation

The data are compared to various leading-order Monte Carlo (MC) models which generate the entire hadronic final state in neutral current DIS events. The MC simulation is performed in two steps: first the primary scattering process at the parton level is simulated by an event generator. The final state particles are obtained by using a fragmentation model. Also strong and electromagnetic decays which happen at the primary vertex are simulated at this stage. The list of all four-vectors which exist at this level are then passed through a full simulation of the detector using GEANT 3.13 [13]. Here the decay of long-lived particles and the detector response to the event is simulated.

Event generators factor the scattering of an electron off a proton into different subprocesses: initial and final state radiation, hard sub-process and fragmentation. The perturbation theory allows that the hard process can directly be computed from the matrix elements while the radiation of other partons is limited by the scale Q^2. The fragmentation process models the conversion of partons carrying colour to final state hadrons. fragmentation models are determined phenomenologically like the Lund string model (chapter 2.2).

The used MC generators are based on the parton-cascade approach to incorporate higher-order QCD effects followed by a fragmentation to hadrons. Events were generated with LEPTO 6.5 [24] and ARIADNE 4.07 [27], both interfaced with HERACLES 4.5.2 [25] in order to incorporate first-order electroweak corrections in the frame of DJANGOH [37]. Also, HERWIG 6.1 [29, 15] was used to simulate electron-proton scattering. The parton density functions were taken from the CTEQ5D set [26]. LEPTO calculates the zeroth and first order matrix elements for inclusive DIS, complemented by parton shower calculations (MEPS). ARIADNE bases on the colour-dipole-model [5] and does not divide the QCD cascade in an initial and final state. It assumes that all gluon radiation can be described as gluon radiation from the colour dipole only. Both programs use the Lund string model as implemented in JETSET 7.4 to simulate the fragmentation of the partons. HERWIG does not include QED radiative corrections and uses a low-mass cluster fragmentation model [28] which forms colour-singlet clusters after the perturbative phase of jet development and then decay into the observed hadrons.

The Boson-gluon fusion process (BGF) is included in the calculations of ARIADNE. In HERWIG the BGF is implemented indirectly, i.e. the gluon and quark ladder, which is simulated by HERWIG, can lead to a Feynman graph that is similar to the graph of the BGF process.

Since ARIADNE provides the best description of the observed hadronic final state in inclusive DIS [41], events generated with DJANGOH interfaced with ARIADNE and HERACLES were passed through the full event simulation. In order to save disk space and computing time only events with at least one Ξ^- and $\Sigma(1385)$ in the central region of the detector with pseudorapidity, η, restricted to $|\eta| < 1.75$ were fully processed and build the so called Ξ– and Σ–MC, respectively.

As a second MC for systematic checks HERWIG is chosen. Since HERWIG does not

contain the Breit-Wigner distribution and therefore does not model the natural width of strongly decaying particles like $\Sigma(1385)$ correctly, only a Ξ–MC generated with HERWIG is passed through the full simulation.

In addition DJANGOH interfaced with LEPTO and ARIADNE was used to generate events with different parameter setting concerning JETSET at the hard process level only.

Since data from the running periods with a proton energy of 820 GeV and 920 GeV are combined to one sample, all MC samples consist of two subsamples generated with a proton energy of 820 GeV and 920 GeV. These subsamples are weighted with the data luminosity and added to one sample which is compared to the data.

The same reconstruction program as that used for the ZEUS data was selected to process the fully simulated events.

Chapter 5

Reconstruction of Ξ^- and $\Sigma(1385)$ baryons

The baryonic state Ξ^- has quark content dss, and the charge conjugated (c.c.) state is $\overline{\Xi}^+$. The Ξ^- is a weakly decaying particle with a lifetime, τ, of $\tau = 1.64 \pm 0.02 \cdot 10^{-10}$ s [34]. The main decay channel is $\Xi^- \to \Lambda + \pi^-$ with a branching ratio, Br, of $Br = 99.89 \pm 0.04\%$ [34]. In the following, when the baryon Ξ^- is mentioned the anti-baryon $\overline{\Xi}^+$ is also meant unless explicitly stated.

The baryonic state $\Sigma(1385)$ includes the charged resonance $\Sigma(1385)^+$ with quark content uus, the neutral $\Sigma(1385)^0$ with quark content uds, the charged $\Sigma(1385)^-$ with quark content dds and the c.c. resonances. The $\Sigma(1385)$ decays strongly and is not a decay product of any weakly decaying particle. Thus $\Sigma(1385)$ decays exclusively at the primary event vertex. The main decay channels are given in Tab. 5.1. The $\Sigma(1385)^0$ cannot be reconstructed well because the π^0 decays into two photons [34] which cannot be measured well in the ZEUS calorimeter. It is not measured in this analysis. From here on the label $\Sigma(1385)$ does not include the neutral states any longer but only the four charged particles. In the following, when the baryon $\Sigma(1385)^+$ is mentioned the anti-baryon $\overline{\Sigma}(1385)^-$ is also meant unless explicitly stated. The same is valid for the baryon-anti-baryon pair $\Sigma(1385)^-$ and $\overline{\Sigma}(1385)^+$.

	content	spin	Br	$\tau/10^{-10}$s	Γ/MeV
$\Xi^- \to \Lambda + \pi^-$	dss	1/2	$99.89 \pm 0.04\%$	1.64 ± 0.02	—
$\Sigma(1385)^- \to \Lambda + \pi^-$	dds	3/2	$88 \pm 2\%$	—	39.4 ± 2.1
$\Sigma(1385)^0 \to \Lambda + \pi^0$	uds				36 ± 5
$\Sigma(1385)^+ \to \Lambda + \pi^+$	uus				35.8 ± 0.8

Table 5.1: Main decay channels of Ξ^-, $\Sigma(1385)^-$, $\Sigma(1385)^0$ and $\Sigma(1385)^+$ and the corresponding quark content, spin, branching ratio, Br, lifetime, τ, and natural width, Γ [34].

Comparing the properties of both Ξ^- and $\Sigma(1385)$ (Tab. 5.1), differences are obvious which suggests that each particle needs its own best reconstruction approach. Since $\Sigma(1385)$ decays exclusively at the primary vertex, the particle will be reconstructed with primary vertex fitted tracks only, while the reconstruction of Ξ^- will use all tracks found in the CTD to reconstruct displaced tertiary vertices.

The reconstruction of both Ξ^- and $\Sigma(1385)$ are performed using charged tracks which can be detected and reconstructed in the CTD. The selected decay channel is the decay into a Λ and π, while the Λ is reconstructed via its decay into a proton and a pion. Since the reconstruction of Ξ^- and $\Sigma(1385)$ is based on the reconstruction of Λ baryons, it is important that the production of Λ baryons is modelled correctly in the Monte Carlo. A comparison of data and Monte Carlo prediction of Λ baryon production has been done previously [35] and it was found that the Monte Carlo describes the shapes of several investigated observables reasonably. However, data and Monte Carlo concerning the Λ baryon production are compared in this analysis, too.

The charge of all final decay products found in the CTD can be used to group the decays of Ξ^- and $\Sigma(1385)$ as seen in Tab. 5.2. This feature is used for the different reconstruction approaches, too.

		decay chain	$Q(p) * Q(\pi_1)$
Ξ^- $\overline{\Xi}^+$	$\Sigma(1385)^-$ $\overline{\Sigma}(1385)^+$	$\rightarrow \Lambda\pi_1^- \rightarrow p\pi_2^-\pi_1^-$ $\rightarrow \overline{\Lambda}\pi_1^+ \rightarrow \overline{p}\pi_2^+\pi_1^+$	-1
—	$\Sigma(1385)^+$ $\overline{\Sigma}(1385)^-$	$\rightarrow \Lambda\pi_1^+ \rightarrow p\pi_2^-\pi_1^+$ $\rightarrow \overline{\Lambda}\pi_1^- \rightarrow \overline{p}\pi_2^+\pi_1^-$	$+1$

Table 5.2: Decay chains of Ξ^- and $\Sigma(1385)$ baryons separated into two groups depending on the charge product $Q(p) * Q(\pi_1)$ of the proton, p, from the Λ decay and the first appearing pion in the decay chain (directly from the Ξ^- or $\Sigma(1385)$ decay), π_1.

The identification of Λ candidates is common for the reconstruction of Ξ^- and $\Sigma(1385)$ baryons. This is described before the detailed reconstruction of Ξ^- and $\Sigma(1385)$ is discussed.

5.1 Λ candidate identification

A Λ candidate is identified by its decay into a proton and pion where both charged particles leave a track in the CTD which can be reconstructed. Since Λ is a weakly decaying neutral particle (lifetime $\tau = 2.632 \cdot 10^{-10}$ s [34]) the decay vertex can be reconstructed as a secondary vertex separated from the primary vertex. The decay of a Λ baryon which is used for its reconstruction in the ZEUS detector is the decay into a proton and pion, $\Lambda \rightarrow p\pi$, and has a branching ratio, Br_Λ, of $Br_\Lambda = 63.9 \pm 0.5\%$ [34]. The reconstruction of secondary vertices is done with VCTRACK [22, 23] as described in chapter 3.

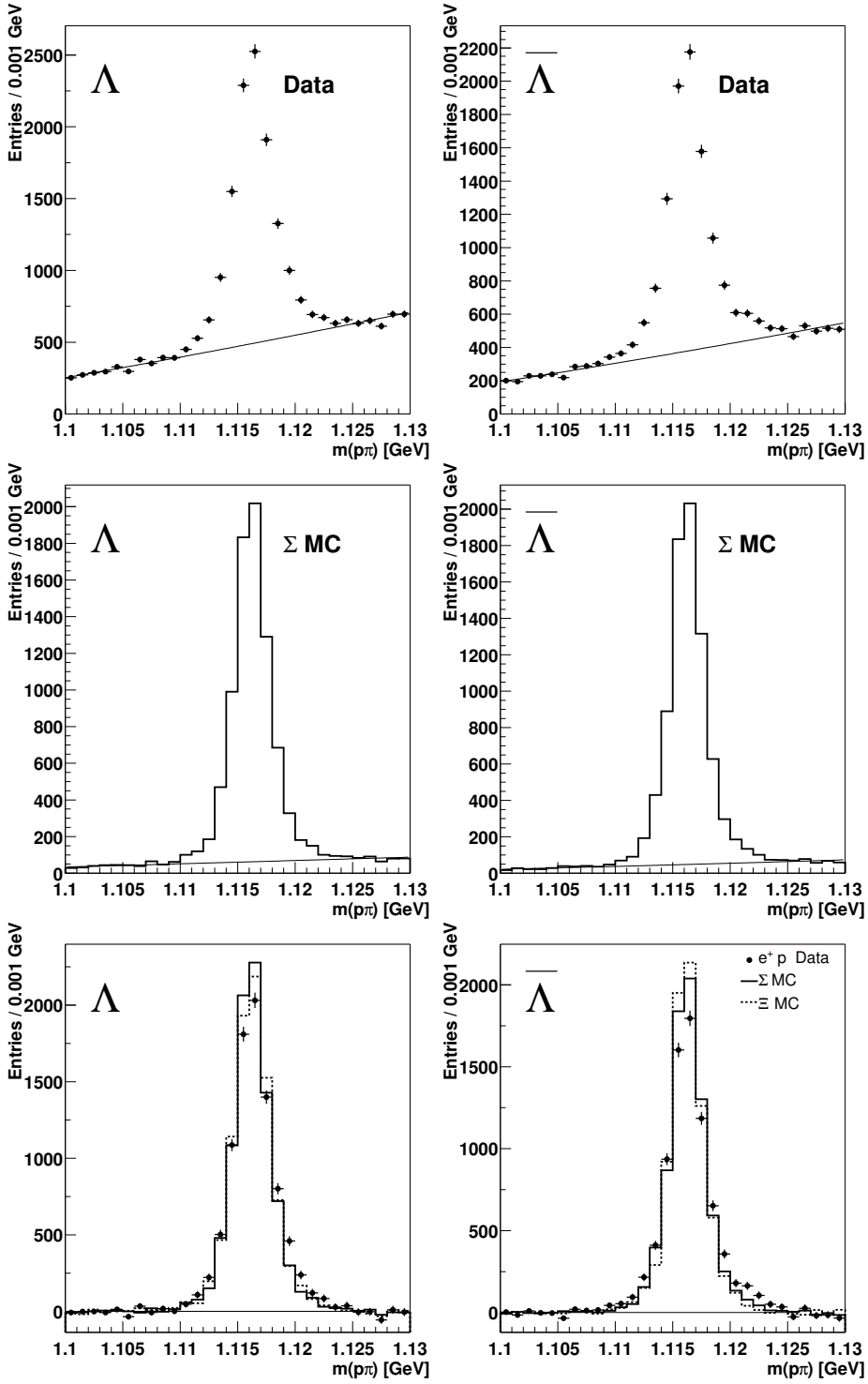

Figure 5.1: The mass distribution $m(p\pi)$ of all reconstructed Λ ($\overline{\Lambda}$) event candidates is shown in the left (right) column for data (top row) and CDM Σ–MC (middle row). These plots show a full line which is a fit with equation 5.1. Using this fit to subtract the background in the Λ event candidate samples, reasonable agreement between data (points), Ξ–MC (dashed histogram) and Σ–MC (full histogram) can be seen in the background subtracted Λ and $\overline{\Lambda}$ signal (bottom row). The MC distributions are scaled to the area below the data.

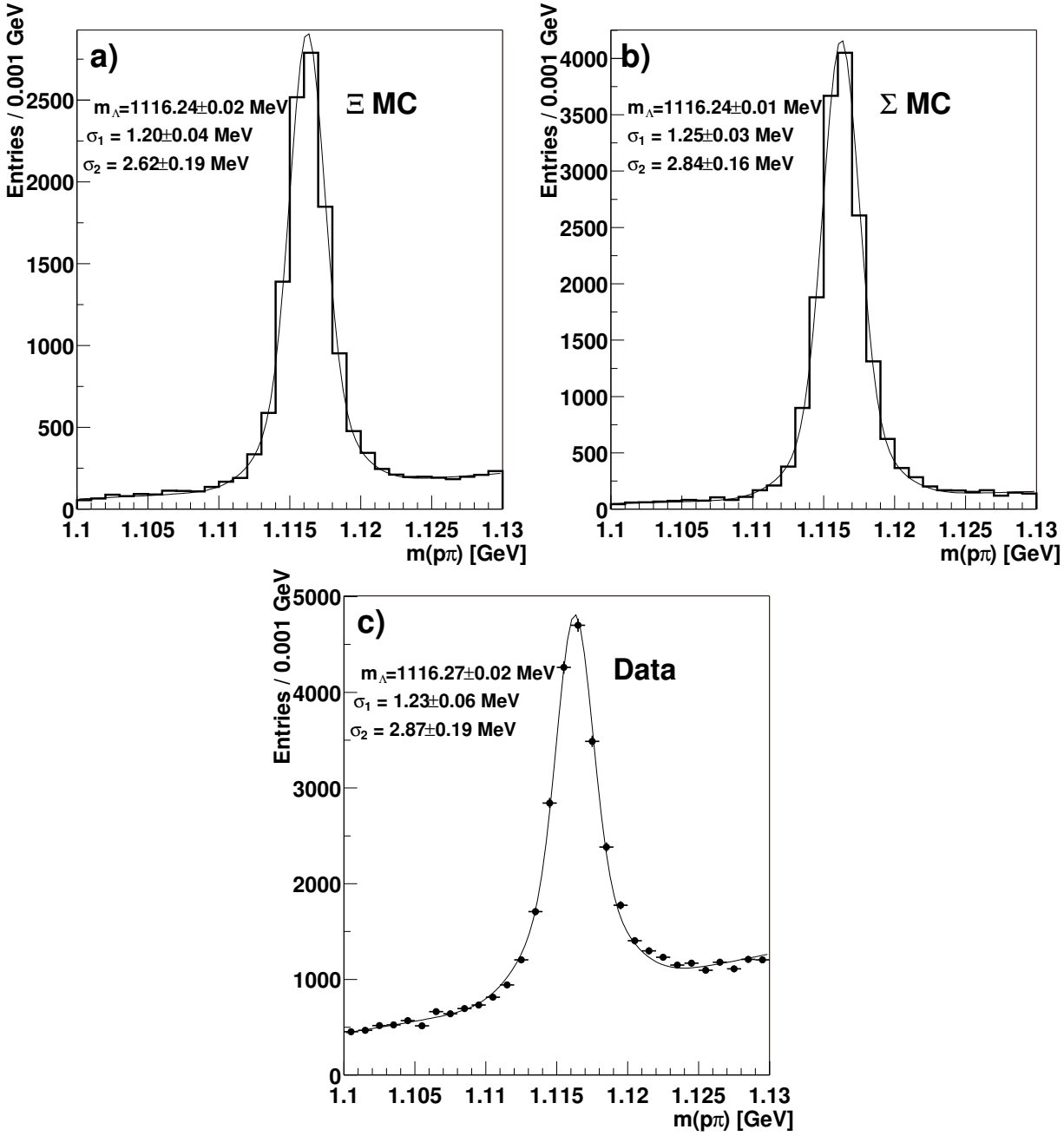

Figure 5.2: The mass distribution $m(p\pi)$ of all reconstructed Λ event candidates for (a) Ξ–MC, (b) Σ–MC and (c) experimental data. These plots show a full line which is a fit with equation 5.2.

All reconstructed secondary vertices of an event are taken into account to build a Λ event candidate sample. The invariant mass of each reconstructed candidate, $m(p\pi)$, is calculated by assigning the proton mass ($m_p = 938.2720$ MeV [34]) to the particle with the higher momentum and the pion mass ($m_\pi = 139.5702$ MeV [34]) to the other one. A Λ event candidate is found if the following requirements are fulfilled:

- both charged tracks have at least
  - hits in superlayers 1 to 3, to take advantage of the considerable resolution enhancement provided through the algorithms of the full stereo reconstruction,
  - $p_T > 0.15$ GeV and
  - $|\eta| < 1.75$, to stay away from the edge of acceptance which exists due to the implicit cut on transverse momentum and pseudorapidity set by the above requirement of three superlayers,
- pseudorapidity of Λ event candidate $|\eta| < 1.75$ and
- invariant mass: $1.1 < m(p\pi) < 1.13$ GeV.

The Λ candidates are defined as all Λ event candidates with an invariant mass of $1.112 < m(p\pi) < 1.119$ GeV. In this range the ratio of the Λ signal to background is about one or higher. In total 20585 Λ candidates are reconstructed.

The background of the Λ event candidate mass distribution is parameterised by

$$Bg\left(m(p\pi)\right) = A \cdot \left[m\left(p\pi\right) - \left(m_p + m_\pi\right)\right]^B \tag{5.1}$$

where A and B are parameters of the fit. For the fit the range around the signal of $1.109 < m(p\pi) < 1.124$ GeV is excluded from the fit. The data are compared to the ARIADNE (CDM) Ξ–MC and CDM Σ–MC, which have at least one generated Ξ^- and $\Sigma(1385)$ in the central region of the detector, respectively (see chapter 4.3). The Λ event candidate mass distributions of data and MC with this fit, as well as the background subtracted histograms, are shown in Fig. 5.1. The Λ event candidate mass distribution of both MC and data differ in the shape of the background. On the one hand, this results from the pre-selected signal Ξ–MC and Σ–MC. On the other hand, this feature appears in MC samples without any pre-selection, too. However the background subtracted Λ and $\overline{\Lambda}$ signal in the data is reasonably described by the MC (Fig. 5.1).

The comparison of the mass and width of the reconstructed Λ signal in data and MC is shown in Fig. 5.2. The mass distribution of the Λ event candidates is parameterised by

$$f\left(m\left(p\pi\right)\right) = G_{N_1,\sigma_1,m_\Lambda}\left(m\left(p\pi\right)\right) + G_{N_2,\sigma_2,m_\Lambda}\left(m\left(p\pi\right)\right) + Bg\left(m\left(p\pi\right)\right) \tag{5.2}$$

where G is a Gaussian and the fit parameters N_1 and σ_1 (N_2 and σ_2) are the number of Λ baryons and the width of the first (second) Gaussian, respectively. The mass of the Λ

signal, m_Λ, is the same fit parameter for both Gaussians. The comparison of the mass and width of the Λ signal in experimental data and MC is important for the subsequent reconstruction because it shows (Fig. 5.2) that the MC provides a reliable simulation of the mass and width of the reconstructed Λ mass. This indicates that the mass and width of other particles may be simulated properly, too.

5.2 Identification of Ξ^- baryons with reconstructed displaced tertiary vertices

The Ξ^- does not only decay close to the primary vertex but also separated from it, because it is a weakly decaying particle. Thus, the vertex of the decay $\Xi^- \to \Lambda\pi$ can be reconstructed separated from the primary vertex — similar to the secondary vertex reconstruction of $\Lambda \to p\pi^-$ decays — and is called a displaced tertiary vertex (Fig. 5.3).

For the reconstruction of displaced tertiary vertices (*dtv*) it is necessary to combine all Λ candidates with all charged CTD tracks of one event. The requirements for each CTD track are:

- hits in superlayers 1 to 3,
- $p_T > 0.15$ GeV and
- $|\eta| < 1.75$.

A *dtv* is reconstructed by finding the distance of closest approach (*dca*) between a Λ candidate and a charged CTD track (Fig. 5.3). Then the middle of a line connecting the points of *dca* on the Λ and CTD track defines the displaced tertiary decay vertex. For a real Ξ^- decay both Λ and π come from the same Ξ^- decay vertex. Thus, the reconstructed *dca* must not be large. Also the Λ, as the heavier particle, takes the biggest fraction of the Ξ^- momentum and therefore flies in nearly the same direction as the Ξ^-. These properties can be used to suppress reconstructed combinations which do not result from a Ξ^- decay. The following cuts are applied to each reconstructed displaced tertiary vertex:

- $dca < 2.5$ cm and $|dca_Z| < 1.5$ cm,
  where dca_Z is the Z component which contributes to *dca* and is defined as the difference between the Z position of the Λ candidate, Z_Λ, and of the pion candidate, Z_π: $dca_Z = Z_\Lambda - Z_\pi$. Since the resolution in Z is worse than in XY, in general the main contribution to *dca* originates from it. The cuts are motivated by the CDM Ξ–MC and an inclusive DIS CDM MC (Fig. 5.4(a)–(b)).

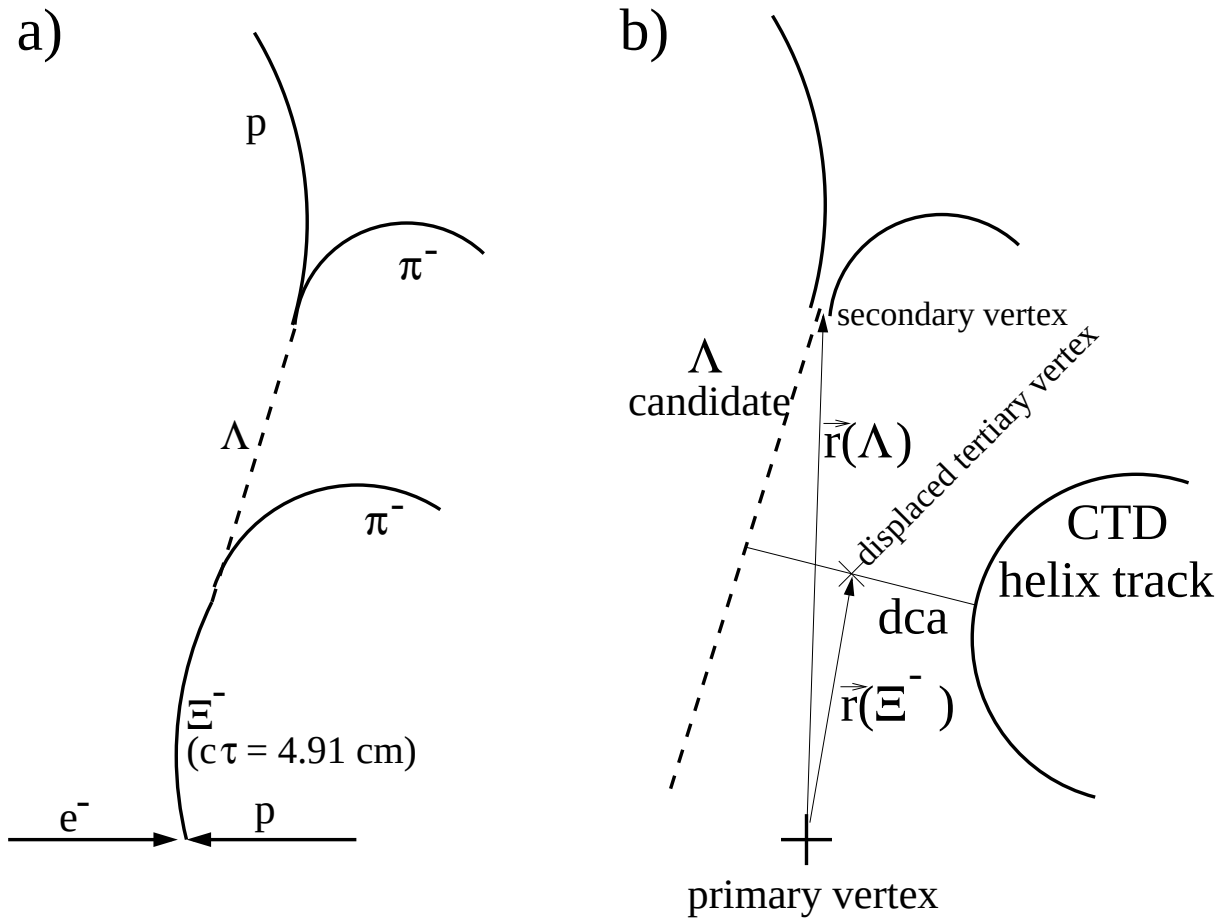

Figure 5.3: Two dimensional sketch of the reconstruction of displaced tertiary vertices. The investigated decay chain $\Xi^- \to \Lambda\pi^- \to p\pi^-\pi^-$ is shown in two ways. Part (a) presents the decays as they happen in real; clear decay vertices exist. The right part (b) shows the situation as found in the CTD. The decay of the Λ candidate is reconstructed by VCTRACK [22, 23] which finds secondary vertices. The distance of closest approach (*dca*) between the Λ candidate and every CTD helix track is calculated and the displaced tertiary vertex is defined as the middle of a line connecting the points of *dca* on the Λ and CTD track. The vector $\vec{r}(\Xi^-)$ points to the reconstructed displaced tertiary decay vertex of the reconstructed Ξ^- with its origin at the primary vertex. The vector $\vec{r}(\Lambda)$ points to the decay vertex of the Λ candidate.

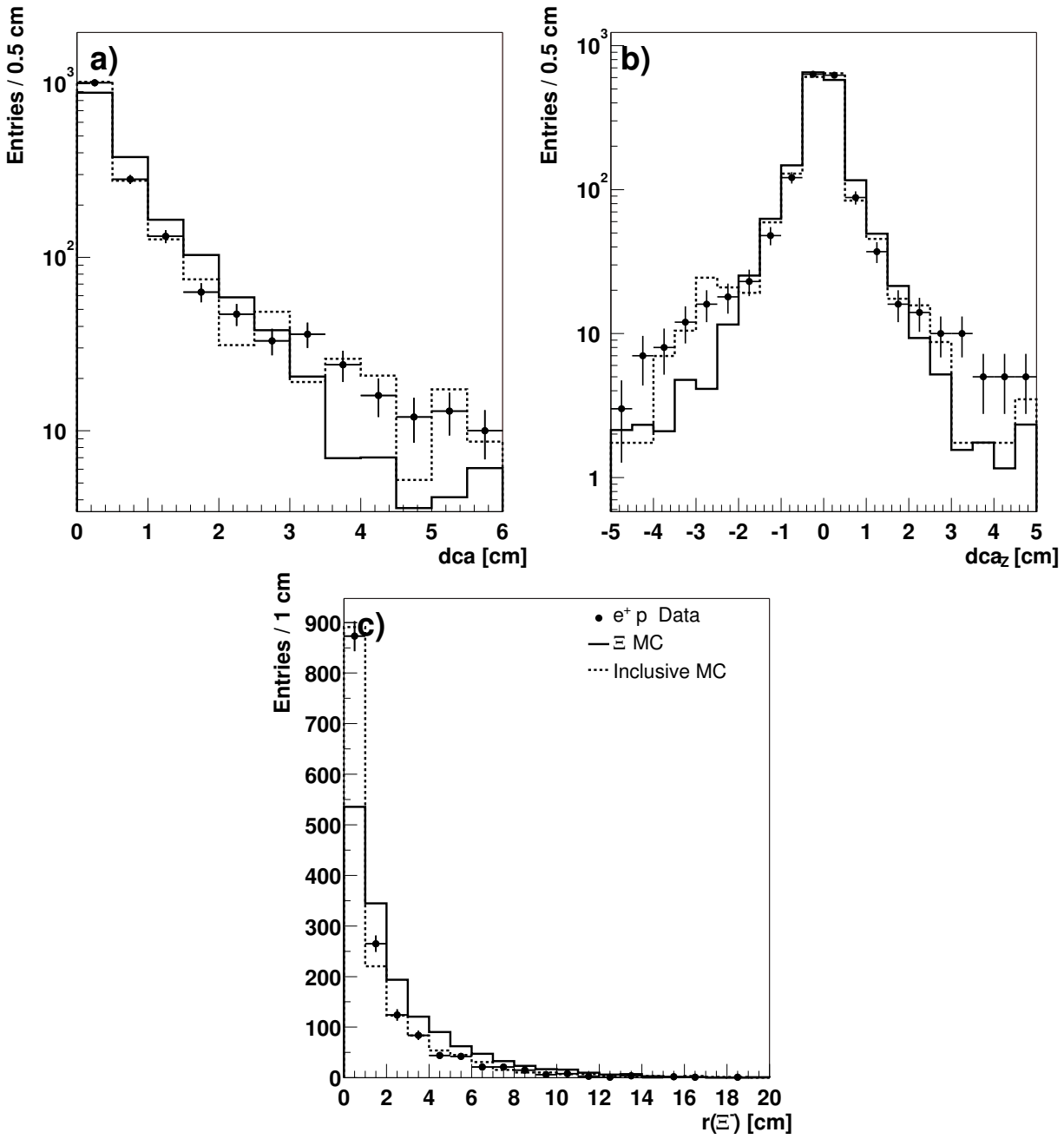

Figure 5.4: Distributions of (a) dca, (b) dca_Z and (c) $r(\Xi^-)$ for data (points), CDM Ξ–MC (full histogram) and an inclusive DIS CDM MC (dashed histogram) in the mass range of $1.3 < m(\Lambda\pi) < 1.34$ GeV, which covers the Ξ^- signal (Fig. 5.5). The applied cuts are $\vec{r}(\Xi^-) \cdot \vec{r}(\Lambda) > 0$ and $r(\Lambda) > r(\Xi^-)$ for (a)–(b), while all cuts listed in the text, except $r(\Xi^-) > 1.75$ cm, are applied for (c). The MC distributions are scaled to the area below the data distributions. They motivate the selection of the region $|dca| < 2.5$ cm, $|dca_Z| < 1.5$ cm and $r(\Xi^-) > 1.75$ cm, where most of the combinatorial background is rejected.

- $\cos(\vec{r}(\Lambda), \vec{r}(\Xi^-)) = \vec{r}(\Lambda) \cdot \vec{r}(\Xi^-)/(r(\Lambda) * r(\Xi^-)) > 0$ and $r(\Lambda) > r(\Xi^-)$, where $r = |\vec{r}|$ and $\vec{r}(\Lambda)$ ($\vec{r}(\Xi^-)$) is the vector to the decay vertex of the Λ candidate (Ξ^- candidate) with its origin at the reconstructed primary vertex. Both cuts use the property that the Λ flies nearly in the same direction as the Ξ^-.

The point of *dca* on the CTD track helix defines its momentum at the decay vertex. The invariant mass of the Ξ^- candidate, $m(\Lambda\pi)$, is calculated by assigning the Λ mass ($m_\Lambda = 1.115683$ GeV [34]) to the Λ candidate and the pion mass ($m_\pi = 139.5702$ MeV [34]) to the CTD track at the decay vertex. A reconstructed particle is called Ξ^- candidate if it passes the following criteria:

- $1.0 < p_T(\Xi^-) < 5.0$ GeV,
- $|\eta(\Xi^-)| < 1.5$,
- $m(\Lambda\pi) < 1.505$ GeV and
- $r(\Xi^-) > 1.75$ cm, to make use of the lifetime of Ξ^- and suppress combinatorial background which comes from tracks with the origin at the primary vertex (Fig. 5.4(c)).

The correct combination $Q(p) \cdot Q(\pi) = -1$ (Tab. 5.2) of the charge of the proton, $Q(p)$, from the Λ decay and the charge of the pion, $Q(\pi)$, which comes from the decay of a Ξ^- candidate, is called the signal sample while the wrong charge combination is used as a background sample.

The invariant mass distribution of all Ξ^- candidates (Fig. 5.5) shows a signal at $m(\Lambda\pi) \approx 1.321$ GeV. The number of Ξ^- in the signal sample is obtained by fitting the mass distribution. The fit is performed with the Maximum-Likelihood method to the mass distribution which has 20 times more bins than the shown figure (Fig. 5.5). The parameterisation used is

$$f\left(m\left(\Lambda\pi\right)\right) = N_\Xi \cdot [r \cdot G_1(m(\Lambda\pi)) + (1-r) \cdot G_2(m(\Lambda\pi))] + A \cdot Bg_{B,C}(m(\Lambda\pi)) \qquad (5.3)$$

where G is a Gaussian with the area below it normalised to one. The mass, m_Ξ, which is used in both Gaussians, the width, $\sigma_{1,\Xi}$, of the first Gaussian, G_1, the width, $\sigma_{2,\Xi}$, of the second Gaussian, G_2, and the parameter r are fixed to values obtained from the same fit to the Ξ–MC, where all parameters are kept as fit parameters. The fit parameters are N_Ξ, that gives the number of reconstructed Ξ^- baryons, and A, which is calculated in such a way that it gives the number of background events below the Ξ^- signal in the mass window $1.305 < m(\Lambda\pi) < 1.345$ GeV. The parameterisation of the background, Bg, is defined as

$$Bg_{B,C}(m(\Lambda\pi)) = \left[(m_{diff})^B + C * m_{diff}\right],$$

where $m_{diff} = m(\Lambda\pi) - m_\Lambda - m_\pi$ is the mass difference between the reconstructed mass, $m(\Lambda\pi)$, and the kinematic threshold, $m_\Lambda + m_\pi$, and B and C are free parameters of the fit.

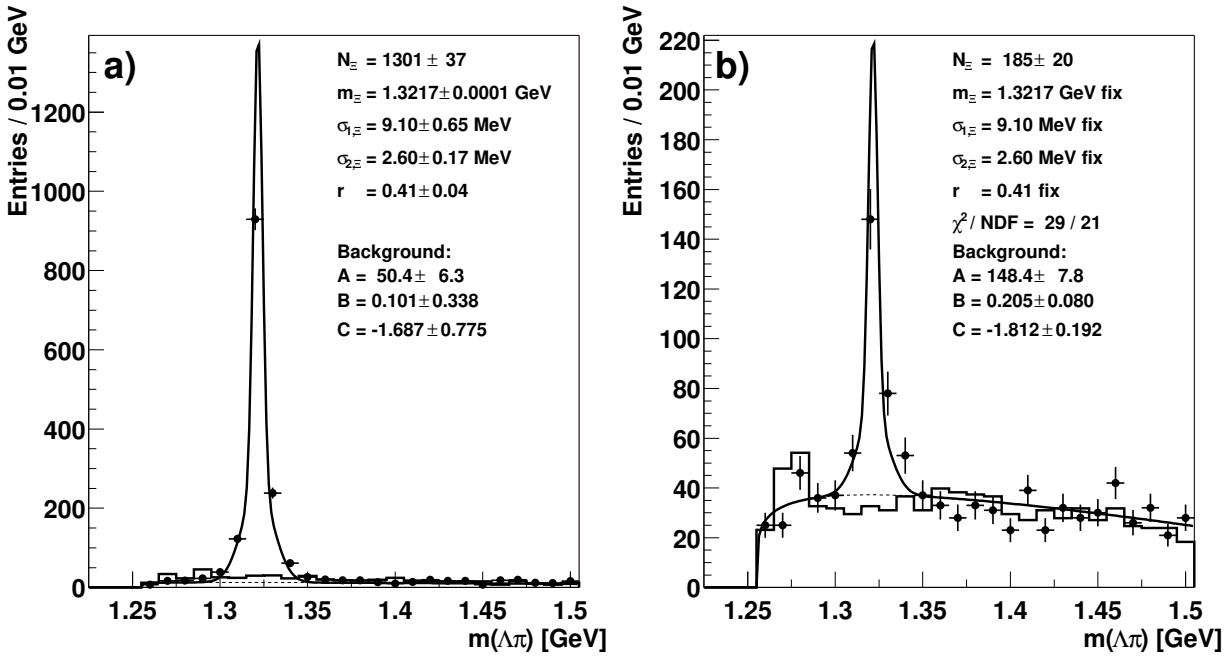

Figure 5.5: Mass distributions, $m(\Lambda\pi)$, of Ξ^- candidates reconstructed with displaced tertiary vertices in the (a) CDM Ξ–MC and (b) data. The points correspond to the signal sample while the histogram shows the wrong charge background which is normalised to the area of the signal sample in the mass range of $1.355 < m(\Lambda\pi) < 1.505$ GeV. The full line shows the parameterisation which is found by the fit to the signal sample, the dashed line represents the parameterisation of the background with the fit parameters A, B and C as described in the text. The mass, m_Ξ, and widths, $\sigma_{1,\Xi}$ and $\sigma_{2,\Xi}$, of the Ξ^- signal are free for the fit to the mass distribution of the Ξ–MC and the found values are used to determine the number of Ξ^- in the data.

Since the number of events with a Ξ^- is not big enough to determine the widths, $\sigma_{1,\Xi}$ and $\sigma_{2,\Xi}$, and mass, m_Ξ, of the Ξ^- signal directly from the data, the ARIADNE (CDM) Ξ–MC is used to set m_Ξ, $\sigma_{1,\Xi}$ and $\sigma_{2,\Xi}$ (Fig. 5.5(a)). From the Σ–MC it can be calculated that the acceptance of $\Sigma(1385)$ baryons is less than 0.05%. Thus, no signal can be seen in the data and no Gaussian for a $\Sigma(1385)$ signal is included to the fit function described above (Eq. 5.3).

The total number of Ξ^- baryons in the data is obtained by the following procedure. First, Eq. 5.3 is fitted to the mass distribution $m(\Lambda\pi)$ as described above. Then, the number of events in a mass window of $1.305 < m(\Lambda\pi) < 1.345$ GeV, which covers the Ξ^- signal, is counted. The number of reconstructed Ξ^- baryons is defined as all events counted in the specified mass window subtracted by the number of background events in the same range

given by the fit parameter A. The total number of reconstructed Ξ^- baryons, measured with the described method, is 185 ± 20 (Fig. 5.5(b)).

The fit to the mass distributions $m(\Lambda\pi^-)$ and $m(\overline{\Lambda}\pi^+)$ are performed in the same way as described above, except that, in addition, the parameter, B, of the background parameterisation is fixed to the parameter B of the fit to the total mass distribution $m(\Lambda\pi)$. This fixing allows a stable fit even with half of the statistics. The number of all Ξ^- and $\overline{\Xi}^+$ decays is 92 ± 14 and 92 ± 14, respectively (Fig. 5.6).

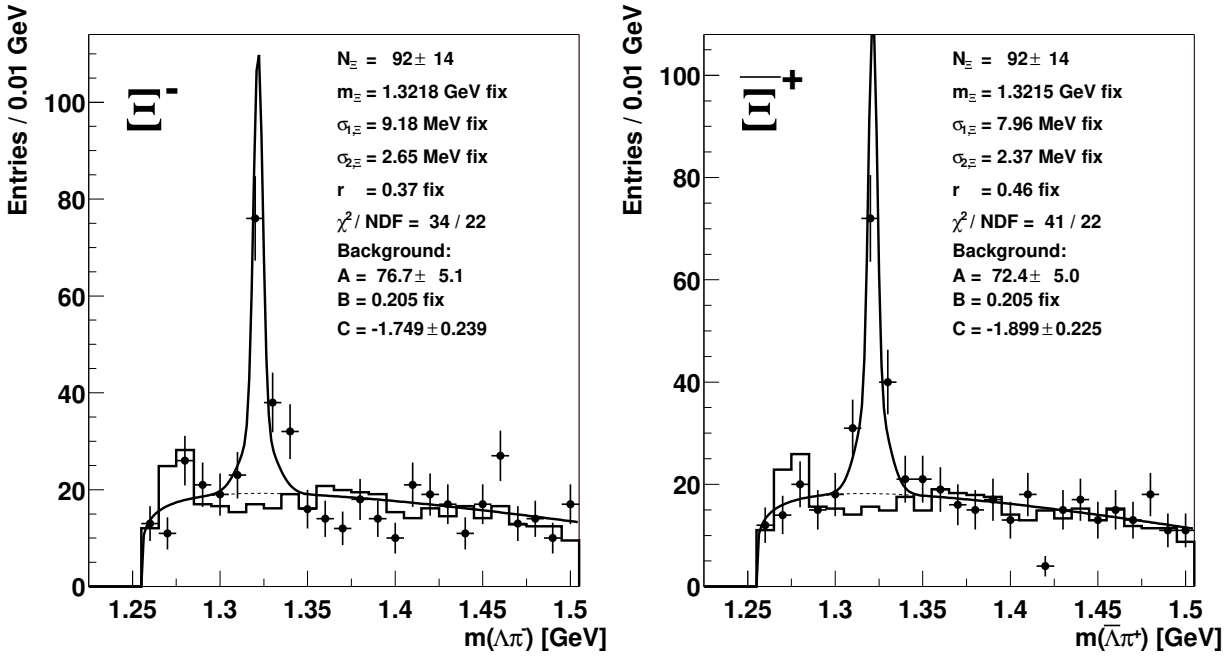

Figure 5.6: Mass distribution, $m(\Lambda\pi)$, of reconstructed (left) Ξ^- and (right) $\overline{\Xi}^+$ candidates. The points correspond to the signal sample while the histogram shows the wrong charge background which is normalised to the area of the signal sample in the range of $1.355 < m(\Lambda\pi) < 1.505$ GeV. The full line shows the parameterisation which is found by the fit to the signal sample and the dashed line represents the parameterisation of the background with the fit parameters A and C. The parameter B is fixed to the value from the fit to the combined mass distribution of Ξ^- and $\overline{\Xi}^+$ (Fig. 5.5(b)).

A number of consistency checks are performed. In the following the results are shown with mass and widths kept as fit parameters and using the wrong charge background sample to determine the parameters for the background parameterisation. Also, the widths of the Ξ^- signal are increased by the uncertainty of the fit to the CDM Ξ–MC. All these changes give a reasonable description and all obtained numbers of Ξ^- decays are consistent within the statistical errors:

- The first width, $\sigma_{1,\Xi}$, of the Ξ^- signal is increased by the uncertainty of the fit to the CDM Ξ–MC of 0.65 MeV to a width of 9.75 MeV. The number of Ξ^- baryons is

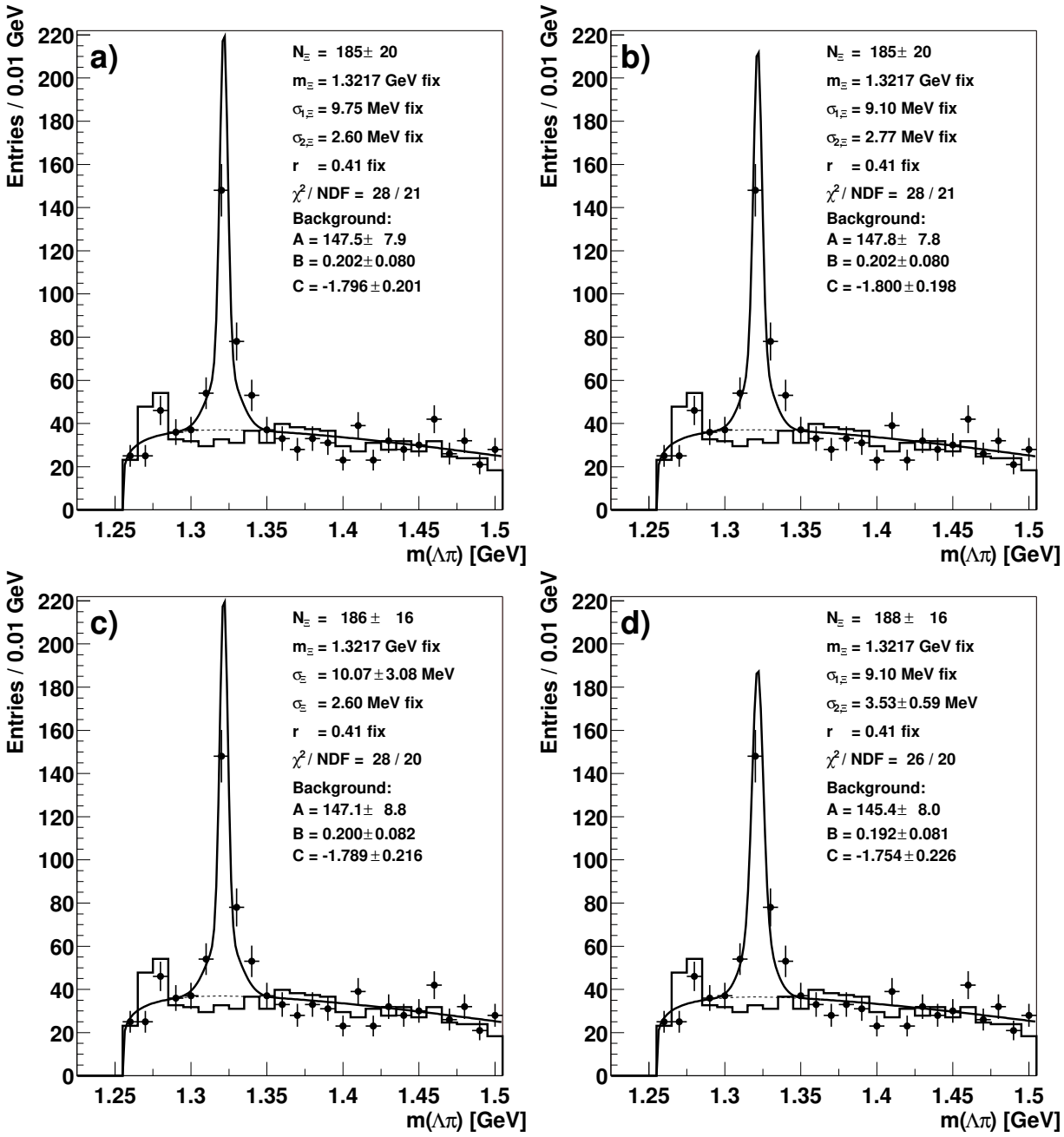

Figure 5.7: Mass distribution, $m(\Lambda\pi)$, of reconstructed Ξ^- candidates. The full line shows the parameterisation which is found by fitting the signal sample with (a) the first width, $\sigma_{1,\Xi}$, increased by the uncertainty of the CDM Ξ–MC, (b) the second width, $\sigma_{2,\Xi}$, increased by the uncertainty of the CDM Ξ–MC, (c) the first width, $\sigma_{1,\Xi}$, kept as a fit parameter and (d) the second width, $\sigma_{2,\Xi}$, kept as a fit parameter. The histogram shows the wrong charge background which is normalised to the area of the signal sample in the range of $1.355 < m(\Lambda\pi) < 1.505$ GeV. The dashed line represents the background parameterisation only.

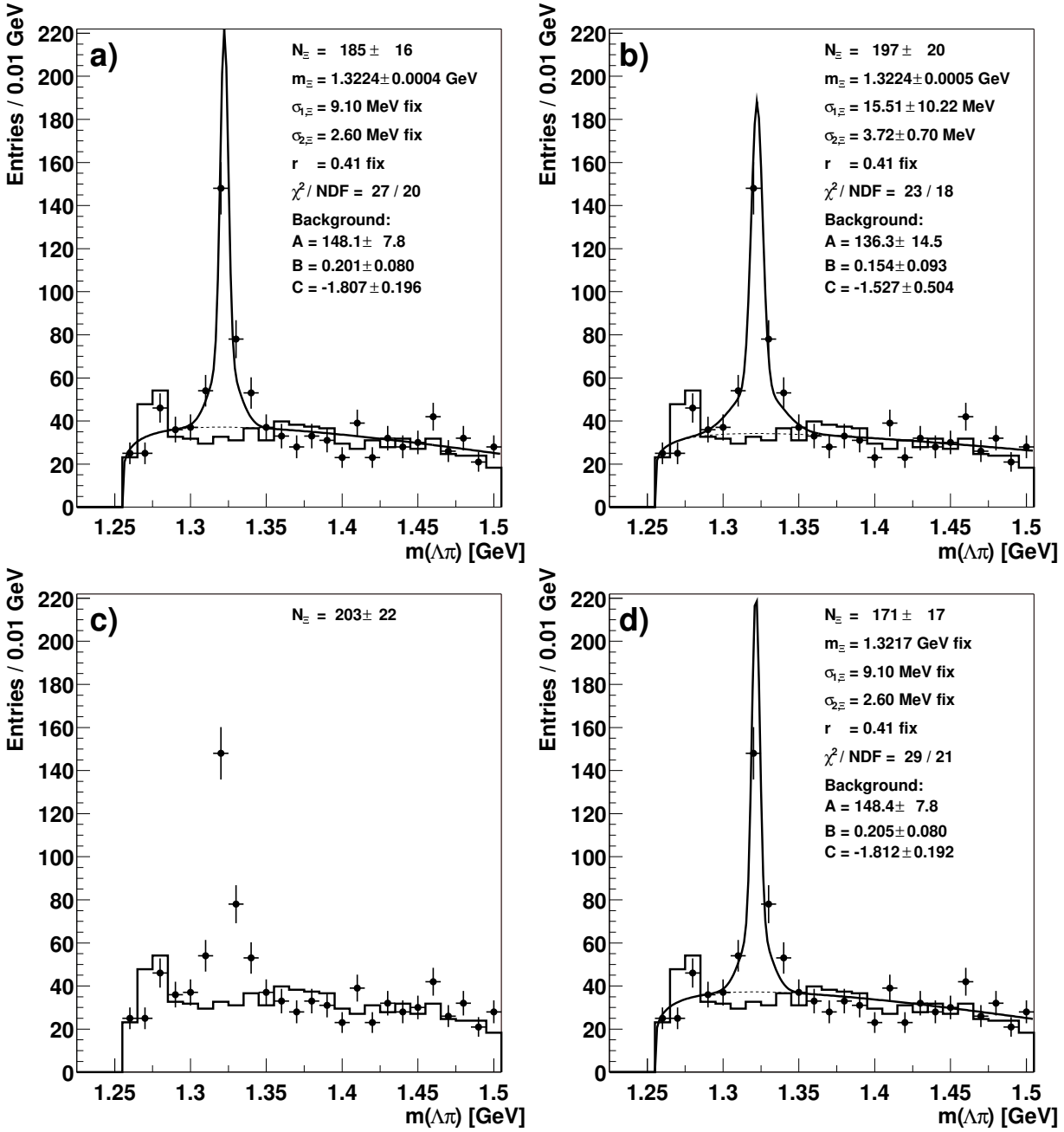

Figure 5.8: Mass distribution, $m(\Lambda\pi)$, of reconstructed Ξ^- candidates. The full line shows the parameterisation which is found by fitting the signal sample with (a) the mass, m_Ξ, kept as a fit parameter, (b) neither mass nor widths fixed for the fit. (c) The number of entries in the signal sample in the mass window of $1.305 < m(\Lambda\pi) < 1.345$ GeV is subtracted by the number of entries in the scaled wrong charge mass distribution in the same mass window. (d) The number of Ξ^- baryons is calculated from the fit parameter N_Ξ (Eq. 5.3). The histogram shows the wrong charge background which is normalised to the area of the signal sample in the range of $1.355 < m(\Lambda\pi) < 1.505$ GeV. The dashed line represents the background parameterisation only.

185 ± 20 (Fig. 5.7(a)) and in agreement with the default fit.

- The second width, $\sigma_{2,\Xi}$, of the Ξ^- signal is increased by the uncertainty of the fit to the CDM Ξ–MC of 0.17 MeV to a width of 2.77 MeV. The number of Ξ^- baryons is 185 ± 20 (Fig. 5.7(b)) and in agreement with the default fit.

- The first width, $\sigma_{1,\Xi}$, is kept as a fit parameter. The fit determines a width of $\sigma_{1,\Xi} = 10.07 \pm 3.08$ MeV while the yield of Ξ^- baryons is 186 ± 16 (Fig. 5.7(c)). The MC predicts a resolution of $\sigma_{1,\Xi} = 9.10 \pm 0.65$ GeV which is within the errors.

- The second width, $\sigma_{2,\Xi}$, is kept as a fit parameter. The fit determines a width of $\sigma_{2,\Xi} = 3.53 \pm 0.59$ MeV while the yield of Ξ^- baryons is 188 ± 16 (Fig. 5.7(d)). The MC predicts a resolution of $\sigma_{2,\Xi} = 2.60 \pm 0.17$ GeV.

- The mass of the Ξ^- signal is not fixed in the fit to the signal sample but kept as a free parameter. It is found to be $m_\Xi = 1.3224 \pm 0.0004$ GeV which is close to the global value of $m_\Xi = 1.3213 \pm 0.0001$ GeV [34] and the mass simulated from the MC of $m_\Xi = 1.3217 \pm 0.0001$ GeV. The number of reconstructed Ξ^- baryons is 185 ± 16 (Fig. 5.8(a)) and identical with the default fit.

- Releasing all three parameters (m_Ξ, $\sigma_{1,\Xi}$ and $\sigma_{2,\Xi}$) the fit prefers the values $m_\Xi = 1.3224 \pm 0.0005$ GeV, $\sigma_{1,,\Xi} = 15.51 \pm 10.22$ MeV and $\sigma_{2,\Xi} = 3.72 \pm 0.70$ MeV. The numbers of Ξ^- baryons is calculated to be 197 ± 20 (Fig. 5.8(b)).

- The number of entries in the signal sample in the mass window of $1.305 < m(\Lambda\pi) < 1.345$ GeV is subtracted by the number of entries in the scaled wrong charge mass distribution in the same mass window. The number of reconstructed Ξ^- baryons is 203 ± 22 (Fig. 5.8(c)). The wrong charge mass distribution is normalised to the area of the signal sample in the range of $1.355 < m(\Lambda\pi) < 1.505$ GeV.

- The number of Ξ^- baryons is calculated from the area below the two Gaussians from the fit which is given by the fit parameter N_Ξ (Eq. 5.3). The yield of Ξ^- baryons with this method is 171 ± 17 (Fig. 5.8(d)).

These checks show that a consistent number of reconstructed Ξ^- baryons is obtained for all changes and that the described fit procedure is stable and reasonable.

The reliability of the CDM Ξ–MC can be verified by comparing distributions of data and Ξ–MC for observables which are important for the reconstruction of displaced tertiary vertices. The Ξ–MC has at least one Ξ^- in every event, which is of course not given for the data sample. Thus a perfect agreement is not expected since both samples differ. However, both samples are as equal as possible if only events are chosen which have a reconstructed mass below the Ξ^- signal. The chosen range of the reconstructed mass is $1.3 < m(\Lambda\pi) < 1.34$ GeV. The comparison of the transverse momentum and pseudorapidity of the track which is combined with the Λ candidate shows a reasonable agreement

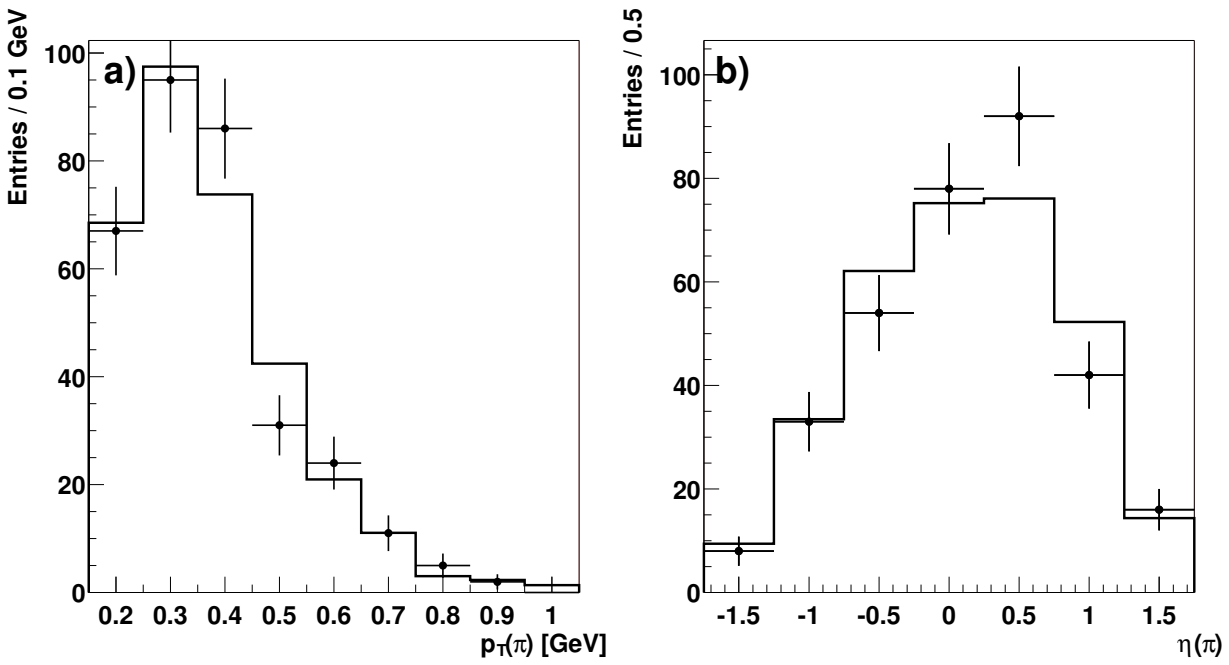

Figure 5.9: The distributions of (a) the transverse momentum, $p_T(\pi)$, and (b) pseudorapidity, $\eta(\pi)$, of the pion from the Ξ^- decay in the laboratory system below the Ξ^- mass signal ($1.3 < m(\Lambda\pi) < 1.34$ GeV) are presented for data (points) and CDM Ξ–MC (histogram).

(Fig. 5.9(a)–(b)) between data and Ξ–MC. Also the distributions of dca, dca_Z, $r(\Lambda)-r(\Xi^-)$, $\cos(\vec{r}(\Lambda), \vec{r}(\Xi^-)) = \vec{r}(\Lambda) \cdot \vec{r}(\Xi^-)/(r(\Lambda) * r(\Xi^-))$ and $r(\Xi^-)$ (Fig. 5.10(a)–(e)) are predicted by the Ξ–MC in good agreement with the data.

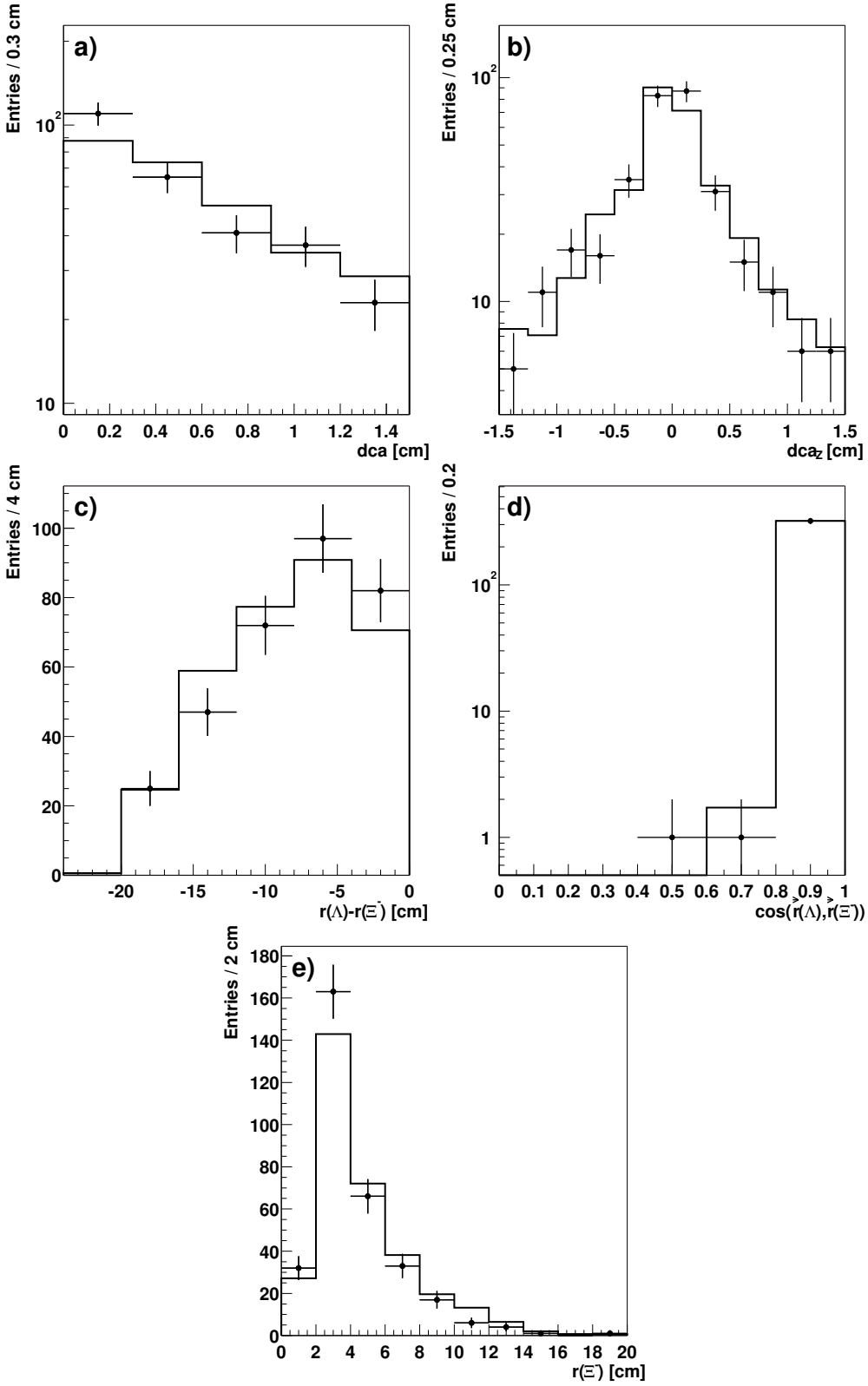

Figure 5.10: The distributions of (a) dca, (b) dca_Z, (c) $r(\Lambda) - r(\Xi^-)$, (d) $\cos((\vec{r}(\Lambda), \vec{r}(\Xi^-))$ and (e) $r(\Xi^-)$ below the Ξ^- mass signal ($1.3 < m(\Lambda\pi) < 1.34$ GeV) are presented for data (points) and CDM Ξ–MC (histogram). All cuts listed in the text are applied, which are $dca < 2.5$ cm, $|dca_Z| < 1.5$ cm, $\cos(\vec{r}(\Lambda), \vec{r}(\Xi^-)) > 0$, $1.0 < p_T(\Xi^-) < 5.0$ GeV, $|\eta(\Xi^-)| < 1.5$, $m(\Lambda\pi) < 1.5$ GeV and $r(\Xi^-) > 1.75$ cm.

Search for Ω^- baryons with reconstructed displaced tertiary vertices

The Ω^- baryon is a weakly decaying particle as it is the case for the Ξ^- baryon. The lifetime of the Ω^- is $\tau = (0.822 \pm 0.012) \cdot 10^{-10}$ s [34], which corresponds to a $c\tau$ of $c\tau = 2.46$ cm that is less than for the Ξ^- baryon with $c\tau = 4.91$ cm [34]. The main decay channel of the Ω^- baryon is $\Omega^- \rightarrow \Lambda K^-$ with a branching ratio of $BR_{\Omega^-} = 67.8 \pm 0.7\%$ [34]. The quark content of a Ω^- consists of three strange quarks. Thus, the production of Ω^- is even more suppressed than for Ξ^- baryons. However, the invariant mass of each Ω^- candidate, $m(\Lambda K^-)$, can be calculated by assigning the Λ mass ($m_\Lambda = 1.115683$ GeV [34]) to the Λ candidate and the kaon mass ($m_{K^-} = 493.677$ MeV [34]) to the CTD track at the decay vertex. The events which are selected fulfill the same requirements for displaced tertiary vertices as introduced for the Ξ^- baryon identification. No signal of Ω^- baryons can be seen (Fig. 5.11).

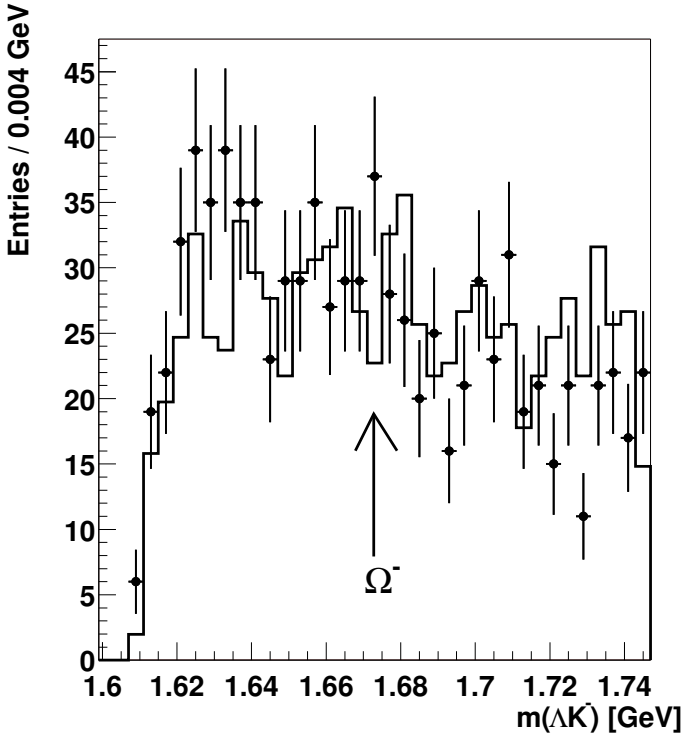

Figure 5.11: Mass distribution, $m(\Lambda K^-)$, of Ω^- baryon candidates (points) reconstructed with displaced tertiary vertices. The histogram shows the wrong charge background which is normalised to the area below the signal sample. The mass of the Ω^- is marked with an arrow.

5.3 Identification of Ξ^- and $\Sigma(1385)$ baryons with primary vertex fitted tracks

The $\Sigma(1385)$ decays exclusively at the primary vertex. Therefore $\Sigma(1385)$ candidates should be reconstructed by combining each Λ candidate with all primary vertex fitted tracks. The invariant mass of each $\Sigma(1385)$ candidate, $m(\Lambda\pi)$, is calculated by assigning the Λ mass ($m_\Lambda = 1.115683$ GeV [34]) to the Λ candidate and the pion mass ($m_\pi = 139.5702$ MeV [34]) to the primary vertex fitted track. The requirements for the primary vertex fitted track are:

- hits in superlayers 1 to 3,
- $p_T > 0.15$ GeV and
- $|\eta| < 1.75$.

A reconstructed particle is considered to be a $\Sigma(1385)$ candidate if it passes the following criteria:

- $1.0 < p_T < 5.0$ GeV,
- $|\eta| < 1.5$ and
- $m(\Lambda\pi) < 1.505$ GeV.

The invariant mass distribution (Fig. 5.12(c)) shows a Ξ^- signal at $m(\Lambda\pi) \approx 1.321$ GeV and a $\Sigma(1385)$ signal at $m(\Lambda\pi) \approx 1.385$ GeV. The distribution is parameterised to obtain the number of reconstructed Ξ^- and $\Sigma(1385)$ baryons. The fit is performed with the Maximum-Likelihood method to the mass distribution which has 10 times more bins than the figure shown (Fig. 5.12). The chosen parameterisation, $f(m(\Lambda\pi))$, has the form

$$\begin{aligned} f(m(\Lambda\pi)) \;=\; & N_\Xi \cdot [r \cdot G_1(m(\Lambda\pi) + (1-r) \cdot G_2(m(\Lambda\pi))] + \\ & N_\Sigma \cdot BW(m(\Lambda\pi)) + \\ & A \cdot Bg_{B,C}(m(\Lambda\pi)) \end{aligned} \tag{5.4}$$

where G is a Gaussian normalised to one and

$$BW(m(\Lambda\pi)) = \text{const.} \cdot \Gamma \frac{m_\Sigma}{\sigma_\Sigma} \int_{m_\Sigma - 5\Gamma}^{m_\Sigma + 5\Gamma} e^{-\frac{(m_1 - m(\Lambda\pi))^2}{2\sigma_\Sigma^2}} \cdot \frac{m_1}{\left(m_1^2 - m_\Sigma^2\right)^2 + m_\Sigma^2 \Gamma^2} dm_1$$

is a relativistic Breit-Wigner function convoluted with a Gaussian normalised to one. The mass, m_Ξ, which is used in both Gaussians, the width, $\sigma_{1,\Xi}$, of the first Gaussian, G_1, the width, $\sigma_{2,\Xi}$, of the second Gaussian, G_2, and the parameter r are fixed to values

obtained from the fit to the Ξ–MC (Fig. 5.12(a)), where these parameters are kept as fit parameters. The mass, m_Σ, and width of the Breit-Wigner function, Γ, are fixed to $m_\Sigma = 1.385$ GeV and $\Gamma = 37.6$ MeV, respectively[1]. The fit parameters are N_Ξ and N_Σ, which give the number of reconstructed Ξ^- and $\Sigma(1385)$, respectively, the width, σ_Σ, of the Gaussian which is convoluted with the Breit-Wigner function and A. The parameter A is the normalisation of the background function, $Bg_{B,C}$, and is calculated in such a way that A gives the number of background events below the $\Sigma(1385)$ signal in the mass window $1.34 < m(\Lambda\pi) < 1.43$ GeV. The background parameterisation, $Bg_{B,C}(m(\Lambda\pi))$, is defined as

$$Bg_{B,C}(m(\Lambda\pi)) = (m_{diff})^B + C * m_{diff}$$

where $m_{diff} = m(\Lambda\pi) - m_\Lambda - m_\pi$ is the mass difference between the reconstructed mass, $m(\Lambda\pi)$, and the kinematic threshold, $m_\Lambda + m_\pi$, and B and C are fit parameters.

To complicate matters, the MC version used does not support a Breit-Wigner function to simulate the decay of $\Sigma(1385)$, but instead uses a Gaussian. Thus, a Gaussian instead of the Breit-Wigner function in the parameterisation is used to determine the number of reconstructed $\Sigma(1385)$ in the MC.

The total number of $\Sigma(1385)$ in the experimental data is determined by the fit (Fig. 5.12(c)) to be 541 ± 96.

The invariant mass distribution of $\Sigma(1385)^-$ and charge conjugated (c.c.) candidates should have a Ξ^- signal but the distribution of $\Sigma(1385)^+$ and c.c. candidates should not (see Tab. 5.2). This is shown to be the case (Fig. 5.13(a) and 5.13(b)). The total number of Ξ^- given by the fit is 191 ± 30 (Fig. 5.13(b)). The reconstructed number of $\Sigma(1385)^+$ and $\Sigma(1385)^-$ is 303 ± 60 and 232 ± 71 (Fig. 5.13(a) and 5.13(b)), respectively. For the fit of the Breit-Wigner function to the $\Sigma(1385)^+$ and $\Sigma(1385)^-$ candidates, the global mass of $m_{\Sigma(1385)^+} = 1.3828$ GeV and $m_{\Sigma(1385)^-} = 1.3872$ GeV [34] (width of $\Gamma_{\Sigma(1385)^+} = 35.8$ MeV and $\Gamma_{\Sigma(1385)^-} = 39.4$ MeV [34]) is used, respectively.

The number of Ξ^-, $\overline{\Xi}^+$, $\Sigma(1385)^-$, $\overline{\Sigma}(1385)^+$, $\Sigma(1385)^+$ and $\overline{\Sigma}(1385)^-$ decays obtained by the fit to the mass distributions (Fig. 5.14) are shown in Tab. 5.3. The width, σ_Σ, of the Gaussian convoluted with the Breit-Wigner function is fixed for the fit to the mass distributions of $\Sigma(1385)^-$ and $\overline{\Sigma}(1385)^+$ candidates. The fixed value for σ_Σ is taken from the fit to the $\Sigma(1385)^-$ distribution (Fig. 5.13(b)) which includes $\Sigma(1385)^-$ and $\overline{\Sigma}(1385)^+$. The fit to the mass distributions of $\Sigma(1385)^+$ and $\overline{\Sigma}(1385)^-$ is performed with a fixed value of σ_Σ taken from the fit to the $\Sigma(1385)^+$ distribution (Fig. 5.13(a)) which includes $\Sigma(1385)^+$ and $\overline{\Sigma}(1385)^-$.

The number of reconstructed $\Sigma(1385)$ baryons can be compared to the number of reconstructed $\overline{\Sigma}(1385)$ anti-baryons. The mass distribution of the $\Sigma(1385)$ baryon candidates

[1]Since the distributions in Fig. 5.12 contain both $\Sigma(1385)^+$ and $\Sigma(1385)^-$ the mass is fixed to the mean of both $m_{\Sigma(1385)^+} = 1.3828$ GeV and $m_{\Sigma(1385)^-} = 1.3872$ GeV, which is calculated to be $m = 1.385$ GeV. The width of the Breit-Wigner function, which is chosen, is the mean of $\Gamma_{\Sigma(1385)^+} = 35.8$ MeV and $\Gamma_{\Sigma(1385)^-} = 39.4$ MeV and computed to be $\Gamma = 37.6$ MeV.

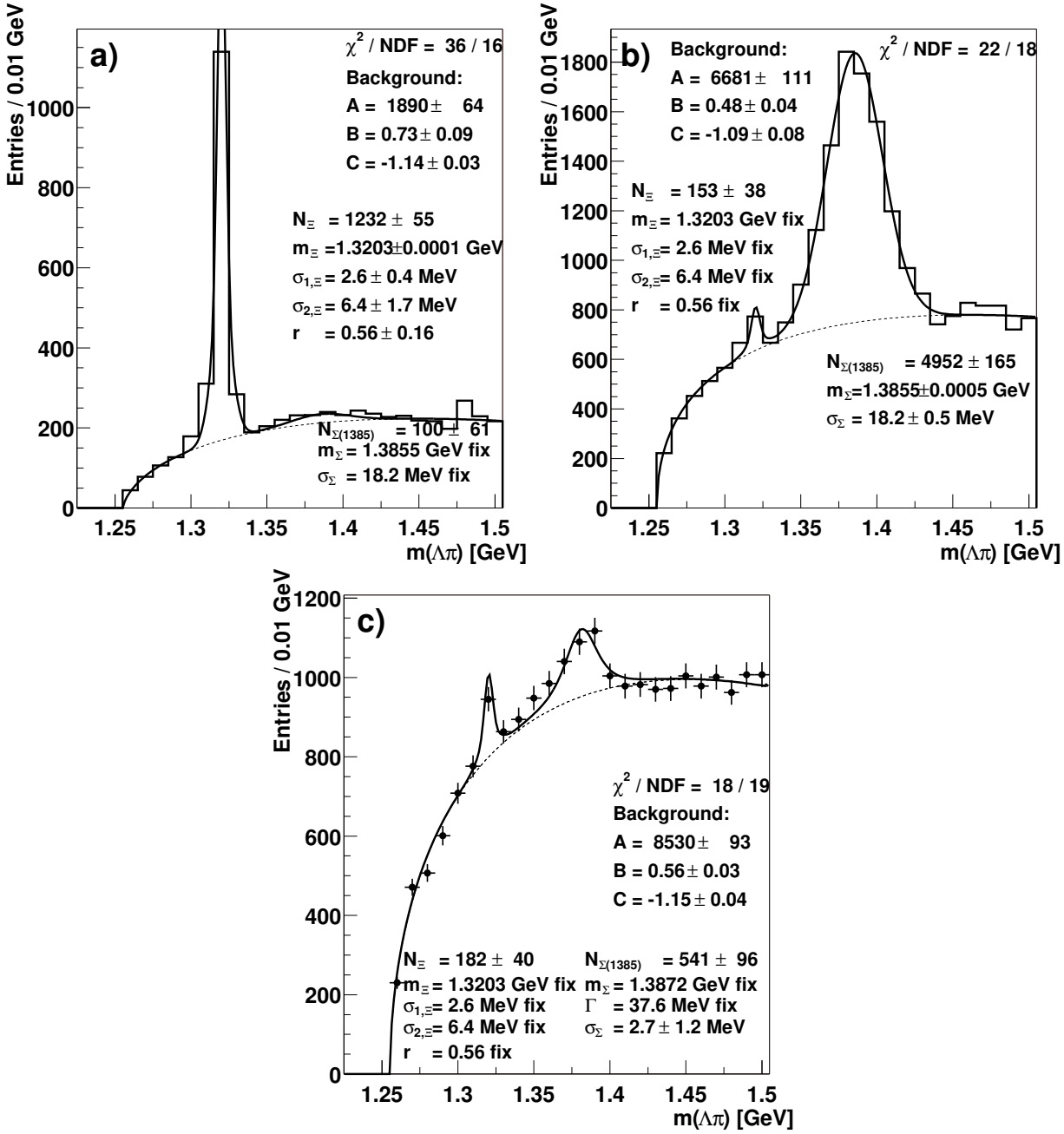

Figure 5.12: Mass distributions, $m(\Lambda\pi)$, of reconstructed Ξ^- and $\Sigma(1385)$ candidates in the (a) Ξ–MC, (b) Σ–MC and (c) data. The correct charge combination $Q(p) * Q(\pi) = -1$ for Ξ^- decays (see Tab. 5.2) is taken for the mass distribution of the CDM Ξ–MC, because the other charge combination does only contribute to the background and not to the Ξ^- signal. The full line shows the parameterisation which is found by the fit (Eq. 5.4), the dashed line represents the background parameterisation only. In the MC distributions the $\Sigma(1385)$ signal is parameterised by a Gaussian, while a Breit-Wigner function with the width Γ convoluted with a Gaussian with the width σ_Σ is used for the fit to the data. The mass and width of the Ξ^- and $\Sigma(1385)$ signal are free for the fit to the Ξ– and Σ–MC distribution, respectively, and the values found for the Ξ^- signal are fixed for the fit to the data to determine the number of Ξ^- and $\Sigma(1385)$.

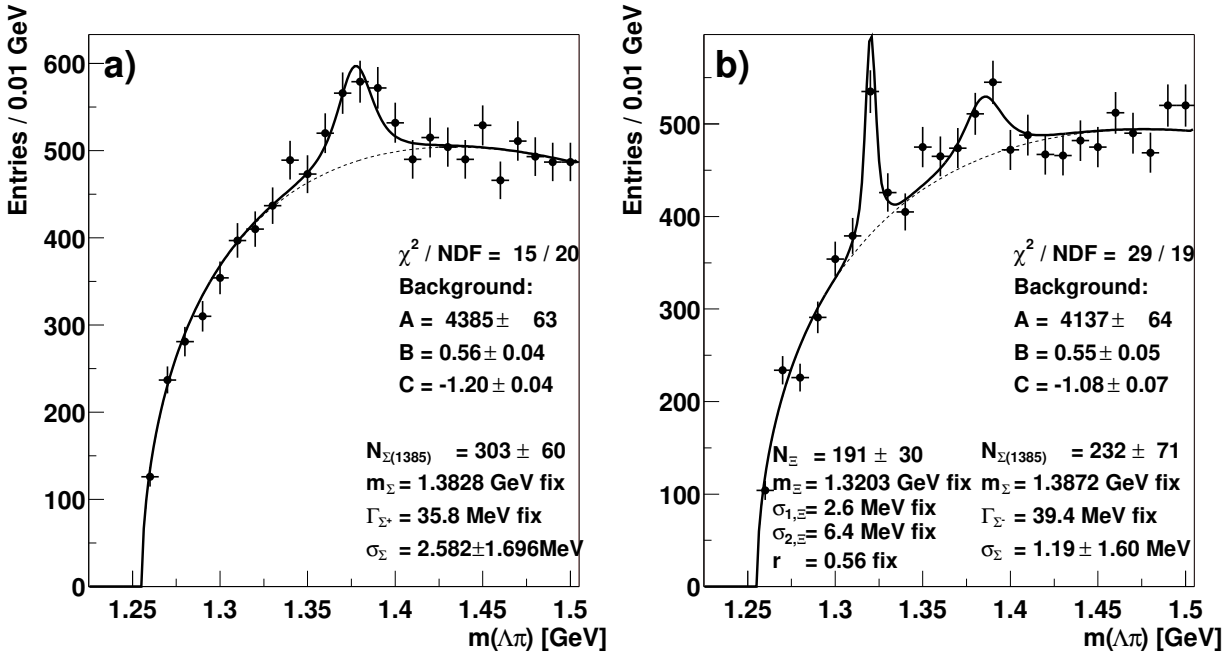

Figure 5.13: Mass distribution, $m(\Lambda\pi)$, of (a) $\Sigma(1385)^+$ and (b) $\Sigma(1385)^-$ baryon candidates. The total number of $\Sigma(1385)^+$ and $\Sigma(1385)^-$ in the signals is determined with a relativistic Breit-Wigner parameterisation convoluted with a Gaussian. The mass, m, and width, Γ, of the Breit-Wigner function are fixed to the global values [34], which are $m_{\Sigma(1385)^+} = 1.3828$ GeV, $\Gamma_{\Sigma(1385)^+} = 35.8$ MeV and $m_{\Sigma(1385)^-} = 1.3872$ GeV, $\Gamma_{\Sigma(1385)^-} = 39.4$ MeV for $\Sigma(1385)^+$ and $\Sigma(1385)^-$, respectively.

particle	Ξ^-	$\overline{\Xi}^+$	$\Sigma(1385)^-$	$\overline{\Sigma}(1385)^+$	$\Sigma(1385)^+$	$\overline{\Sigma}(1385)^-$
number	85 ± 21	105 ± 21	67 ± 52	170 ± 51	186 ± 43	116 ± 42

Table 5.3: Number of Ξ^-, $\overline{\Xi}^+$, $\Sigma(1385)^-$, $\overline{\Sigma}(1385)^+$, $\Sigma(1385)^+$ and $\overline{\Sigma}(1385)^-$ decays obtained by the fit to the corresponding mass distributions (Fig. 5.14).

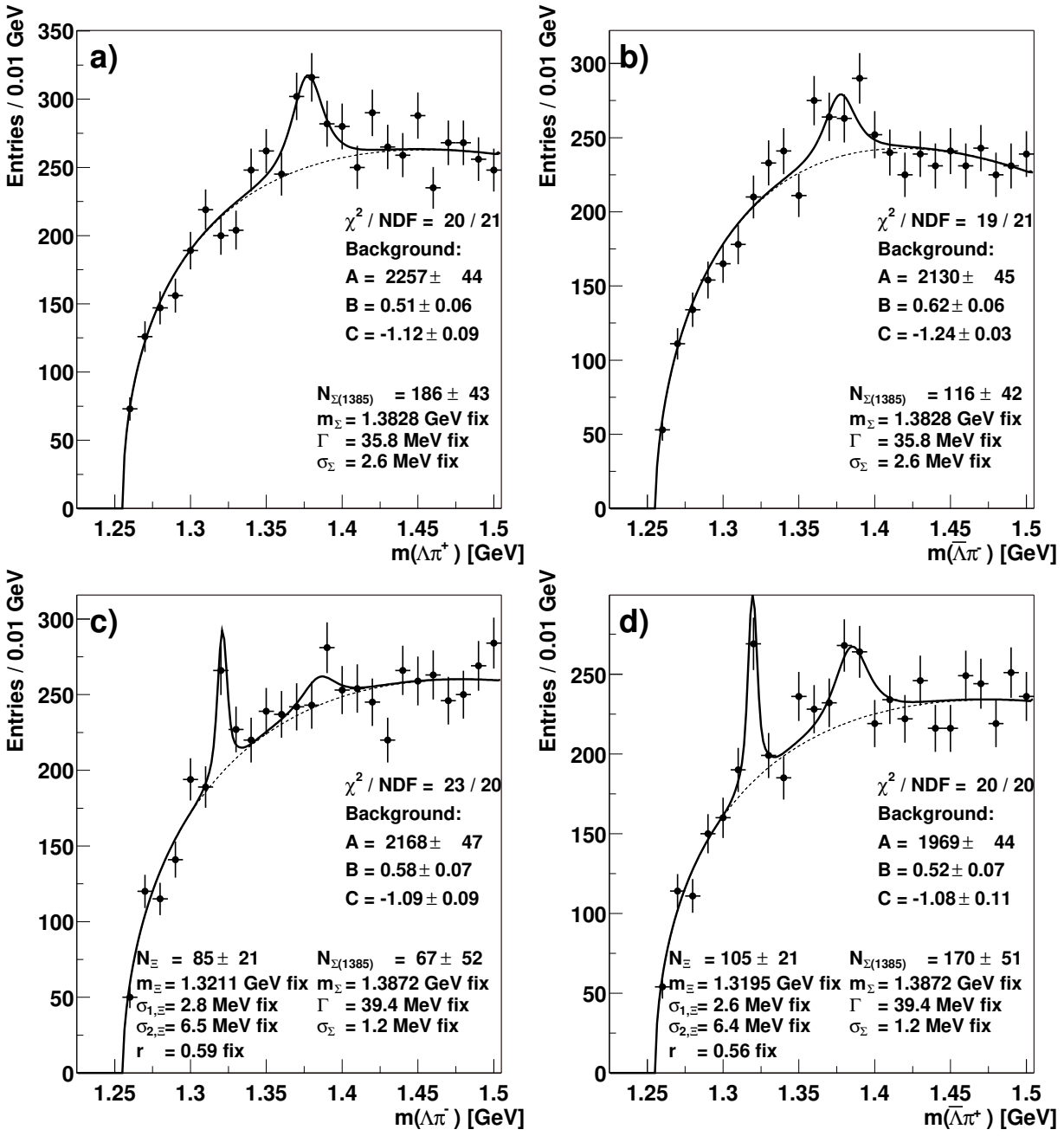

Figure 5.14: Mass distributions, $m(\Lambda\pi)$, for the decay channels (a) $\Lambda\pi^+$, (b) $\overline{\Lambda}\pi^-$, (c) $\Lambda\pi^-$ and (d) $\overline{\Lambda}\pi^+$. The full line shows the parameterisation which is found by the fit (Eq. 5.4), the dashed line represents the background parameterisation only. Since the decay channels into $\Lambda\pi^+$ and $\overline{\Lambda}\pi^-$ cannot have any Ξ^- signal (Tab. 5.2), the Gaussians for the Ξ^- signal are excluded from the fit.

(Fig. 5.15(a)) has 234 ± 68 $\Sigma(1385)$ baryons while the mass distribution of the $\overline{\Sigma}(1385)$ anti-baryon candidates (Fig. 5.15(b)) has 265 ± 62 $\overline{\Sigma}(1385)$ anti-baryons. The number of Ξ^- and $\Sigma(1385)$ baryons and $\overline{\Xi}^+$ and $\overline{\Sigma}(1385)$ anti-baryons is equal within the uncertainty.

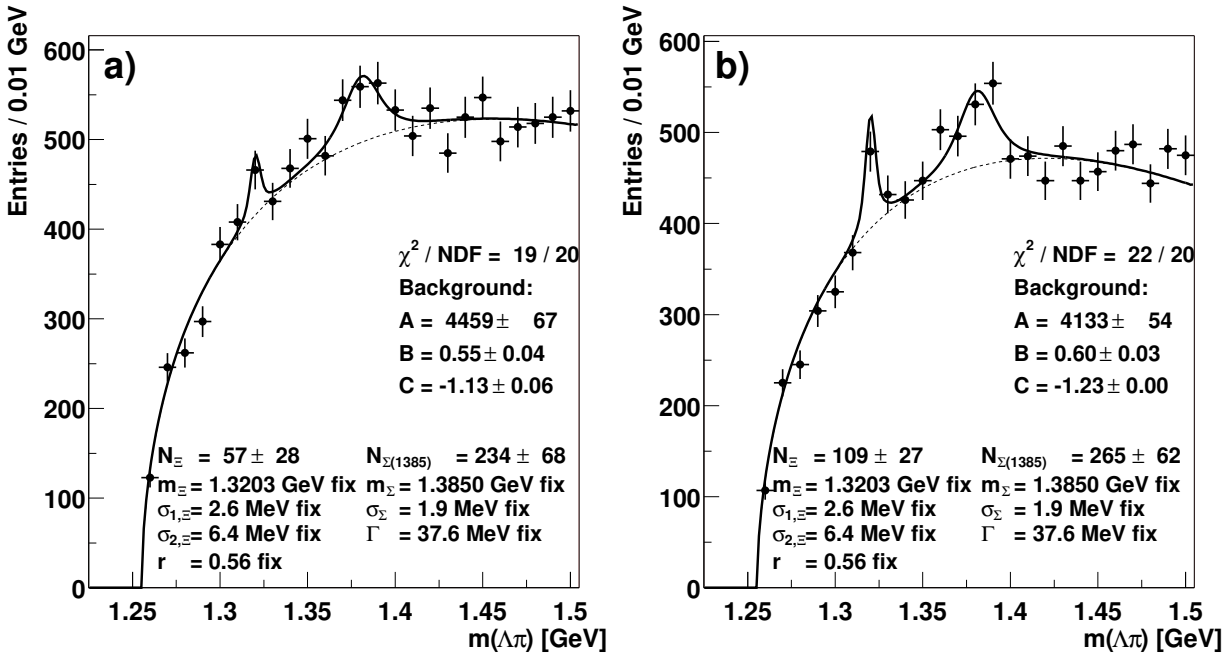

Figure 5.15: Mass distribution, $m(\Lambda\pi)$, of (a) $\Sigma(1385)^+$ and $\Sigma(1385)^-$ and (b) $\overline{\Sigma}(1385)^+$ and $\overline{\Sigma}(1385)^-$ candidates. The mass, m_Σ, and width, Γ, of the Breit-Wigner function are fixed to $m_{\Sigma(1385)^+} = 1.385$ GeV, $\Gamma_{\Sigma(1385)^+} = 37.4$ MeV, which are the mean of the global values [34] of these particles.

A number of consistency checks are performed. A DIS sample with slightly more statistics but not well simulated trigger chain can be used to verify the position and width of Ξ^-, $\Sigma(1385)^-$ and $\Sigma(1385)^+$ in the data itself but cannot be used to determine cross sections. For this sample the distance of the impact point of the positron on the calorimeter to the beam axis is lowered and a box cut of $X > 12$ cm and $Y > 6$ cm is required. The mass distribution of these events (Fig. 5.16(a), 5.17(a) and 5.18(a)) has 202 ± 31, 268 ± 75 and 293 ± 63 reconstructed Ξ^-, $\Sigma(1385)^-$ and $\Sigma(1385)^+$ baryons respectively, when using the fit Eq. 5.4. The charge combination $Q(p) * Q(\pi) = -1$ is taken to check the signal of Ξ^- and $\Sigma(1385)^-$ candidates, while the charge combination $Q(p) * Q(\pi) = +1$ is used to check the signal of $\Sigma(1385)^+$ baryon candidates (see Tab. 5.2). The fits to the mass distribution with mass and width kept as fit parameters give a reasonable description and the number of Ξ^-, $\Sigma(1385)^-$ and $\Sigma(1385)^+$ are consistent within the statistical errors (Tab. 5.4, 5.5 and 5.6):

	Figure	N_Ξ	m_Ξ (GeV)	$\sigma_{1,\Xi}$ (MeV)	$\sigma_{2,\Xi}$ (MeV)	r
1)	5.16(a)	202 ± 31	fixed	fixed	fixed	fixed
2)	5.16(b)	202 ± 31	1.3202 ± 0.0007	fixed	fixed	fixed
3)	5.16(c)	206 ± 35	fixed	2.8 ± 0.7	fixed	fixed
4)	5.16(d)	215 ± 33	fixed	fixed	8.1 ± 7.0	fixed
5)	5.16(e)	211 ± 42	fixed	fixed	fixed	0.48 ± 0.24
6)	5.17(c)	206 ± 53	—	—	—	—
7)	5.12(a)	—	1.3203 ± 0.0001	2.6 ± 0.4	6.4 ± 1.7	0.56 ± 0.16

Table 5.4: Results of the consistency checks for the sample with slightly higher statistics due to relaxed DIS selection cuts concerning the Ξ^- signal. The number of reconstructed Ξ^- baryons, N_Ξ, the found mass, m_Ξ, widths, $\sigma_{1,\Xi}$ and $\sigma_{2,\Xi}$, and r (see equation 5.4) are shown for the fit with (1) fixed mass, widths and parameter r, (2) fixed widths and r, (3) the first width, $\sigma_{1,\Xi}$, kept as a fit parameter, (4) the second width, $\sigma_{2,\Xi}$, kept as a fit parameter and (5) the parameter r kept as a fit parameter. (6) The number of Ξ^- is determined by counting the number of entries in the mass window of $1.30 < m(\Lambda\pi) < 1.34$ GeV and subtracting the number of background events given by the parameter A of the fit in the same range. The fixed values are taken from row (7) which are found by the fit to the Ξ–MC.

	Figure	N_Σ	m_Σ (GeV)	σ_Σ (MeV)
1)	5.17(a)	268 ± 75	fixed	1.9 ± 1.6
2)	5.17(b)	269 ± 75	1.387 ± 0.003	fixed to 1.9
3)	5.17(c)	205 ± 97	—	—
4)	—	—	1.3886 ± 0.0008	—

Table 5.5: Results of the consistency checks for the sample with slightly higher statistics due to relaxed DIS selection cuts concerning the $\Sigma(1385)^-$ signal. The number of reconstructed $\Sigma(1385)^-$ baryons, N_Σ, the found mass of the Breit-Wigner function, m_Σ, and width, σ_Σ, of the Gaussian, which is convoluted with the Breit-Wigner function, are shown for the fit with (1) the width, σ_Σ, kept as a fit parameter and (2) the mass kept as a free fit parameter and the width, σ_Σ, is fixed to the value which is found in row (1). (3) The number of $\Sigma(1385)^-$ is determined by counting the number of entries in the mass window of $1.34 < m(\Lambda\pi) < 1.43$ GeV and subtracting the number of background events given by the parameter A of the fit in the same range. The fixed mass, m_Σ, is taken from row (4) which is found by the fit to the Σ–MC.

	Figure	N_Σ	m_Σ (GeV)	σ_Σ (MeV)
1)	5.18(a)	293 ± 63	fixed	1.7 ± 1.8
2)	5.18(b)	293 ± 63	1.383 ± 0.004	fixed to 1.7
3)	5.18(c)	346 ± 99	—	—
4)	—	—	1.3834 ± 0.0006	—

Table 5.6: Results of the consistency checks for the sample with slightly higher statistics due to relaxed DIS selection cuts concerning the $\Sigma(1385)^+$ signal. The number of reconstructed $\Sigma(1385)^+$ baryons, N_Σ, the found mass of the Breit-Wigner function, m_Σ, and width, σ_Σ, of the Gaussian, which is convoluted with the Breit-Wigner function, are shown for the fit with (1) the width, σ_Σ, kept as a fit parameter and (2) the mass kept as a free fit parameter and the width, σ_Σ, is fixed to the value which is found in row (1). (3) The number of $\Sigma(1385)^+$ is determined by counting the number of entries in the mass window of $1.34 < m(\Lambda\pi) < 1.43$ GeV and subtracting the number of background events given by the parameter A of the fit in the same range. The fixed mass, m_Σ, is taken from row (4) which is found by the fit to the Σ–MC.

- The Ξ^- signal:
  The fit to the Ξ^- signal with the mass as a free parameter of the fit results in a Ξ^- mass of $m_\Xi = 1.3202 \pm 0.0007$ GeV and a number of 202 ± 31 Ξ^- (Fig. 5.16(b)). This is in good agreement with the global mass of $m_{\Xi^-} = 1.3213 \pm 0.0001$ GeV [34]. The predicted mass by the MC is $m_\Xi = 1.3203 \pm 0.0001$ GeV (Fig. 5.12(a)).
  The first width, $\sigma_{1,\Xi}$, of the Ξ^- signal is kept as a fit parameter. The Ξ^- signal contains 206 ± 35 Ξ^- baryons and prefers a width of $\sigma_{1,\Xi} = 2.8 \pm 0.7$ MeV (Fig. 5.16(c)). If the second width is kept as a fit parameter a number of 215 ± 33 Ξ^- baryons and a width of $\sigma_{2,\Xi} = 8.1 \pm 7.0$ MeV is obtained (Fig. 5.16(d)). Both widths have to be compared to the predicted values of the MC which are $\sigma_{1,\Xi} = 2.6 \pm 0.4$ MeV and $\sigma_{2,\Xi} = 6.4 \pm 1.7$ MeV. Experimental data and MC agree within the uncertainty. Fitting the parameter r of the Ξ^- signal in the data, it results in $r = 0.48 \pm 0.24$ and a number of 211 ± 42 Ξ^- baryons, respectively (Fig. 5.16(e)). In the MC the preferred value of r is $r = 0.56 \pm 0.16$. The number of reconstructed Ξ^- is calculated by subtracting the number of background events in the mass window of $1.30 < m(\Lambda\pi) < 1.34$ GeV, which is given by the fit, from the number of all entries in the same mass range. The number of reconstructed Ξ^- using this subtraction method is found to be 206 ± 53 (Fig. 5.18(c)).

- The $\Sigma(1385)^-$ signal:
  The $\Sigma(1385)^-$ mass as a free parameter of the fit and the width σ_Σ fixed to the value from the default fit (Fig. 5.18(b)) results in a number of 269 ± 75 $\Sigma(1385)^-$ and a mass of $m_\Sigma = 1.387 \pm 0.003$ GeV. The value found is reasonable and close to the mass preferred by the Σ–MC of $m_\Sigma = 1.3886 \pm 0.0006$ GeV and the global value of $m_\Sigma = 1.3872 \pm 0.0005$ GeV [34].
  The number of reconstructed $\Sigma(1385)^-$ is calculated by subtracting the number of

background events in the mass window of $1.34 < m(\Lambda\pi) < 1.43$ GeV, which is given by the fit, from the number of all entries in the same mass range. The number of reconstructed $\Sigma(1385)^-$ using this subtraction method is found to be 205 ± 97 (Fig. 5.18(c)).

- The $\Sigma(1385)^+$ signal:
  The $\Sigma(1385)^+$ mass as a free parameter of the fit and the width σ_Σ fixed to the value from the default fit (Fig. 5.18(b)) results in a number of 293 ± 63 $\Sigma(1385)^+$ and a mass of $m_\Sigma = 1.383 \pm 0.004$ GeV. The value found is reasonable and close to the mass preferred by the Σ–MC of $m_\Sigma = 1.3834 \pm 0.0006$ GeV and the global value of $m_\Sigma = 1.3828 \pm 0.0004$ GeV [34].
  The number of reconstructed $\Sigma(1385)^+$ is calculated by subtracting the number of background events in the mass window of $1.34 < m(\Lambda\pi) < 1.43$ GeV, which is given by the fit, from the number of all entries in the same mass range. The number of reconstructed $\Sigma(1385)^+$ using this subtraction method is found to be 346 ± 99 (Fig. 5.18(c)).

These checks are all consistent within the statistical errors and show that the calculation of the number of reconstructed Ξ^-, $\Sigma(1385)^-$ and $\Sigma(1385)^+$ baryons is reasonable.

The experimental data can be used to check if the global event kinematics are reconstructed in good agreement with MC predictions. The Ξ– and Σ–MC have at least one Ξ^- and $\Sigma(1385)$, respectively, in every event which is of course not the case for the data sample. Thus a perfect agreement is not expected since both samples differ. However, both samples are as equal as possible if only events are chosen which have a reconstructed mass below the Ξ^- and $\Sigma(1385)$ signal. The chosen range of the reconstructed mass is $1.3 < m(\Lambda\pi) < 1.45$ GeV. Several distributions which are important for DIS event (Fig. 5.19), primary vertex (Fig. 5.20) and Λ candidate reconstruction (Fig. 5.22) are compared with Ξ– and Σ–MC simulation. The MC distributions are scaled to the area below the data distribution. The comparisons show a reasonable agreement between data and MC which makes the simulation reliable. The shift in the $E - P_Z$ distribution is obvious but not a problem since the cuts are made at the tails (Fig. 5.19(b)). The effect of the systematic shift is considered as a systematic uncertainty (chapter 6). The distributions of the transverse momentum and pseudorapidity of the primary vertex fitted pion are well simulated by both MCs (Fig. 5.21).

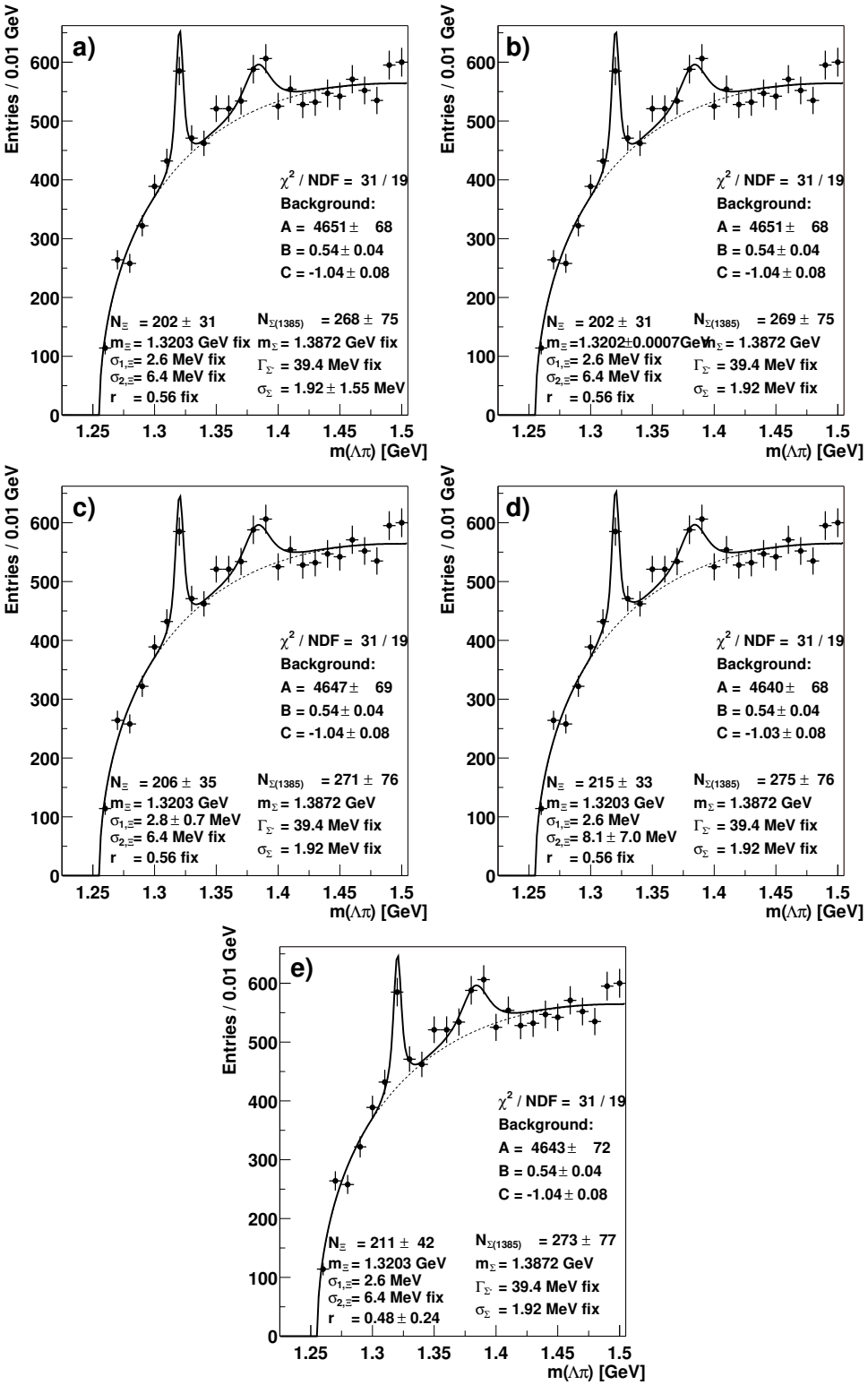

Figure 5.16: Mass distribution, $m(\Lambda\pi)$, for a sample with slightly higher statistics due to relaxed DIS selection cuts. All plots show the same data with the correct charge combination, $Q(p) * Q(\pi) = -1$, for Ξ^- decays (see Tab. 5.2) but different fits which are always presented by the full line. The dashed line is the parameterisation of the background only. The fit is processed by (a) fixing the mass, m_Ξ, widths, $\sigma_{1,\Xi}$ and $\sigma_{2,\Xi}$, and parameter r of the Ξ^- signal to the values found by the Monte Carlo, (b) keeping the mass, m_Ξ, as a fit parameter, (c) keeping the first width, $\sigma_{1,\Xi}$, as a fit parameter, (d) keeping the second width, $\sigma_{2,\Xi}$, as a fit parameter and (e) keeping the parameter r as a fit parameter.

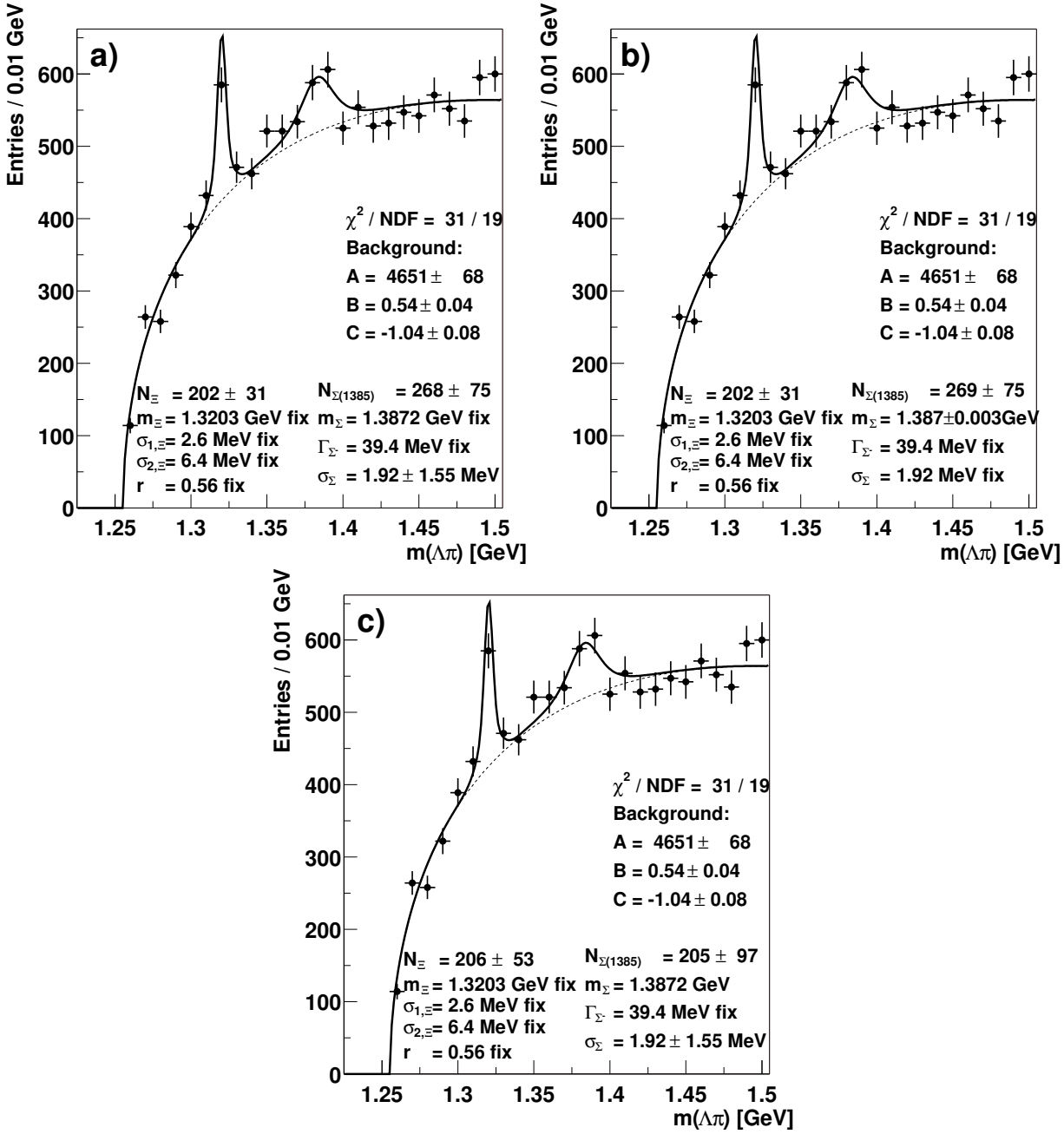

Figure 5.17: Mass distribution $m(\Lambda\pi)$ for a sample with higher statistics due to relaxed DIS selection cuts. All plots show the same data with the correct charge combination, $Q(p) * Q(\pi) = -1$, for $\Sigma(1385)^-$ decays (see Tab. 5.2) but different fits which are always presented by the full line. The dashed line is the parameterisation of the background only. The fit is processed by (a) fixing the mass, m_Σ, to the global value of $m_\Sigma = 1.3872$ GeV and keeping the width, σ_Σ, of the Gaussian convoluted with the Breit-Wigner as a fit parameter and (b) fixing the width, σ_Σ, but keeping the mass, m_Σ, of the $\Sigma(1385)^-$ signal as a fit parameter. (c) The number of Ξ^- and $\Sigma(1385)^-$ is calculated by counting all events in the mass window of $1.30 < m(\Lambda\pi) < 1.34$ GeV and $1.34 < m(\Lambda\pi) < 1.43$ GeV, respectively, and subtracting the number of background events in the same range determined by the fit.

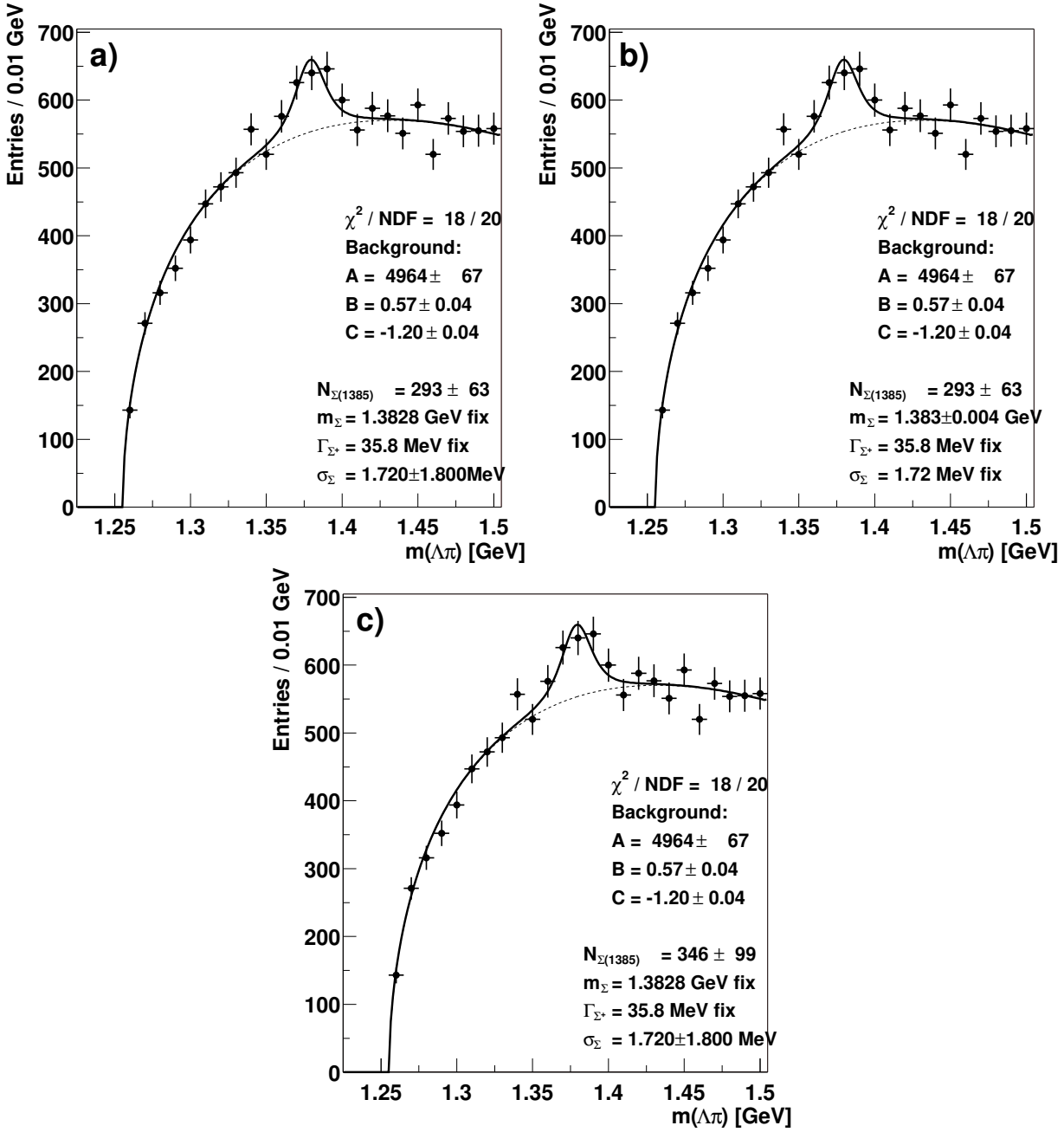

Figure 5.18: Mass distribution $m(\Lambda\pi)$ for a sample with higher statistics due to relaxed DIS selection cuts. All plots show the same data with the correct charge combination, $Q(p) * Q(\pi) = +1$, for $\Sigma(1385)^+$ decays (see Tab. 5.2) but different fits which are always presented by the full line. The dashed line is the parameterisation of the background only. The fit is processed by (a) fixing the mass, m_Σ, to the global value of $m_\Sigma = 1.3828$ GeV and keeping the width, σ_Σ, of the Gaussian convoluted with the Breit-Wigner as a fit parameter and (b) fixing the width, σ_Σ, but keeping the mass, m_Σ, of the $\Sigma(1385)^-$ signal as a fit parameter. (c) The number of $\Sigma(1385)^+$ is calculated by counting all events in the mass window of $1.34 < m(\Lambda\pi) < 1.43$ GeV and subtracting the number of background events, A, in the same range determined by the fit,

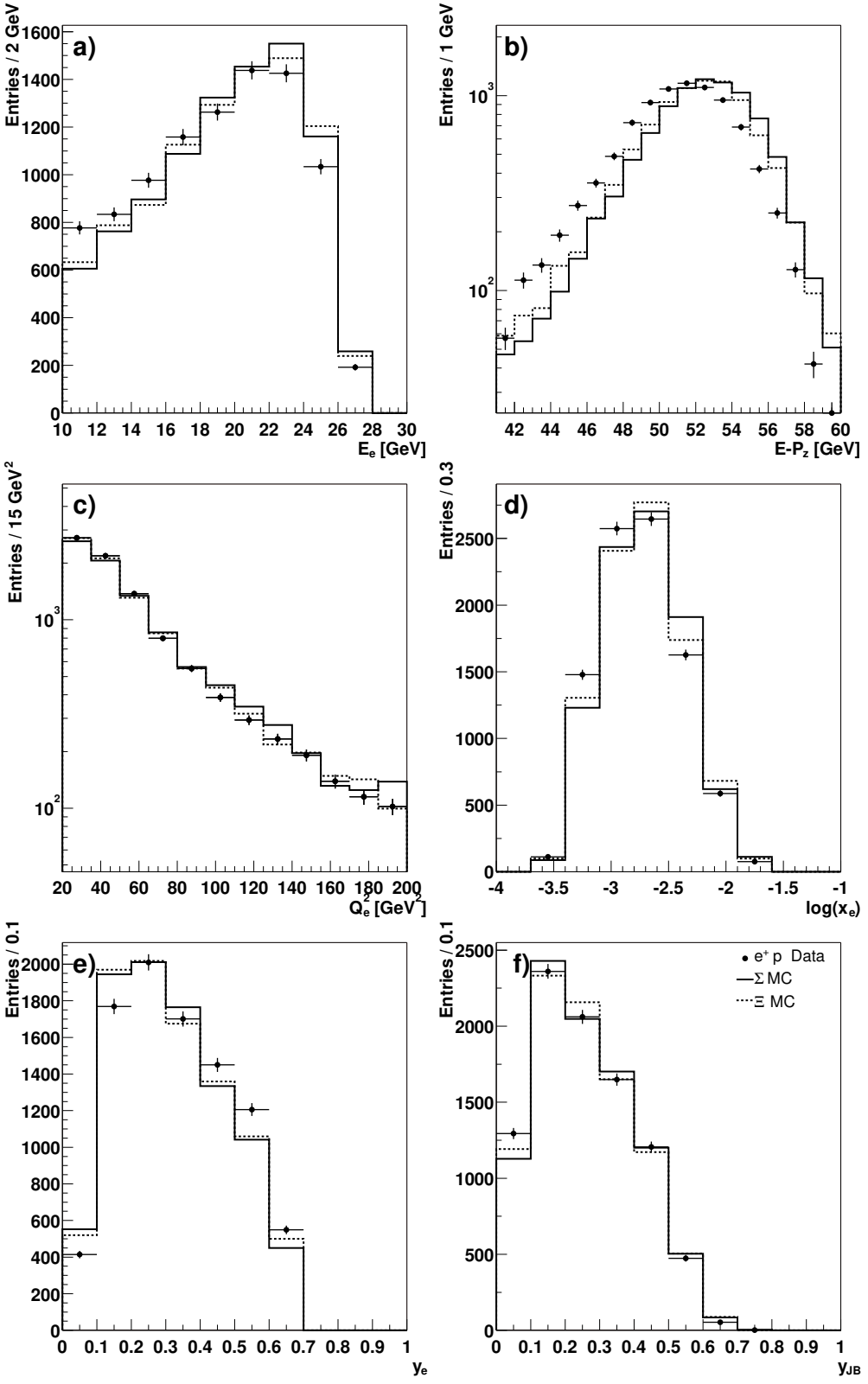

Figure 5.19: The distributions of (a) the energy of the scattered electron, $E_{e'}$, the quantities (b) $E - P_Z$, (c) Q_e^2, (d) $\log(x_e)$, (e) y_e and (f) y_{JB} below the Ξ^- and $\Sigma(1385)$ signal in the mass window of $1.3 < m(\Lambda\pi) < 1.45$ GeV are presented for data (points), CDM Ξ–MC (dashed histogram) and Σ–MC (full histogram). In each case the MC distribution is scaled to the area below the data distribution. All cuts listed in the text are applied.

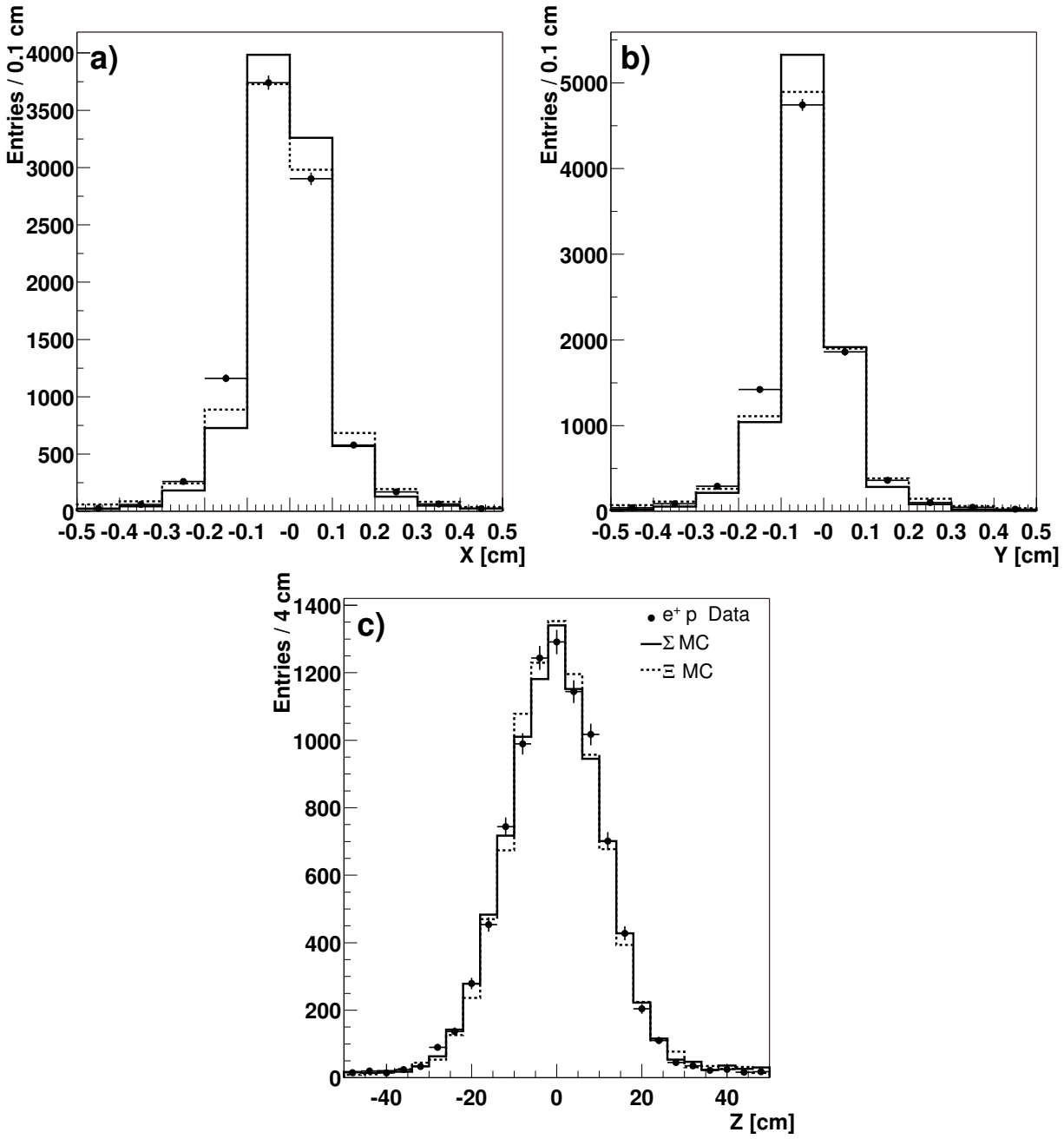

Figure 5.20: The distributions of the (a) X, (b) Y and (c) Z component of the reconstructed primary vertex below the Ξ^- and $\Sigma(1385)$ signal in the mass window of $1.3 < m(\Lambda\pi) < 1.45$ GeV are shown for data (points), CDM Ξ–MC (dashed histogram) and Σ–MC (full histogram). In each case the MC distribution is scaled to the area below the data distribution. All cuts listed in the text are applied.

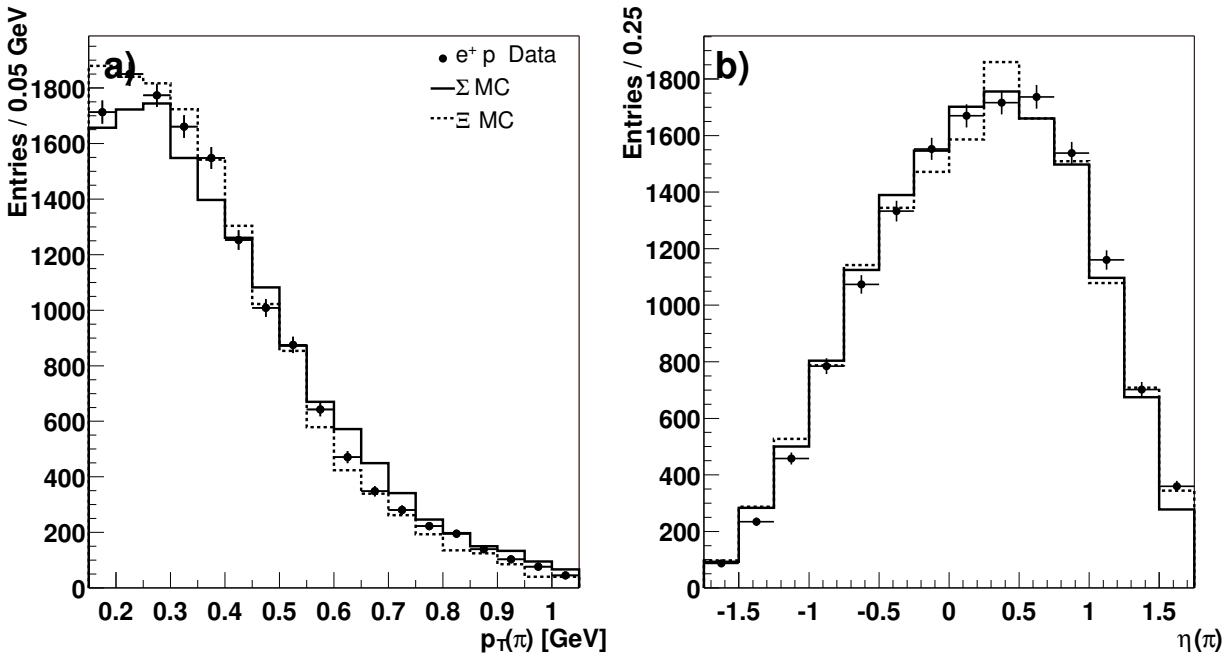

Figure 5.21: The distributions of (a) the transverse momentum, $p_T(\pi)$, and (b) pseudorapidity, $\eta(\pi)$, of the primary vertex fitted pion candidate in the laboratory system below the Ξ^- and $\Sigma(1385)$ signal in the mass window of $1.3 < m(\Lambda\pi) < 1.45$ GeV are presented for data (points) and CDM Ξ–MC (dashed histogram) and Σ–MC (full histogram). In each case the MC distribution is scaled to the area below the data distribution. All cuts listed in the text are applied.

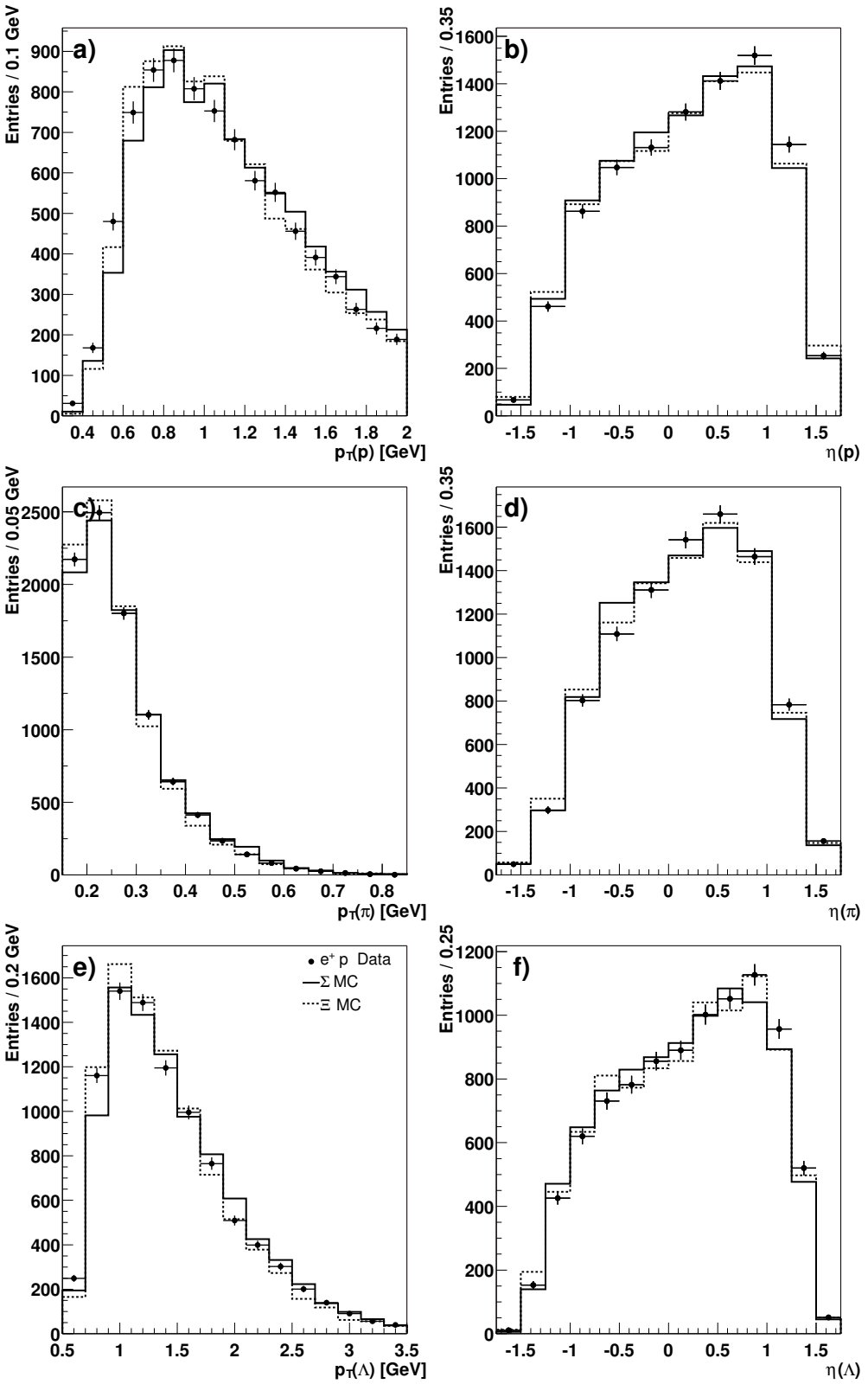

Figure 5.22: The distributions of (left) the transverse momentum and (right) the pseudorapidity of the (top) proton, (middle) pion, which is combined to a Λ candidate, and (bottom) Λ candidate below the Ξ^- and $\Sigma(1385)$ signal in the mass window of $1.3 < m(\Lambda\pi) < 1.45$ GeV are presented for data (points), CDM Ξ–MC (dashed histogram) and Σ–MC (full line) in the laboratory system. In each case the MC distribution is scaled to the area below the data distribution. All cuts listed in the text are applied.

Chapter 6

Definition of cross sections and systematic uncertainties

The cross section for a given observable Y is determined from

$$\frac{d\sigma}{dY} = \frac{N}{A \cdot \mathcal{L} \cdot B \cdot B_\Lambda \cdot \Delta Y},$$

where N is the number of events with a Ξ^- ($\Sigma(1385)$) baryon determined from the corresponding fit described in chapter 5 in a bin of size ΔY, $B_\Lambda = 0.639 \pm 0.005$ is the branching ration of $\Lambda \to p\pi^-$, $\mathcal{L}$ is the integrated luminosity and A is the acceptance. The acceptance is defined as the number of reconstructed Ξ^- and $\Sigma(1385)$ in a certain bin ΔY divided by the number of generated Ξ^- and $\Sigma(1385)$, respectively, for that bin. Since experimental data and MC agree, the acceptance takes into account migrations, efficiencies and radiative effects for that bin.

The decay $\Xi^- \to \Lambda\pi$ has a well known branching ratio of $B = 0.9989 \pm 0.0004$ [34], and $\Sigma(1385)$ has a branching ratio of $B = 0.88 \pm 0.02$ [34] for $\Sigma\,(1385) \to \Lambda\pi$.

The systematic uncertainties on the measured cross sections are estimated from the following and the contribution from each item can be found in Tab. 6.1:

- Systematic checks were performed by varying the cuts on y_e, y_{JB}, $E - P_Z$ and the vertex position: from $y_e < 0.7$ to $y_e < 0.65$, from $y_{JB} > 0.04$ to $y_{JB} > 0.05$, from $41 < E - P_Z < 60$ GeV to $43 < E - P_Z < 58$ GeV and from $|Z_{vtx}| < 50$ cm to $|Z_{vtx}| < 45$ cm. The radius cut, r_e, for the position of the scattered positron in the calorimeter was raised from 36 cm by 1 cm to 37 cm. The minimum value of the energy of the scattered lepton was increased by 1 GeV. Since the reconstruction of the kinematic variables is based on the electron method, the positron energy scale was raised by 2%, which is the uncertainty of the electromagnetic energy calibration [44].

- The minimum transverse momentum for all reconstructed charged tracks were changed. The transverse momentum resolution of a track with $p_T = 150$ MeV traversing all nine superlayers is 11 MeV (chapter 3). Since only three superlayers are required in this analysis a conservative value for the resolution of 20 MeV is assumed. So the minimum p_T for the p and π of the Λ reconstruction and the π for the Ξ^- and $\Sigma(1385)$ reconstruction is raised from 150 MeV by 20 MeV, respectively.

- The default Λ candidate mass window of $1.112 < m(p\pi) < 1.119$ GeV was chosen to be both more narrow and wider: $1.113 < m(p\pi) < 1.118$ GeV and $1.110 < m(p\pi) < 1.121$ GeV.

- The width of the Ξ^- signal was increased by one standard deviation of the width found by the fit to the Ξ–MC mass distribution. Thus, the uncertainty of the width introduced by the MC is taken into account.

In addition, systematic uncertainties are estimated differently due to the different reconstruction approaches:

Further systematic uncertainties for the identification of Ξ^- measurement with reconstructed displaced tertiary vertices

- The first two and last two bins were omitted from the fit.

- The number of entries in the signal sample in the mass window of $1.305 < m(\Lambda\pi) < 1.345$ GeV is subtracted by the number of entries in the scaled wrong charge mass distribution in the same mass window.

- The cuts for the reconstruction of displaced tertiary vertices are varied: from $|dca_Z| < 1.5$ cm to $|dca_Z| < 1$ cm and $|dca_Z| < 2$ cm, from $dca < 2.5$ cm to $dca < 2$ cm and $dca < 3$ cm and from $r(\Xi^-) > 1.75$ cm to $r(\Xi^-) > 1.25$ cm and $r(\Xi^-) > 2.25$ cm.

- The cross section is determined with a full simulated HERWIG Monte Carlo instead of DJANGOH using ARIADNE.

Further systematic uncertainties for the Ξ^- and $\Sigma(1385)$ measurement with primary vertex fitted tracks

- The first one and last two bins were omitted from the fit

- The background is parameterised by a different function: $Bg_{B,C} = m_{diff}^{B} * e^{(C \cdot m_{diff})}$

- HERWIG does not simulate the mass distribution of $\Sigma(1385)$ properly. Therefore the systematic uncertainty of the acceptance is taken from the measurement with reconstructed displaced tertiary vertices.

The overall systematic uncertainty is determined by adding the above uncertainties in quadrature. The normalisation uncertainties due to the $\Xi^- \to \Lambda\pi$ ($\Sigma(1385) \to \Lambda\pi$) decay branching ration of $\pm 0.04\%$ ($\pm 2\%$) [34] and due to the luminosity measurement error are not included in the systematic uncertainties.

systematic check	contribution		
	Ξ^- (dtv)	Ξ^- (pvt)	$\Sigma(1385)$
$y_e < 0.65$	-3.8%	$(\pm 0.8\%)^\bullet$	-3.5%
$y_{JB} > 0.05$	$(^{+0.3\%}_{-0.6\%})^\bullet$	-5.2%	-3.1%
$43 < E - P_Z < 58$ GeV	$(^{+0.9\%}_{-2.3\%})^\bullet$	$(^{+1.6\%}_{-0.8\%})^\bullet$	-3.7%
$\lvert Z_{vtx}\rvert < 45$ cm	$(^{+0.3\%}_{-0.7\%})^\bullet$	$(\pm 0.7\%)^\bullet$	-1.3%
r_e raised by 1 cm	$+1.3\%$	$(+1.3\%)^\star$	$+4.7\%$
$E_{e'} > 11$ GeV	-3.5%	-1.8%	-1.7%
energy scale raised by 2%	$+1.2\%$	$(+1.2\%)^\star$	$+0.7\%$
$p_T(p,\pi) > 170$ MeV	$(\pm 2.0\%)^\bullet$	$(\pm 2.0\%)^\bullet$	$+9.4\%$
$p_T(\pi^{1st}) > 170$ MeV	$+1.6\%$	-6.3%	-1.5%
change of Λ mass window	-5.2%	-4.5%	-5.0%
1^{st} width of Ξ^- signal increased/lowered	$\pm 0.5\%$	$\pm 4.2\%$	$\pm 0.2\%$
2^{nd} width of Ξ^- signal increased/lowered	$\pm 0.4\%$	$\pm 6.2\%$	$\pm 0.9\%$
omitted bins	$+1.4\%$	$(^{+0.8\%}_{-0.2\%})^\bullet$	$+1.5\%$
different background subtraction	$+9.7\%$	-0.8%	-2.5%
$\lvert dca_Z\rvert < 1$ cm	$(+1.3\%)^\dagger$	—	—
$\lvert dca_Z\rvert < 2$ cm	-1.2%	—	—
$dca < 2$ cm	$(-1.2\%)^\dagger$	—	—
$dca < 3$ cm	$(+0.8\%)^\dagger$	—	—
$r(\Xi^-) > 1.25$ cm	$(+0.2\%)^\dagger$	—	—
$r(\Xi^-) > 2.25$ cm	$(-1.2\%)^\dagger$	—	—
HERWIG instead of ARIADNE	$+11.4\%$	$+11.4\%$	
total systematic uncertainty	$^{+15.5\%}_{-8.3\%}$	$^{+14.1\%}_{-12.4\%}$	$^{+15.6\%}_{-8.6\%}$

Table 6.1: The contribution of each systematic check, which is explained in the text in detail, is listed. The contributions are given for the identification of Ξ^- baryons with reconstructed displaced tertiary vertices (dtv) as explained in chapter 5.2, with primary vertex fitted tracks (pvt) as explained in chapter 5.3 and for the $\Sigma(1385)$ baryon reconstruction, respectively. For a few systematic checks concerning the Ξ^- reconstruction the statistical uncertainty of the systematic error is bigger than the systematic shift and compatible with zero. In these cases the systematic error is quoted in parentheses and estimated in the following ways:

* If the systematic uncertainty of the pvt approach is compatible with zero but in agreement with the systematic uncertainty of the dtv approach within the statistical uncertainty, the uncertainty of the dtv approach is taken for the pvt approach and vice versa.

$^\bullet$ If the systematic shift is compatible with zero and not in agreement with the systematic shift of the other approach, a conservative systematic is taken in such a way, that the statistical uncertainty of the systematic sets the systematic uncertainty.

† The calculated systematic uncertainty it taken although it is compatible with zero, because no other conservative estimate can be made.

Chapter 7

Inclusive Ξ^- and $\Sigma(1385)$ baryon cross sections in a restricted kinematic region

7.1 Total inclusive Ξ^- and $\Sigma(1385)$ baryon cross sections in a restricted kinematic region

The identification of Ξ^- baryons can be done in two different ways: with reconstructed displaced tertiary vertices (*dtv*) (chapter 5.2) and with primary vertex fitted tracks (*pvt*) (chapter 5.3). Both methods allow the measurement of the total Ξ^- cross section and can be used to calculate an error weighted combined cross section. The identification of $\Sigma(1385)$ baryons is performed with the *pvt* approach.

7.1.1 Total inclusive Ξ^- baryon cross section in a restricted $p_T(\Xi^-)$ and $\eta(\Xi^-)$ kinematic region

The overall acceptance of Ξ^- baryons identified with *dtv* for $20 < Q^2 < 200$ GeV^2, $3{\cdot}10^{-4} < x < 2 \cdot 10^{-2}$, $0.04 < y < 0.7$, $1.0 < p_T(\Xi^-) < 5.0$ GeV and $|\eta(\Xi^-)| < 1.5$, estimated with DJANGOH using ARIADNE and HERWIG is found to be $3.5\% \pm 0.1\%$ and $3.1\% \pm 0.1\%$, respectively. Since ARIADNE provides the best description of the observed hadronic final state in inclusive DIS [41], this acceptance is used to determine the total measured Ξ^- baryon cross section in the restricted kinematic region, where Ξ^- includes Ξ^- and $\overline{\Xi}^+$:

$$\sigma_{dtv}(e^+p \to e^+\Xi^- X) = 83 \pm 9(\text{stat.})^{+13}_{-7}(\text{syst.}) \text{ pb}.$$

In the same kinematic range the overall Ξ^- baryon acceptance, reconstructed with the *pvt* approach, is estimated with DJANGOH using ARIADNE and found to be $3.4\% \pm 0.1\%$. The total measured Ξ^- baryon cross section with this approach is

$$\sigma_{pvt}(e^+p \to e^+\Xi^- X) = 89 \pm 15(\text{stat.})^{+13}_{-11}(\text{syst.}) \text{ pb},$$

where Ξ^- includes Ξ^- and $\overline{\Xi}^+$.

An error weighted combined total Ξ^- baryon cross section is

$$\sigma(e^+p \to e^+\Xi^- X) = 85 \pm 7(\text{stat.})^{+13}_{-8}(\text{syst.})\ \text{pb},$$

where Ξ^- includes Ξ^- and $\overline{\Xi}^+$.

The statistical error for a separate measurement of Ξ^- and $\overline{\Xi}^+$ increases wrt. the total Ξ^- baryon cross section due to the halved statistics. However, the systematic uncertainties can be minimized by measuring the ratio, $N_{\Xi^-}/N_{\Xi_{all}}$ ($N_{\overline{\Xi}^+}/N_{\Xi_{all}}$), of the number of reconstructed Ξ^- ($\overline{\Xi}^+$), N_{Ξ^-} ($N_{\overline{\Xi}^+}$), to the number of all reconstructed Ξ^- baryons, N_{all}, because many systematics cancel. The systematic uncertainty of the ratios is determined from the change of the following cuts which are sensitive to the reconstruction of the particles: a) change of the p_T of all particles measured with the CTD, b) change of the selected mass window of reconstructed Λ candidates, c) change of the cuts of dca, dca_Z and $r(\Xi^-)$ and d) changes of the fit procedure (omitted bins, change of the width of the Ξ^- signal, different background parameterisation) (detailed description in chapter 6). All systematic checks are compatible with zero within the statistical uncertainties. Since it is expected that the systematics cancel in the ratio, no systematic uncertainty is stated. The ratios agree within the errors (Tab. 7.2).

7.1.2 Total inclusive $\Sigma(1385)$ baryon cross sections in a restricted $p_T(\Sigma\,(1385))$ and $\eta(\Sigma\,(1385))$ kinematic region

The overall $\Sigma(1385)$ baryon acceptance for $20 < Q^2 < 200$ GeV^2, $3 \cdot 10^{-4} < x < 2 \cdot 10^{-2}$, $0.04 < y < 0.7$, $1.0 < p_T(\Sigma\,(1385)) < 5.0$ GeV and $|\eta(\Sigma\,(1385))| < 1.5$, estimated with DJANGOH using ARIADNE is $8.9\% \pm 0.3\%$. The total $\Sigma(1385)$ baryon cross section in this region is measured to be

$$\sigma(e^+p \to e^+\Sigma\,(1385)\,X) = 110 \pm 20(\text{stat.})^{+17}_{-10}(\text{syst.})\ \text{pb},$$

where $\Sigma(1385)$ includes $\Sigma(1385)^+$, $\overline{\Sigma}(1385)^-$, $\Sigma(1385)^-$ and $\overline{\Sigma}(1385)^+$.

The total $\Sigma(1385)^+$ and $\Sigma(1385)^-$ baryon cross section in this region are measured to be

$$\sigma(e^+p \to e^+\Sigma(1385)^+X) = 61 \pm 12(\text{stat.})^{+10}_{-5}(\text{syst.})\ \text{pb}$$

and

$$\sigma(e^+p \to e^+\Sigma(1385)^-X) = 49 \pm 15(\text{stat.})^{+8}_{-4}(\text{syst.})\ \text{pb},$$

respectively, where $\Sigma(1385)^+$ includes $\Sigma(1385)^+$ and $\overline{\Sigma}(1385)^-$, while $\Sigma(1385)^-$ includes $\Sigma(1385)^-$ and $\overline{\Sigma}(1385)^+$.

The total measured $\Sigma(1385)$ baryon and $\overline{\Sigma}(1385)$ anti-baryon cross section in this region are measured to be

$$\sigma(e^+p \to e^+\Sigma(1385)X) = 47 \pm 14(\text{stat.})^{+7}_{-4}(\text{syst.})\ \text{pb}$$

and

$$\sigma(e^+p \to e^+\overline{\Sigma}(1385)X) = 55 \pm 13(\text{stat.})^{+9}_{-5}(\text{syst.})\ \text{pb},$$

respectively, where $\Sigma(1385)$ includes $\Sigma(1385)^+$ and $\Sigma(1385)^-$, while $\overline{\Sigma}(1385)$ includes $\overline{\Sigma}(1385)^+$ and $\overline{\Sigma}(1385)^-$. Baryon and anti-baryon cross section agree within the uncertainties.

The systematic uncertainties for the cross sections of $\Sigma(1385)^+$, $\Sigma(1385)^-$, $\Sigma(1385)$ and $\overline{\Sigma}(1385)$ stated above cannot be estimated for each measurement separately, because already for the total $\Sigma(1385)$ baryon cross section the statistical fluctuations cover the real systematic uncertainty. With less statistics, after dividing the experimental data in mass distributions of $\Sigma(1385)^+$, $\Sigma(1385)^-$, $\Sigma(1385)$ and $\overline{\Sigma}(1385)$, respectively, no reliable estimate is possible. Therefore the quoted systematic uncertainties are taken from the total cross sections (chapter 6).

The ratios $N_{\Sigma(1385)^+}/N_{\Sigma(1385)}$, $N_{\overline{\Sigma}(1385)^-}/N_{\Sigma(1385)}$, $N_{\Sigma(1385)^-}/N_{\Sigma(1385)}$ and $N_{\overline{\Sigma}(1385)^-}/N_{\Sigma(1385)}$, of the reconstructed number, N, of $\Sigma(1385)^+$, $\overline{\Sigma}(1385)^-$, $\Sigma(1385)^-$ and $\overline{\Sigma}(1385)^+$, respectively, to the total number of reconstructed $\Sigma(1385)$ baryons , $N_{\Sigma(1385)}$, is measured (Tab. 7.2). The systematic uncertainty of the ratios is determined from the change of the following cuts which are sensitive to the reconstruction of the particles: a) change of the p_T of all particles measured with the CTD, b) change of the selected mass window of reconstructed Λ candidates and c) changes of the fit procedure (omitted bins, change of the width of the Ξ^- signal, different background parameterisation) (detailed description in chapter 6). Not all systematics cancel completely. A systematic uncertainty of about 4% remains from the change of the selected Λ mass window and the acceptance is not the same for all four decay channels. The acceptance of reconstructed $\overline{\Sigma}(1385)^+$ baryons is about 15% lower than the mean acceptance which corresponds to a systematic uncertainty of the ratio, $N_{\overline{\Sigma}(1385)^+}/N_{\Sigma(1385)}$, of about 10%.

7.1.3 Comparison of the measurement and prediction of the total inclusive cross sections

Both cross sections and the ratio of the cross sections, $R = \sigma(e^+p \to e^+\Sigma\,(1385)\,X)/\sigma(e^+p \to e^+\Xi^-X)$, are compared to the predictions of ARIADNE, LEPTO, both interfaced with HERACLES in order to incorporate first-order electroweak corrections, and HERWIG, all using the CTEQ5D structure function (Tab. 7.1). The first-order electroweak corrections have an effect of $+0.8\%$ and -1.7% on the cross section which is predicted for Ξ^- and $\Sigma(1385)$, respectively. The ARIADNE and LEPTO model with the LEP default strangeness suppression factor $\gamma_s = 0.3$ overestimate both cross sections, HERWIG overestimates the cross section even more than ARIADNE and LEPTO. The measured cross section of the Ξ^- baryon production is about 1.3 and of the $\Sigma(1385)$ baryon production about 6.5 standard deviations lower than the simulated by ARIADNE and LEPTO.

The total cross sections in the experimental data and the MC models do not agree with the default settings. However the ratio of the cross sections, $R = \sigma(e^+p \to e^+\Sigma\,(1385)\,X)/\sigma(e^+p \to$

$e^+\Xi^- X$), is independent of the normalisation of the cross sections and could be reasonably predicted by the MC models. The measured ratio is found to be $R = 1.3 \pm 0.3$. The uncertainty is propagated from the statistical errors of both cross sections. HERWIG predicts a ratio of $R = 3.3$, while LEPTO and ARIADNE forecast a ratio of $R = 2.6$, all of which do not agree with the measurement.

	γ_s	γ_{spin1}	$\gamma_{SU(6)}$	$\sigma(e^+p \to e^+\Xi^- X)$ (pb)	$\sigma(e^+p \to e^+\Sigma\,(1385)\,X)$ (pb)	R
ZEUS				$85 \pm 7^{+13}_{-8}$	$110 \pm 20^{+17}_{-10}$	1.3 ± 0.3
HERWIG				281	925	3.3
LEPTO	0.3	0.05	1.0	93	239	2.6
ARIADNE	0.3	0.05	1.0	107	283	2.6
LEPTO	0.2	0.05	1.0	54	192	3.6
ARIADNE	0.2	0.05	1.0	61	225	3.7
ARIADNE	0.2	0.025	1.0	71	169	2.4
ARIADNE	0.2	0.05	0.5	67	153	2.3
ARIADNE	0.2	0.025	0.5	76	113	1.5

Table 7.1: Total cross sections, $\sigma(e^+p \to e^+\Xi^- X)$ and $\sigma(e^+p \to e^+\Sigma\,(1385)\,X)$, of Ξ^- and $\Sigma(1385)$, respectively, in a restricted kinematic region of $20 < Q^2 < 200$ GeV^2, $3 \cdot 10^{-4} < x < 2 \cdot 10^{-2}$, $0.04 < y < 0.7$, $1.0 < p_T(\Xi^-, \Sigma\,(1385)) < 5.0$ GeV and $|\eta(\Xi^-, \Sigma\,(1385))| < 1.5$ and the ratio of the cross sections $R = \sigma(e^+p \to e^+\Sigma\,(1385)\,X)/\sigma(e^+p \to e^+\Xi^- X)$. The cross sections measured with the ZEUS detector and predicted by HERWIG, LEPTO and ARIADNE are shown. Since the MCs with default parameters do not agree well with the measured cross sections, the predictions of LEPTO and ARIADNE with changed JETSET parameters γ_s, γ_{spin1} and $\gamma_{SU(6)}$ (see text) concerning the Lund fragmentation model were compared with data, too. The default values are $\gamma_s = 0.3$, $\gamma_{spin1} = 0.05$ and $\gamma_{SU(6)} = 1.0$.

In measurements of K^0, ϕ and Λ at HERA [19, 20, 42, 43, 14] it was found that a suppression factor decreased to $\gamma_s = 0.2$ describes the data better than the standard value of $\gamma_s = 0.3$. Indeed a smaller value of the strangeness suppression factor, $\gamma_s = 0.2$, leads to predicted Ξ^- and $\Sigma(1385)$ cross sections which are lower wrt. the default value of $\gamma_s = 0.3$. However, the prediction of $\Sigma(1385)$ baryon production is still too high, while the forecasted cross sections of Ξ^- baryon production is lower than the measurement. The prediction of the ratio R departs even more from the measurement of the ratio and has a value of $R \approx 3.6$. It looks like that a change of the strangeness suppression factor is not sufficient to describe both Ξ^- and $\Sigma(1385)$ cross sections simultaneously and increases the difference between the measurement and prediction of the ratio R.

For further studies the MC model ARIADNE with strangeness suppression factor $\gamma_s = 0.2$ is chosen, because ARIADNE provides the best description of the hadronic final state observed in inclusive DIS [41] and $\gamma_s \approx 0.2$ shows a better agreement with the measurements of K^0, Λ and $\phi(1020)$ at HERA [19, 20, 42, 43, 14].

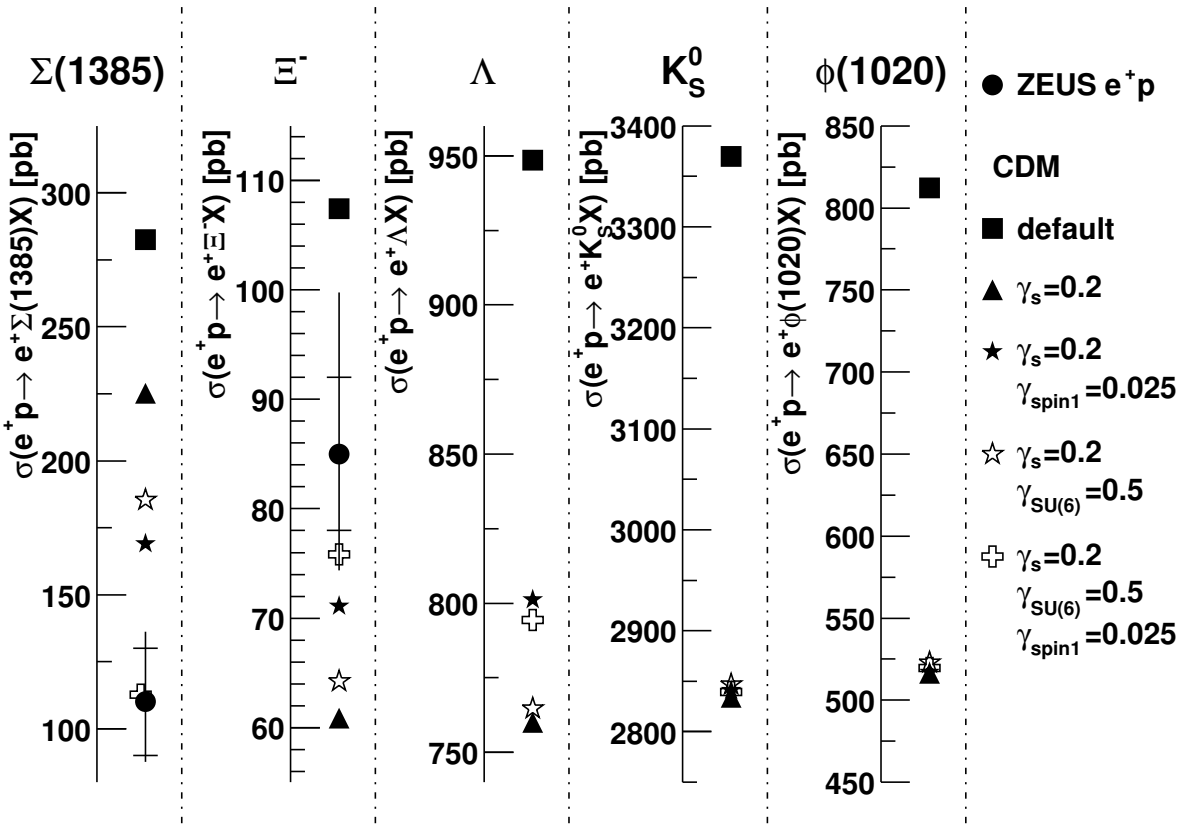

Figure 7.1: Total cross sections of $\Sigma(1385)$, Ξ^-, Λ, K^0_S and $\phi(1020)$ in the same restricted kinematic region of $20 < Q^2 < 200$ GeV^2, $3 \cdot 10^{-4} < x < 2 \cdot 10^{-2}$, $0.04 < y < 0.7$, $1.0 < p_T(\Xi^-, \Sigma\,(1385)) < 5.0$ GeV and $|\eta(\Xi^-, \Sigma\,(1385))| < 1.5$. The measured Ξ^- and $\Sigma(1385)$ cross sections are compared to predictions of ARIADNE with different JETSET parameters γ_s, γ_{spin1} and $\gamma_{SU(6)}$ (see text) concerning the Lund fragmentation model. Also the predicted cross sections of Λ, K^0_S and $\phi(1020)$ in the same restricted kinematic region are shown for the same JETSET parameter settings. The default values are $\gamma_s = 0.3$, $\gamma_{spin1} = 0.05$ and $\gamma_{SU(6)} = 1.0$.

The fragmentation model used in ARIADNE is the Lund string scheme which is implemented in JETSET [36]. JETSET offers several parameters which can be tuned, but it does not make sense to change all of them since they work well for other experiments. Beside the strangeness, one other obvious difference between Ξ^- and $\Sigma(1385)$ baryons is the spin: 3/2 for $\Sigma(1385)$ and 1/2 for Ξ^-. Parameters which take care of the spin of baryons produced during fragmentation are e.g. $PARJ(4)$ and $PARJ(18)$. The former parameter is the suppression of spin 1 diquarks compared with spin 0 ones and is set to $PARJ(4) = 0.05$ by default [36]. From here on the parameter $PARJ(4)$ is labelled as $\gamma_{spin1} \equiv PARJ(4)$. Since the measured cross section is lower than the predicted for $\Sigma(1385)$ and higher for Ξ^- baryon production, this parameter is lowered to improve the agreement. The arbitrary chosen value of γ_{spin1} is $\gamma_{spin1} = 0.025$. This value of γ_{spin1} decreases the cross section of $\Sigma(1385)$ and increases the cross section of Ξ^- baryon production (Tab. 7.1) wrt. the default value of $\gamma_{spin1} = 0.05$, but even a suppression which is half of the default value, does not predict a correct Ξ^- and $\Sigma(1385)$ cross section. The cross sections separated for baryons and anti-baryons show that still an equal number of baryons and anti-baryons is simulated as it is measured (Tab. 7.2). The ratio of the cross sections, R, decreases for the prediction and comes closer to the measurement of R, but is still too high.

The parameter $PARJ(18)$ is an extra suppression factor multiplying the ordinary SU(6) weight for spin 3/2 baryons, and hence a means to break SU(6) in addition to the dynamic breaking implied by γ_s and γ_{spin1} [36]. From here on $PARJ(18)$ is substituted by $\gamma_{SU(6)} \equiv PARJ(18)$. By default no extra suppression is set ($\gamma_{SU(6)} = 1.0$), but to investigate the effect of this parameter on the cross sections, it is varied to $\gamma_{SU(6)} = 0.5$. A lower value of $\gamma_{SU(6)}$ has the same effect as a lower value of γ_{spin1}, it decreases the cross section which is predicted for $\Sigma(1385)$ and increases the Ξ^- baryon production (Tab. 7.1) wrt. the default values. The forecasted cross section for Ξ^- baryons is lower than the measurement but too high for $\Sigma(1385)$ baryon production. Also the forecasted ratio of the two cross sections, R, is still too high.

If both parameters are halved to the values $\gamma_{spin1} = 0.025$ and $\gamma_{SU(6)} = 0.5$ at the same time, the predicted cross sections of Ξ^- and $\Sigma(1385)$ are close to the centre values of the measurement and agree with the MC within the errors (Tab. 7.1). In consequence the ratio of the cross sections in the MC is $R = 1.5$ and in agreement with the measurement of $R = 1.3 \pm 0.3$. The predicted ratios of baryon to anti-baryon cross sections are not affected by both parameters, an equal number of baryons and anti-baryons is predicted for $\gamma_{spin1} = 0.025$ and $\gamma_{SU(6)} = 0.5$ at each case and simultaneously (Tab. 7.2).

Tuning the parameters γ_{spin1} and $\gamma_{SU(6)}$ to improve the agreement with the measured Ξ^- and $\Sigma(1385)$ cross sections might destroy existing agreement for other particles. Therefore the changes of the Λ, K^0_S and $\phi(1020)$ cross sections in the same kinematic region predicted with different parameters of γ_s, γ_{spin1} and $\gamma_{SU(6)}$ are investigated (Fig. 7.1). For Λ, K^0_S and ϕ it is known that $\gamma_s = 0.3$ predicts a rate too high to accommodate the measured data. A value of $\gamma_s \approx 0.2$ agrees better with the measurements [19, 20, 42, 43, 14], although

this parameter might be a little bit too low[1]. Changes of the parameters γ_{spin1} and $\gamma_{SU(6)}$ do not have any influence on the K^0_S and $\phi(1020)$ meson cross section which is forecasted (Fig. 7.1), so the found agreement between the measurement of the ϕ cross section and the Monte Carlo simulation with $\gamma_s = 0.22$ [14] cannot be destroyed by this tuning. The case is different for the prediction of the Λ baryon cross sections. Reducing the parameter γ_{spin1} increases the Λ cross section by nearly 5%, which is $\approx 20\%$ of the difference between the cross sections with $\gamma_s = 0.3$ and $\gamma_s = 0.2$. The parameter $\gamma_{SU(6)}$ has nearly no effect on the cross section. Changing both parameters at the same time, a cross section similar to the one with changed γ_{spin1} alone is forecasted.

The comparison of Monte Carlo cross sections with and without tuned γ_{spin1} and $\gamma_{SU(6)}$ parameter indicates that for ϕ, Λ and K^0_S all presented changes are in agreement with previous measurements of these particles at HERA (see chapter 1).

The default ARIADNE MC with the parameters γ_s, $\gamma_{SU(6)}$ and γ_{spin1} changed to $\gamma_s = 0.2$, $\gamma_{SU(6)} = 0.5$ and $\gamma_{spin1} = 0.025$ is able to describe the cross sections of Ξ^- and $\Sigma(1385)$ and is in agreement with measurements of K^0, Λ and $\phi(1020)$ at HERA [19, 20, 42, 43, 14].

The MC models predict that the production of Ξ^- baryons and $\overline{\Xi}^+$ anti-baryons have an equal cross section. The measurement of the ratio, $N_{\Xi^-}/N_{\Xi_{all}}$ ($N_{\overline{\Xi}^+}/N_{\Xi_{all}}$), of the number, N_{Ξ^-} ($N_{\overline{\Xi}^+}$), of Ξ^- ($\overline{\Xi}^+$) baryons to the number N_{all} of all produced Ξ^- and $\overline{\Xi}^+$ baryons shows an equal production of baryons and anti-baryons within the uncertainty, which is in agreement with the MC (Tab. 7.2). The tuning presented above does not destroy the prediction of an equal production of Ξ^- baryons and $\overline{\Xi}^+$ anti-baryons.

The measurement of the ratios $N_{\Sigma(1385)^+}/N_{\Sigma(1385)}$, $N_{\overline{\Sigma}(1385)^-}/N_{\Sigma(1385)}$, $N_{\Sigma(1385)^-}/N_{\Sigma(1385)}$ and $N_{\overline{\Sigma}(1385)^+}/N_{\Sigma(1385)}$ is compared to the presented MC models with different tunings. The measurements are in agreement with the MC predictions within the uncertainty (Tab. 7.2). The MC models forecast an equal production of the baryon anti-baryon pair $\Sigma(1385)^+$ and $\overline{\Sigma}(1385)^-$ as well as for the pair $\Sigma(1385)^-$ and $\overline{\Sigma}(1385)^+$, which remains independent of the presented tuning. However, the tuning changes the ratio of $N_{\Sigma(1385)^+ + \overline{\Sigma}(1385)^-}/N_{\Sigma(1385)^- + \overline{\Sigma}(1385)^+}$ slightly in the MC, but the uncertainty of the measurement does not allow to exclude any of the predictions.

The measurement is in agreement with all MC predictions which forecast an equal cross section for all baryon anti-baryon pairs.

[1] DELPHI prefers a value of $\gamma_s = 0.23$ (see chapter 1), the ϕ measurement at HERA [14] shows the best agreement with a value of $\gamma_s = 0.22$ and a few K^0 and Λ measurements show that a value of $\gamma_s = 0.2$ might be too low (see chapter 1).

	γ_s	γ_{spin1}	$\gamma_{SU(6)}$	$N_{\Xi^-}/N_{\Xi_{all}}$	$N_{\overline{\Xi}^+}/N_{\Xi_{all}}$
ZEUS				0.50 ± 0.05	0.50 ± 0.05
HERWIG				0.50	0.50
LEPTO	0.3	0.05	1.0	0.50	0.50
ARIADNE	0.3	0.05	1.0	0.50	0.50
LEPTO	0.2	0.05	1.0	0.50	0.50
ARIADNE	0.2	0.05	1.0	0.50	0.50
ARIADNE	0.2	0.025	1.0	0.50	0.50
ARIADNE	0.2	0.05	0.5	0.50	0.50
ARIADNE	0.2	0.025	0.5	0.50	0.50

	γ_s	γ_{spin1}	$\gamma_{SU(6)}$	$N_{\Sigma(1385)^+}/N_{\Sigma(1385)}$	$N_{\overline{\Sigma}(1385)^-}/N_{\Sigma(1385)}$
ZEUS				$0.34 \pm 0.06^{+0.01}_{-0.01}$	$0.21 \pm 0.07^{+0.01}_{-0.01}$
HERWIG				0.27	0.27
LEPTO	0.3	0.05	1.0	0.28	0.28
ARIADNE	0.3	0.05	1.0	0.28	0.28
LEPTO	0.2	0.05	1.0	0.29	0.29
ARIADNE	0.2	0.05	1.0	0.28	0.28
ARIADNE	0.2	0.025	1.0	0.29	0.29
ARIADNE	0.2	0.05	0.5	0.29	0.29
ARIADNE	0.2	0.025	0.5	0.30	0.30

	γ_s	γ_{spin1}	$\gamma_{SU(6)}$	$N_{\Sigma(1385)^-}/N_{\Sigma(1385)}$	$N_{\overline{\Sigma}(1385)^+}/N_{\Sigma(1385)}$
ZEUS				$0.12 \pm 0.10^{+0.01}_{-0.01}$	$0.31 \pm 0.08^{+0.03}_{-0.01}$
HERWIG				0.23	0.23
LEPTO	0.3	0.05	1.0	0.22	0.22
ARIADNE	0.3	0.05	1.0	0.22	0.22
LEPTO	0.2	0.05	1.0	0.21	0.21
ARIADNE	0.2	0.05	1.0	0.22	0.22
ARIADNE	0.2	0.025	1.0	0.21	0.21
ARIADNE	0.2	0.05	0.5	0.21	0.21
ARIADNE	0.2	0.025	0.5	0.20	0.20

Table 7.2: Ratios, $N_{\Xi^-}/N_{\Xi_{all}}$, $N_{\overline{\Xi}^+}/N_{\Xi_{all}}$, $N_{\Sigma(1385)^+}/N_{\Sigma(1385)}$, $N_{\overline{\Sigma}(1385)^-}/N_{\Sigma(1385)}$, $N_{\Sigma(1385)^-}/N_{\Sigma(1385)}$ and $N_{\overline{\Sigma}(1385)^+}/N_{\Sigma(1385)}$, of the reconstructed number, N, of Ξ^-, $\overline{\Xi}^+$, $\Sigma(1385)^+$, $\overline{\Sigma}(1385)^-$, $\Sigma(1385)^-$ and $\overline{\Sigma}(1385)^+$ respectively, to the total number of reconstructed Ξ^- and $\Sigma(1385)$ baryons, $N_{\Xi_{all}}$ and $N_{\Sigma(1385)}$ respectively, in a restricted kinematic region of $20 < Q^2 < 200$ GeV^2, $3 \cdot 10^{-4} < x < 2 \cdot 10^{-2}$, $0.04 < y < 0.7$, $1.0 < p_T(\Xi^-, \Sigma\,(1385)) < 5.0$ GeV and $|\eta(\Xi^-, \Sigma\,(1385))| < 1.5$. The ratios measured with the ZEUS detector and predicted by HERWIG, LEPTO and ARIADNE are shown. Since the MCs with default parameters do not agree well with the measured cross sections, the predictions of LEPTO and ARIADNE with changed JETSET parameters γ_s, γ_{spin1} and $\gamma_{SU(6)}$ (see text) concerning the Lund fragmentation model are stated, too. The default values are $\gamma_s = 0.3$, $\gamma_{spin1} = 0.05$ and $\gamma_{SU(6)} = 1.0$.

7.2 Inclusive Ξ^- and $\Sigma(1385)$ baryon cross sections in bins of Q^2, x, p_T and η

The identification of Ξ^- with reconstructed displaced tertiary vertices allows the measurement of cross sections with a smaller uncertainty than with the other approach. Thus, all differential cross sections are measured with the more certain method. The mass distributions in bins of Q^2, x, $p_T(\Xi^-)$ and $\eta(\Xi^-)$ (Fig. A.1, A.2, A.3 and A.4) are evaluated with the method described in chapter 5.2.

The inclusive $\Sigma(1385)$ cross sections in bins of Q^2, x, $p_T(\Sigma\,(1385))$ and $\eta(\Sigma\,(1385))$ are calculated from the corresponding mass distributions (Fig. A.5, A.6, A.7 and A.8) reconstructed with the *pvt* approach, which is described in chapter 5.3.

The systematic uncertainties cannot be estimated for each bin separately, because already for the total cross sections statistical fluctuations cover the real systematic uncertainty. With fewer statistics, after dividing the experimental data in bins of Q^2, x, p_T and η, no reliable estimate is possible. Therefore the quoted systematic uncertainties are taken from the total cross sections.

The measured differential cross sections as functions of p_T, η, x and Q^2 are compared to the same MC generators and sets of parameters already introduced in the chapter before: LEPTO, ARIADNE and HERWIG. Although not all MCs are able to predict a total cross section in agreement with the data, the shapes of the differential cross sections could be. Therefore the MC distributions are always scaled to the area below the data.

7.2.1 Inclusive Ξ^- baryon cross sections in bins of Q^2, x, $p_T(\Xi^-)$ and $\eta(\Xi^-)$

The differential Ξ^- baryons cross sections measured as a function of $p_T(\Xi^-)$, $\eta(\Xi^-)$, x and Q^2 are shown in Fig. 7.2 and listed in Tab. 7.3.

The shape of the differential cross sections as a function of $p_T(\Xi^-)$, $\eta(\Xi^-)$, x and Q^2 are predicted by LEPTO and ARIADNE with a strangeness suppression factor of $\gamma_s = 0.2$ and HERWIG. They all are in agreement with the data within large uncertainties (Fig. 7.2).

The shapes of the investigated differential cross sections of Ξ^- baryons generated with ARIADNE, suppression factor $\gamma_s = 0.2$ and changed parameters γ_{spin1} and $\gamma_{SU(6)}$ do not differ from the distribution with default values of γ_{spin1} and $\gamma_{SU(6)}$. Thus these distributions are not shown.

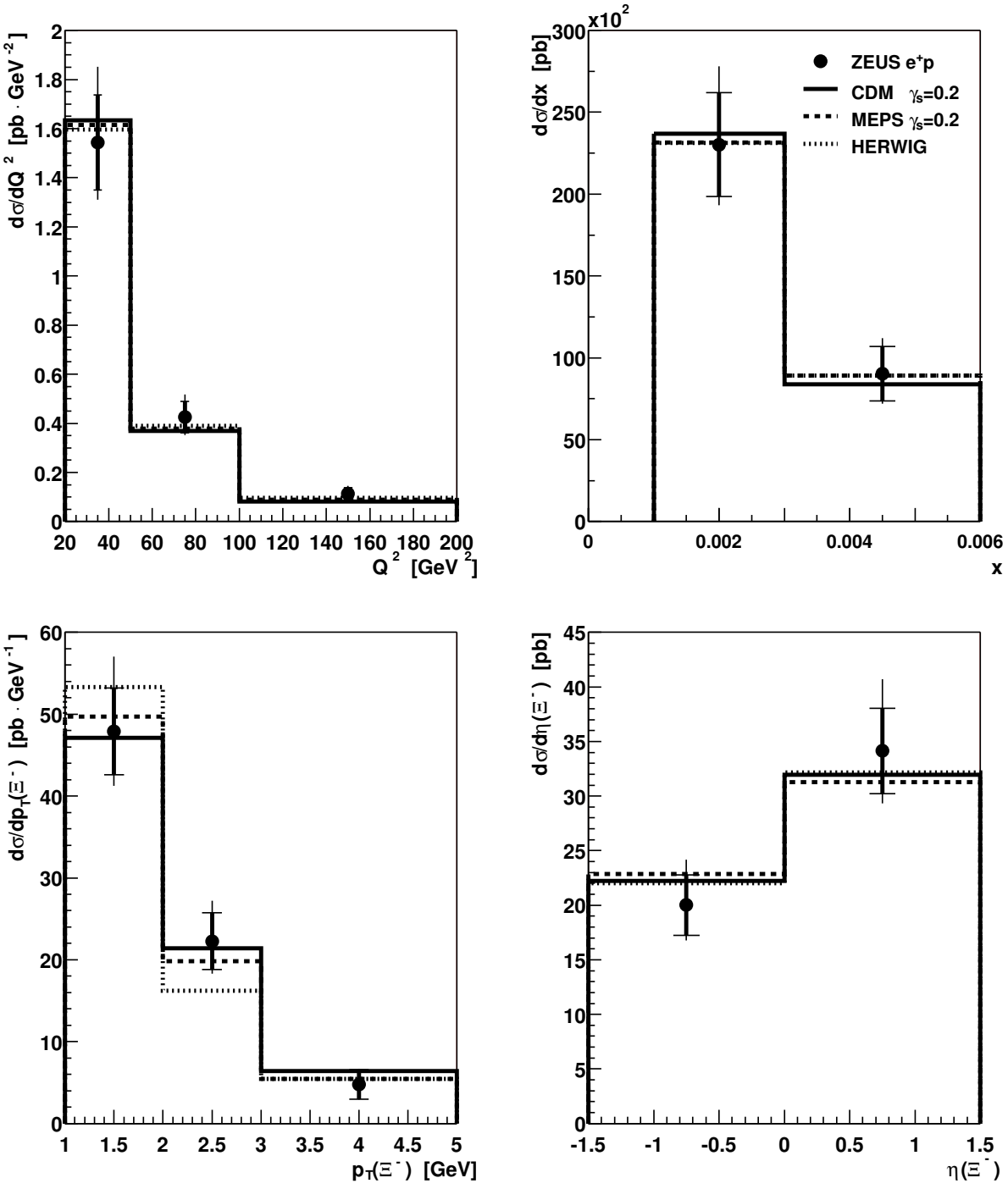

Figure 7.2: Differential Ξ^- baryon cross sections as a function of Q^2, x, $p_T(\Xi^-)$ and $\eta(\Xi^-)$. Differential cross sections which are measured (points) are compared to leading-order MC models with the CTEQ5D parton density function. LEPTO (MEPS) and ARIADNE (CDM) are shown for a strangeness suppression factor of $\gamma_s = 0.2$. All MC distributions are scaled to the area below the data to compare the shapes of the distributions. The inner error bars represent the statistical, the outer error bar the systematic uncertainties.

range (GeV)	$< p_T(\Xi^-) >$ (GeV)	N_{Ξ^-}	$d\sigma/dp_T(\Xi^-)$ (pb/GeV)
1.0 – 2.0	1.49	116 ± 12	$48 \pm 5^{+7}_{-4}$
2.0 – 3.0	2.38	57 ± 8	$22 \pm 3^{+3}_{-2}$
3.0 – 5.0	3.52	11 ± 4	$5 \pm 2^{+0.8}_{-0.4}$

range	$< \eta(\Xi^-) >$	N_{Ξ^-}	$d\sigma/d\eta(\Xi^-)$ (pb)
-1.5 – 0.0	-0.58	75 ± 10	$20 \pm 3^{+3}_{-2}$
0.0 – 1.5	0.66	108 ± 12	$34 \pm 4^{+5}_{-3}$

range	$< x >$	N_{Ξ^-}	$d\sigma/dx$ ($10^3 \cdot$ pb)
0.001 – 0.003	0.00185	75 ± 10	$19 \pm 4^{+3}_{-2}$
0.003 – 0.006	0.00421	42 ± 7	$11 \pm 2^{+2}_{-1}$

range (GeV^2)	$< Q^2 >$ (GeV^2)	N_{Ξ^-}	$d\sigma/dQ^2$ (pb/GeV^2)
20 – 50	33	89 ± 11	$1.5 \pm 0.2^{+0.2}_{-0.1}$
50 – 100	68	62 ± 9	$0.43 \pm 0.06^{+0.07}_{-0.04}$
100 – 200	136	32 ± 6	$0.11 \pm 0.02^{+0.02}_{-0.01}$

Table 7.3: Differential Ξ^- baryon cross sections, $d\sigma$, measured as a function of $p_T(\Xi^-)$, $\eta(\Xi^-)$, x and Q^2. The first error is the statistical and the second asymmetric errors are the systematic uncertainties. The number of Ξ^- baryons, N_{Ξ^-}, and the mean value of the experimental data in the mass window below the signal, $1.30 < m(\Lambda\pi) < 1.34$ GeV, are listed for each range of $p_T(\Xi^-)$, $\eta(\Xi^-)$, x and Q^2.

7.2.2 Inclusive $\Sigma(1385)$ baryon cross sections in bins of Q^2, x, $p_T(\Sigma\,(1385))$ and $\eta(\Sigma\,(1385))$

The differential $\Sigma(1385)$ baryon cross sections measured as a function of $p_T(\Sigma\,(1385))$, $\eta(\Sigma\,(1385))$, x and Q^2 are shown in Fig. 7.3 and listed in Tab. 7.4.

The shapes of the differential cross sections as a function of $p_T(\Sigma\,(1385))$, $\eta(\Sigma\,(1385))$, x and Q^2 are predicted by LEPTO and ARIADNE with a strangeness suppression factor of $\gamma_s = 0.2$ and HERWIG. They all are in agreement with the data within large uncertainties (Fig. 7.3).

The shapes of the investigated differential cross sections of $\Sigma(1385)$ generated with ARIADNE, suppression factor $\gamma_s = 0.2$ and changed parameters γ_{spin1} and $\gamma_{SU(6)}$ do not differ from the distribution with default values of γ_{spin1} and $\gamma_{SU(6)}$. Thus these distributions are not shown.

range (GeV)	$< p_T(\Sigma\,(1385)) >$ (GeV)	$N_{\Sigma(1385)}$	$d\sigma/dp_T(\Sigma\,(1385))$ (pb/GeV)
1.0 – 2.0	1.45	288 ± 78	$60 \pm 16^{+9}_{-5}$
2.0 – 3.0	2.40	189 ± 47	$35 \pm 9^{+5}_{-3}$
3.0 – 5.0	3.51	65 ± 26	$10 \pm 4^{+2}_{-1}$
range	$< \eta(\Sigma\,(1385)) >$	$N_{\Sigma(1385)}$	$d\sigma/d\eta(\Sigma\,(1385))$ (pb)
-1.5 – 0.0	-0.56	168 ± 58	$22 \pm 8^{+3}_{-2}$
0.0 – 1.5	0.69	374 ± 75	$55 \pm 11^{+9}_{-5}$
range	$< x >$	$N_{\Sigma(1385)}$	$d\sigma/dx$ ($10^3 \cdot$ pb)
0.001 – 0.002	0.00145	188 ± 53	$40 \pm 11^{+6}_{-3}$
0.002 – 0.0035	0.00267	145 ± 46	$19 \pm 6^{+3}_{-2}$
0.0035 – 0.008	0.00511	88 ± 41	$3 \pm 1^{+0.5}_{-0.3}$
range (GeV^2)	$< Q^2 >$ (GeV^2)	$N_{\Sigma(1385)}$	$d\sigma/dQ^2$ (pb/GeV^2)
20 – 50	33	252 ± 68	$2.2 \pm 0.6^{+0.3}_{-0.2}$
50 – 100	69	221 ± 55	$0.7 \pm 0.2^{+0.1}_{-0.1}$
100 – 200	138	66 ± 38	$0.09 \pm 0.05^{+0.01}_{-0.01}$

Table 7.4: Differential $\Sigma(1385)$ baryon cross sections as functions of $p_T(\Sigma\,(1385))$, $\eta(\Sigma\,(1385))$, x and Q^2. The first error is the statistical and the second asymmetric errors are the systematic uncertainties. The number of $\Sigma(1385)$ baryons, $N_{\Sigma(1385)}$, and the mean value of the experimental data in the mass window below the signals, $1.35 < m(\Lambda\pi) < 1.45$ GeV, are listed for each range of $p_T(\Sigma\,(1385))$, $\eta(\Sigma\,(1385))$, x and Q^2.

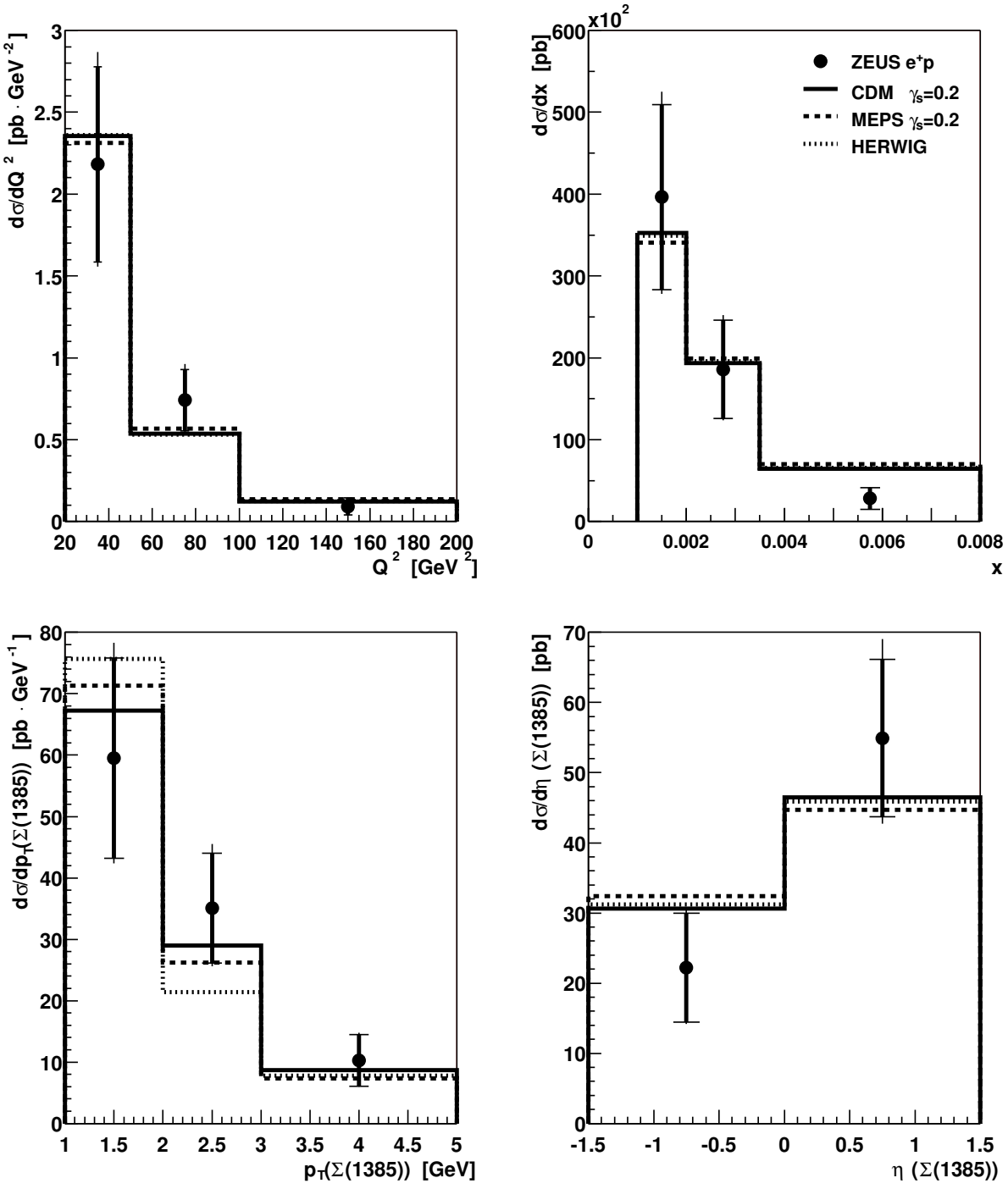

Figure 7.3: Differential $\Sigma(1385)$ baryon cross sections as a function of Q^2, x, $p_T(\Sigma\,(1385))$ and $\eta(\Sigma\,(1385))$. Differential cross sections which are measured (points) are compared to leading-order MC models with the CTEQ5D parton density function. LEPTO (MEPS) and ARIADNE (CDM) are shown for a strangeness suppression factor of $\gamma_s = 0.2$. All MC distributions are scaled to the area below the data to compare the shapes of the distributions. The inner error bars represent the statistical, the outer error bar the systematic uncertainties.

7.3 Total Ξ^- and $\Sigma(1385)$ baryon cross section in a range of virtuality of the exchanged photon of $20 < Q^2 < 200$ GeV^2

The total Ξ^- and $\Sigma(1385)$ cross section, σ_{Ξ^-}(cuts) and $\sigma_{\Sigma(1385)}$(cuts) respectively, which are measured in a restricted kinematic region of $20 < Q^2 < 200$ GeV^2, $3 \cdot 10^{-4} < x < 2 \cdot 10^{-2}$, $0.04 < y < 0.7$, $1.0 < p_T(\Xi^-, \Sigma\,(1385)) < 5.0$ GeV and $|\eta(\Xi^-, \Sigma\,(1385))| < 1.5$, can be extrapolated to a total Ξ^- and $\Sigma(1385)$ cross section, $\sigma_{\Xi^-}(20 < Q^2 < 200$ GeV$^2)$ and $\sigma_{\Sigma(1385)}(20 < Q^2 < 200$ GeV$^2)$ respectively, in a range of virtuality of the exchanged boson of $20 < Q^2 < 200$ GeV^2 using the ARIADNE and HERWIG MC (Tab. 7.5). Since the differential distributions of the MC models are in agreement with the measurement, this extrapolation may be justified. The ratios, $\sigma(20 < Q^2 < 200$ GeV$^2)/\sigma$(cuts), for Ξ^- and $\Sigma(1385)$ baryons strongly depend on the MC model which is used. The biggest discrepancy exist for the extrapolation of the Ξ^- baryon cross section, where the simulations differ by a factor of 2.

$\frac{\sigma(20<Q^2<200\ \text{GeV}^2)}{\sigma(\text{cuts})}$	ARIADNE	HERWIG
Ξ^-	8.0 ± 0.2	16.2 ± 0.2
$\Sigma(1385)$	13.3 ± 0.2	15.8 ± 0.2
$\Sigma(1385)^-$	10.7 ± 0.2	16.1 ± 0.2
$\Sigma(1385)^+$	15.0 ± 0.2	15.6 ± 0.2

Table 7.5: Ratios, $\sigma(20 < Q^2 < 200$ GeV$^2)/\sigma$(cuts), of the cross section, $\sigma(20 < Q^2 < 200$ GeV$^2)$, in a range of virtuality of the exchanged boson of $20 < Q^2 < 200$ GeV^2 to the cross section, σ(cuts), simulated in a restricted kinematic region of $20 < Q^2 < 200$ GeV^2, $3 \cdot 10^{-4} < x < 2 \cdot 10^{-2}$, $0.04 < y < 0.7$, $1.0 < p_T(\Xi^-, \Sigma\,(1385)) < 5.0$ GeV and $|\eta(\Xi^-, \Sigma\,(1385))| < 1.5$, computed for ARIADNE and HERWIG. The ratios are calculated for the cross sections of Ξ^- baryons, where Ξ^- includes Ξ^- and $\overline{\Xi}^+$, of $\Sigma(1385)$ baryons, where $\Sigma(1385)$ includes $\Sigma(1385)^+$, $\overline{\Sigma}(1385)^-$, $\Sigma(1385)^-$ and $\overline{\Sigma}(1385)^+$, of $\Sigma(1385)^-$ baryons, where $\Sigma(1385)^-$ includes $\Sigma(1385)^-$ and $\overline{\Sigma}(1385)^+$, and of $\Sigma(1385)^+$ baryons, where $\Sigma(1385)^+$ includes $\Sigma(1385)^+$ and $\overline{\Sigma}(1385)^-$.

Chapter 8

Summary and conclusions

Inclusive Ξ^- and $\Sigma(1385)$ baryon cross sections in a restricted kinematic region have been measured in deep inelastic scattering for $20 < Q^2 < 200$ GeV^2, $3 \cdot 10^{-4} < x < 2 \cdot 10^{-2}$, $0.04 < y < 0.7$, $1.0 < p_T(\Xi^-, \Sigma\,(1385)) < 5.0$ GeV and $|\eta(\Xi^-, \Sigma\,(1385))| < 1.5$ with the ZEUS detector at HERA for the first time.

The measured cross sections of Ξ^- and $\Sigma(1385)$ baryons are overestimated by the default ARIADNE and LEPTO Monte Carlo generators which are based on the Lund string fragmentation model with a strangeness suppression factor of $\gamma_s = 0.3$. HERWIG overestimates the total Ξ^- and $\Sigma(1385)$ cross section even more than ARIADNE and LEPTO. Also the simulated ratio of the cross sections, $R = \sigma(e^+p \rightarrow e^+\Sigma\,(1385)\,X)/\sigma(e^+p \rightarrow e^+\Xi^-X)$, is not in agreement with the measurement but about twice as high. However, the MCs predict an equal cross section for baryons and anti-baryons, which is in agreement with the measurement within the uncertainties.

A reduced strangeness suppression factor, $\gamma_s = 0.2$, is suggested by other measurements of the production of K^0, Λ and $\phi(1020)$ at HERA [19, 20, 42, 43, 14]. This reduced parameter reduces the predicted total Ξ^- and $\Sigma(1385)$ baryon cross section. Nevertheless the $\Sigma(1385)$ baryon cross section is still too high while the Ξ^- cross section is lower than the measured one. Also the simulated ratio, R, shows a discrepancy which is even higher than with $\gamma_s = 0.3$. The main differences between Ξ^- and $\Sigma(1385)$ are the spin and strangeness: spin 3/2 and one strange quark for $\Sigma(1385)$ and spin 1/2 and two strange quarks for Ξ^-. Since a change of the strangeness suppression parameter does not solve the disagreement, the effect of the two JETSET parameters $\gamma_{spin1} \equiv PARJ(4)$ and $\gamma_{SU(6)} \equiv PARJ(18)$ [36] are investigated, because these set the probability of the production of baryons depending on the spin of the baryon which is produced. The former parameter γ_{spin1} is the suppression of spin 1 diquarks compared with spin 0 ones. This parameter is decreased to $\gamma_{spin1} = 0.025$ from the default value of $\gamma_{spin1} = 0.05$, but measurement and prediction are not in agreement. The parameter $\gamma_{SU(6)}$ is an extra suppression factor multiplying the ordinary SU(6) weight for spin 3/2 baryons, and hence a means to break SU(6) in addition to the dynamic breaking implied by γ_s and γ_{spin1}. The reduction of the parameter $\gamma_{SU(6)}$ from

the default value of $\gamma_{SU(6)} = 1$ to $\gamma_{SU(6)} = 0.5$ shows a similar effect of the predicted cross sections as seen for γ_{spin1} before. Only reducing both γ_{spin1} and $\gamma_{SU(6)}$ to the values of $\gamma_{spin1} = 0.05$ and $\gamma_{SU(6)} = 0.5$ results in a Ξ^- and $\Sigma(1385)$ baryon cross section which are in agreement with the measurement within the errors.

Since other measurements of strange particles (K^0, Λ and $\phi(1020)$) at HERA exist [19, 20, 42, 43, 14] which agree with the MCs with default values of γ_{spin1}=0.05, $\gamma_{SU(6)} = 1$ and reduced value of $\gamma_s = 0.2$, the presented tuning must not destroy this agreement. A change of γ_{spin1} to $\gamma_{spin1} = 0.025$ and $\gamma_{SU(6)}$ to $\gamma_{SU(6)} = 0.5$ leads to predicted K^0_S, Λ and $\phi(1020)$ cross sections, which are in agreement with previous measurements of strange particles at HERA. Since only a combined change of γ_{spin1} and $\gamma_{SU(6)}$ gives the correct $\Sigma(1385)$ cross section, it is suggested that this tuning be used and checked with further strange particle productions at HERA.

The shapes of the differential Ξ^- and $\Sigma(1385)$ baryon cross sections are presented as a function of Q^2, x, η and p_T. They are reasonably reproduced by the Monte Carlos calculations.

Acknowledgments

I thank the DESY directorate for the financial support throughout my time at DESY. Also I am grateful to my adviser E. Lohrmann for his support, the pieces of advice and his experience which helped me to avoid dead ends and gave me a deeper insight into physics. I would like to thank S. Chekanov and M. Sutton, too, who helped me through all the years and answered many questions about the ZEUS software and detector, HERA physics, MC generators, presentations etc. S. Hillert introduced me to orange, explained the use and supported my work. If questions about C and C++ appeared I always found a helping soul in R.P. Feller.

I would like to thank Claire Gwenlan who proof-read my thesis and enlarged my knowledge of English with her comments.

Many thanks go to my loving, helpful, understanding and beautiful wife Arzu who supported me all the time although she had much trouble herself.

Appendix A

Mass distribution $m(\Lambda\pi)$ in bins of Q^2, x, p_T and η

The mass distribution $m(\Lambda\pi)$ in bins of Q^2, x, p_T and η, which are used for the calculation of the differential inclusive cross sections, are shown for both reconstruction approaches: the identification of Ξ^- baryons with reconstructed displaced tertiary vertices (dtv) and $\Sigma(1385)$ baryons with primary vertex fitted tracks (pvt).

A.1 Mass distribution $m(\Lambda\pi)$ with dtv approach in bins of Q^2, x, p_T and η

The mass distributions $m(\Lambda\pi)$ in bins of Q^2 , x, $p_T(\Xi^-)$ and $\eta(\Xi^-)$ are shown in Fig. A.1, Fig. A.2, Fig. A.3 and Fig. A.4, respectively.

A.2 Mass distribution $m(\Lambda\pi)$ with pvt approach in bins of Q^2, x, p_T and η

The mass distributions $m(\Lambda\pi)$ in bins of Q^2 , x, $p_T(\Sigma\,(1385))$ and $\eta(\Sigma\,(1385))$ are shown in Fig. A.5, Fig. A.6, Fig. A.7 and Fig. A.8, respectively.

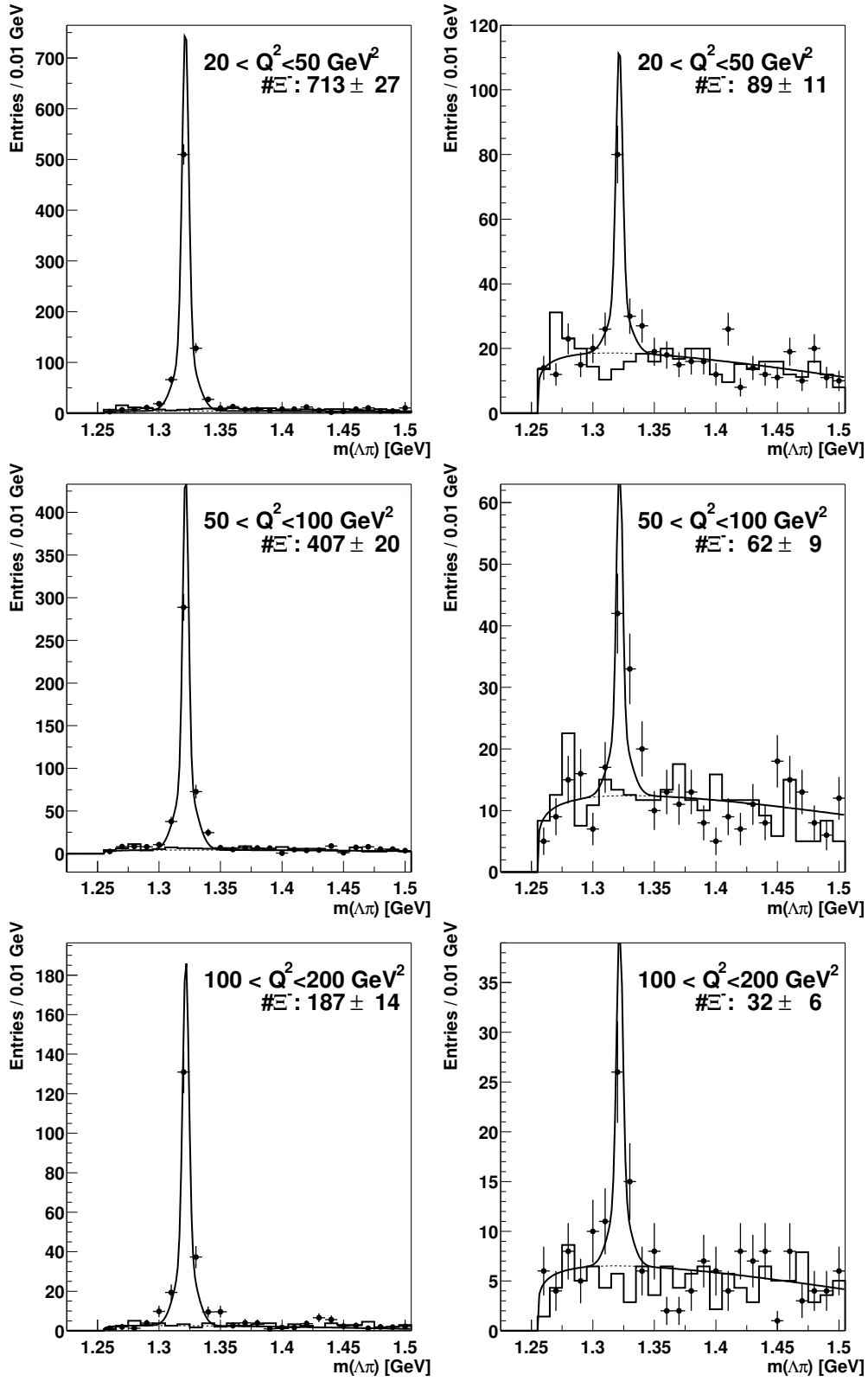

Figure A.1: Mass distribution $m(\Lambda\pi)$ in bins of Q^2 for CDM Ξ–MC (left) and data (right). The full line describes the parameterisation which is found by the fit (Eq. 5.3), the dashed line represents the background parameterisation only. The histogram shows the wrong charge background which is normalised to the area of the signal sample in the range of $1.355 < m(\Lambda\pi) < 1.505$ GeV.

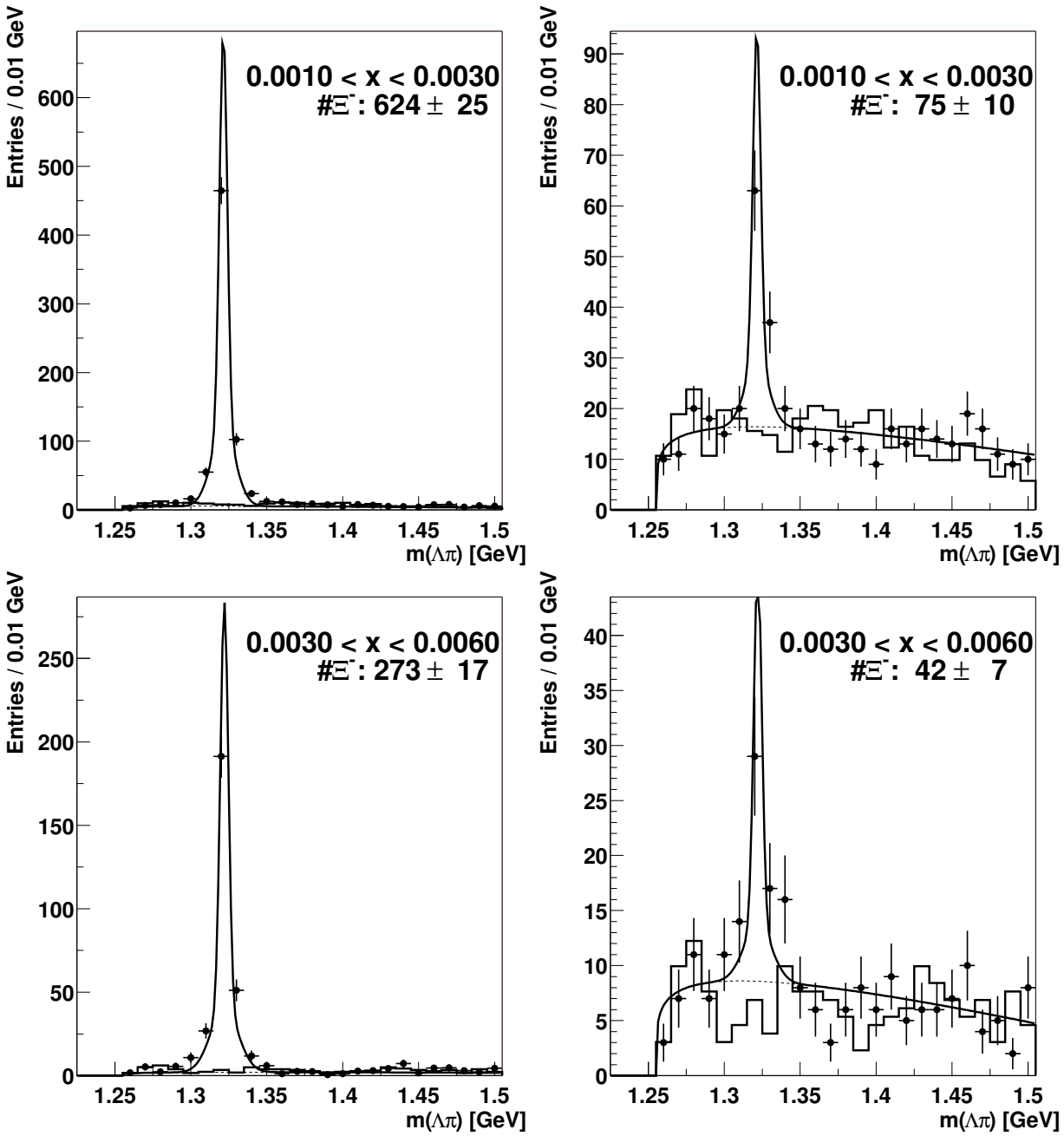

Figure A.2: Mass distribution $m(\Lambda\pi)$ in bins of x for CDM Ξ–MC (left) and data (right). The full line describes the parameterisation which is found by the fit (Eq. 5.3), the dashed line represents the background parameterisation only. The histogram shows the wrong charge background which is normalised to the area of the signal sample in the range of $1.355 < m(\Lambda\pi) < 1.505$ GeV.

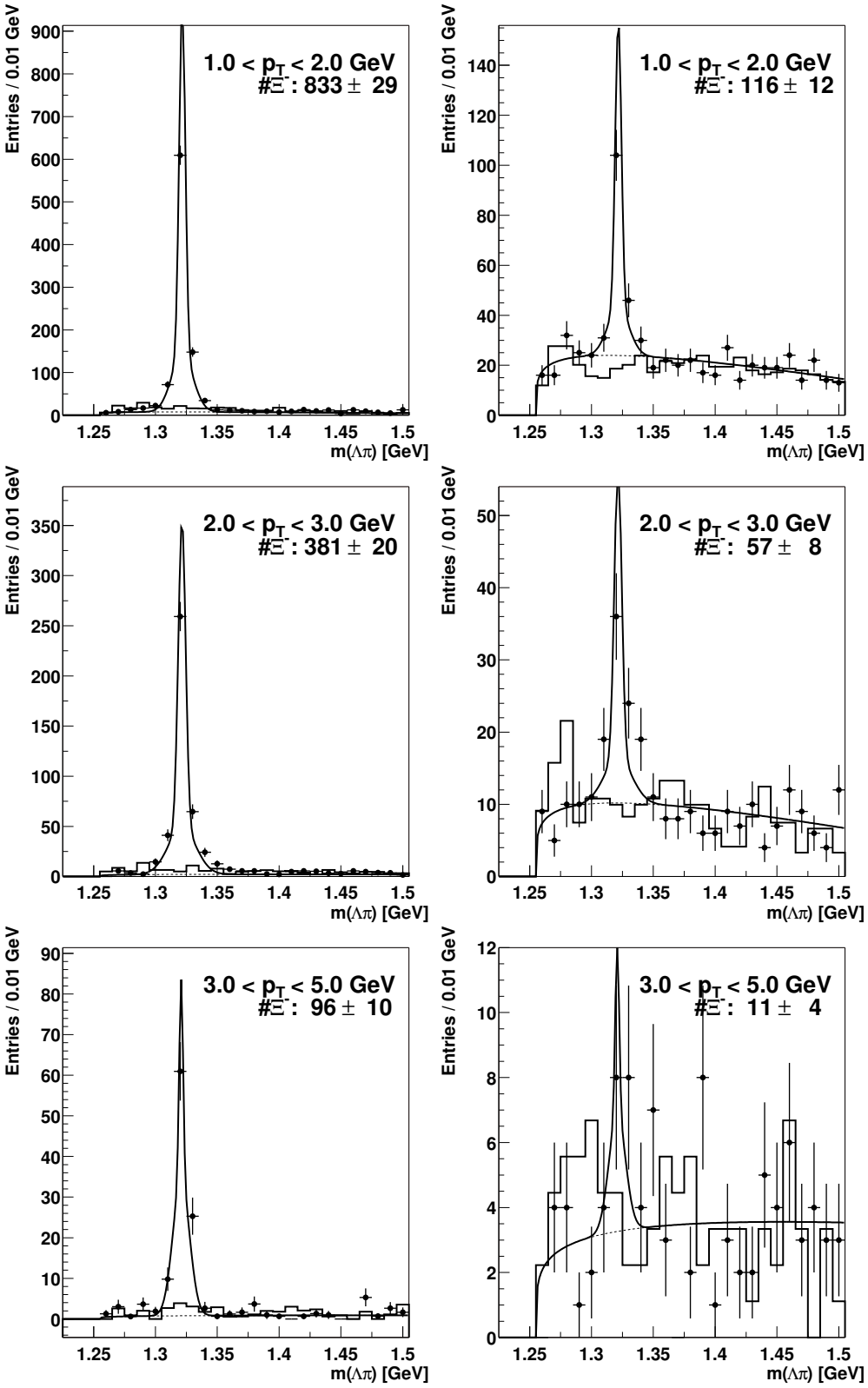

Figure A.3: Mass distribution $m(\Lambda\pi)$ in bins of $p_T(\Xi^-)$ for CDM Ξ–MC (left) and data (right). The full line describes the parameterisation which is found by the fit (Eq. 5.3), the dashed line represents the background parameterisation only. The histogram shows the wrong charge background which is normalised to the area of the signal sample in the range of $1.355 < m(\Lambda\pi) < 1.505$ GeV.

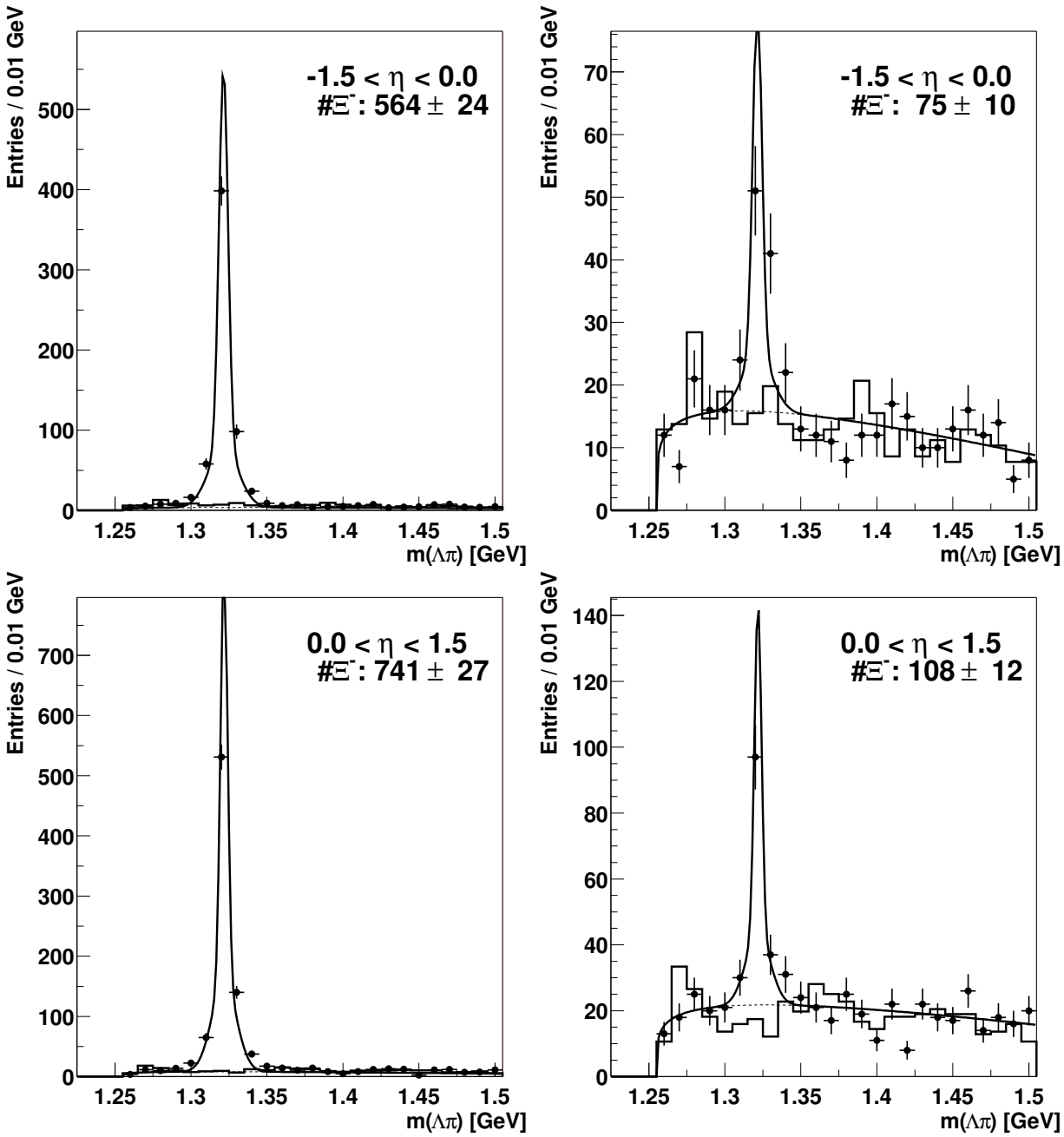

Figure A.4: Mass distribution $m(\Lambda\pi)$ in bins of $\eta(\Xi^-)$ for CDM Ξ–MC (left) data (right). The full line describes the parameterisation which is found by the fit (Eq. 5.3), the dashed line represents the background parameterisation only. The histogram shows the wrong charge background which is normalised to the area of the signal sample in the range of $1.355 < m(\Lambda\pi) < 1.505$ GeV.

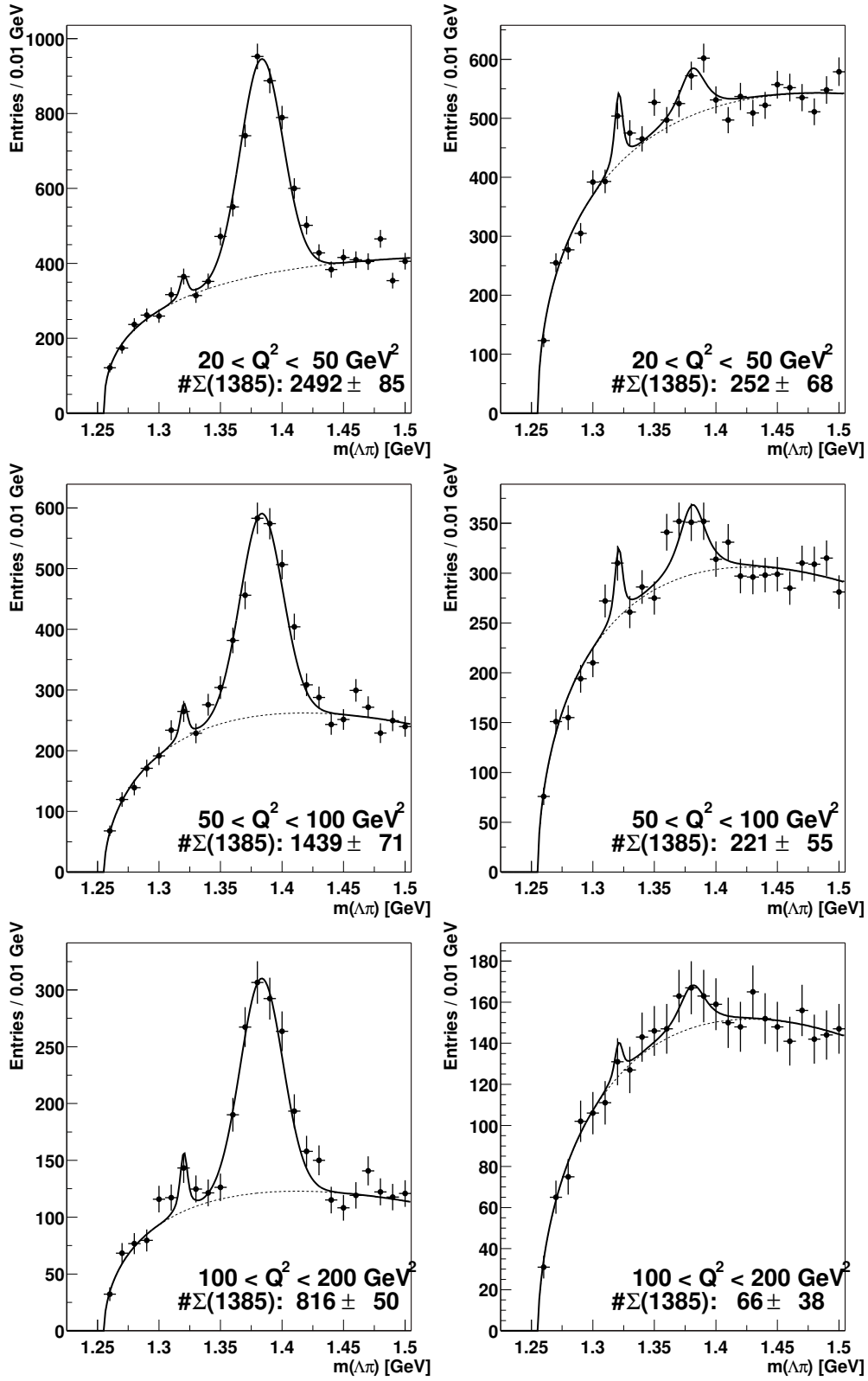

Figure A.5: Mass distribution $m(\Lambda\pi)$ in bins of Q^2 for Σ–MC (left) and data (right). The full line describes the parameterisation which is found by the fit (Eq. 5.4), the dashed line represents the background parameterisation only.

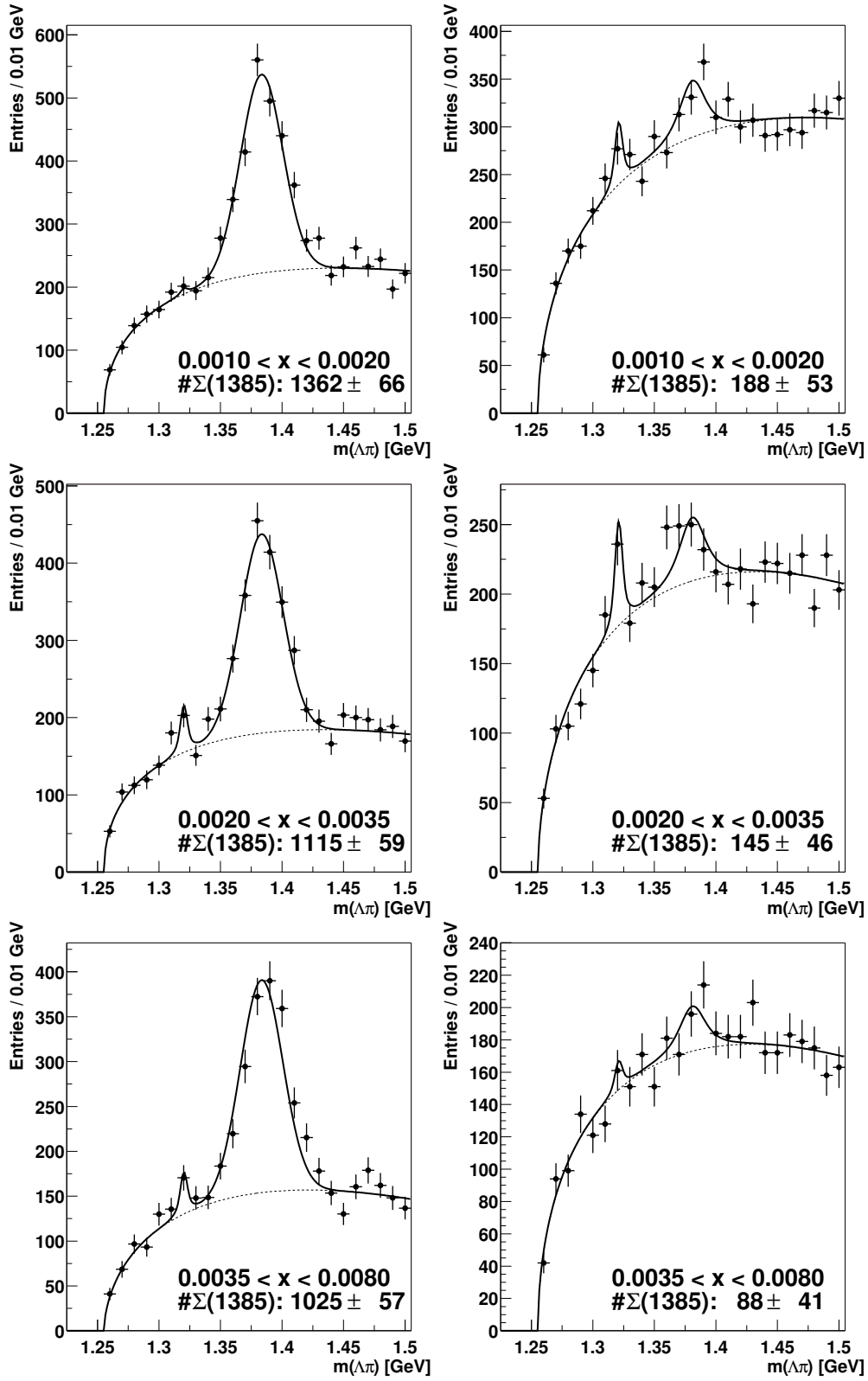

Figure A.6: Mass distribution $m(\Lambda\pi)$ in bins of x for Σ–MC (left) and data (right). The full line describes the parameterisation which is found by the fit (Eq. 5.4), the dashed line represents the background parameterisation only.

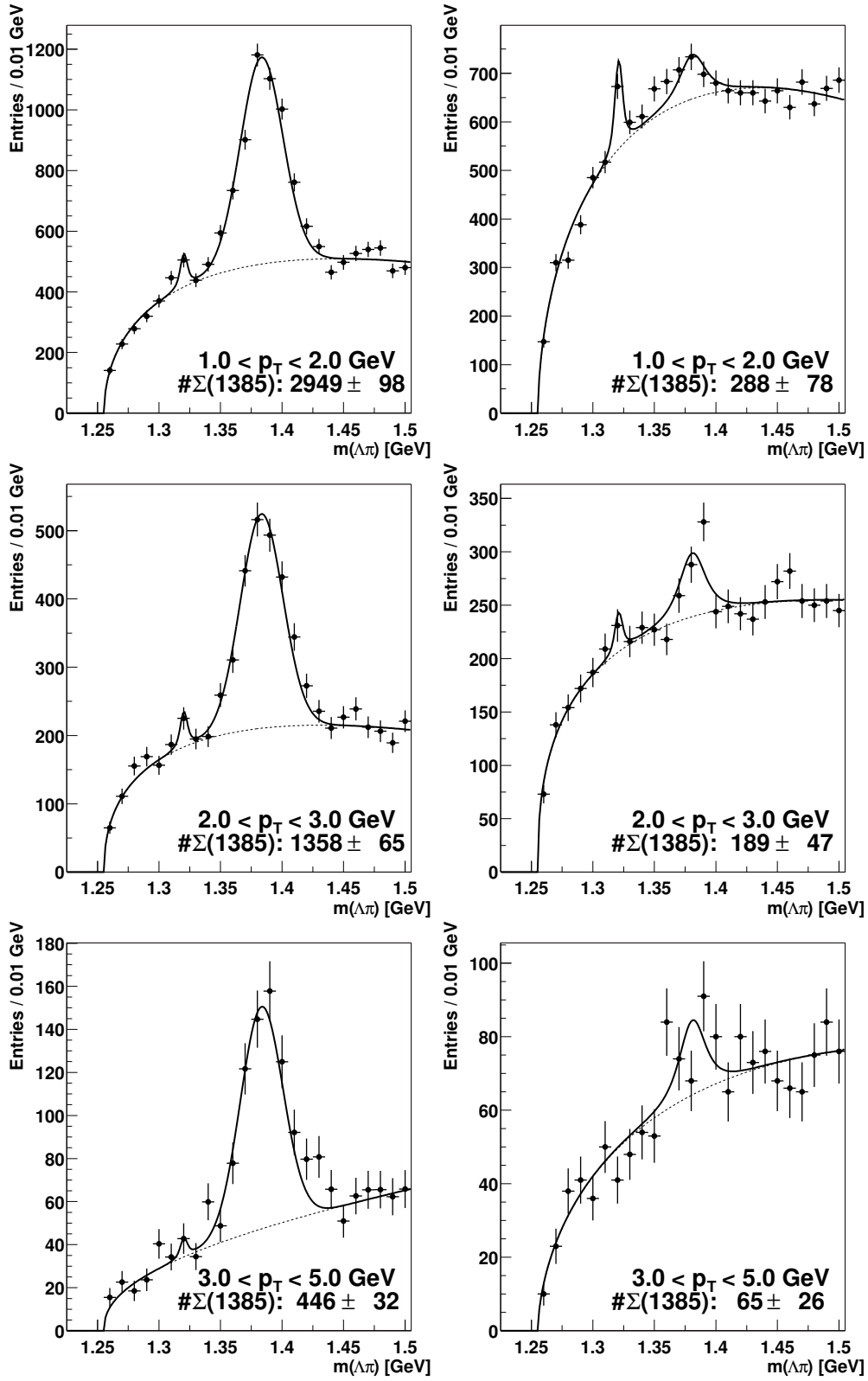

Figure A.7: Mass distribution $m(\Lambda\pi)$ in bins of $p_T(\Sigma\,(1385))$ for Σ–MC (left) and data (right). The full line describes the parameterisation which is found by the fit (Eq. 5.4), the dashed line represents the background parameterisation only.

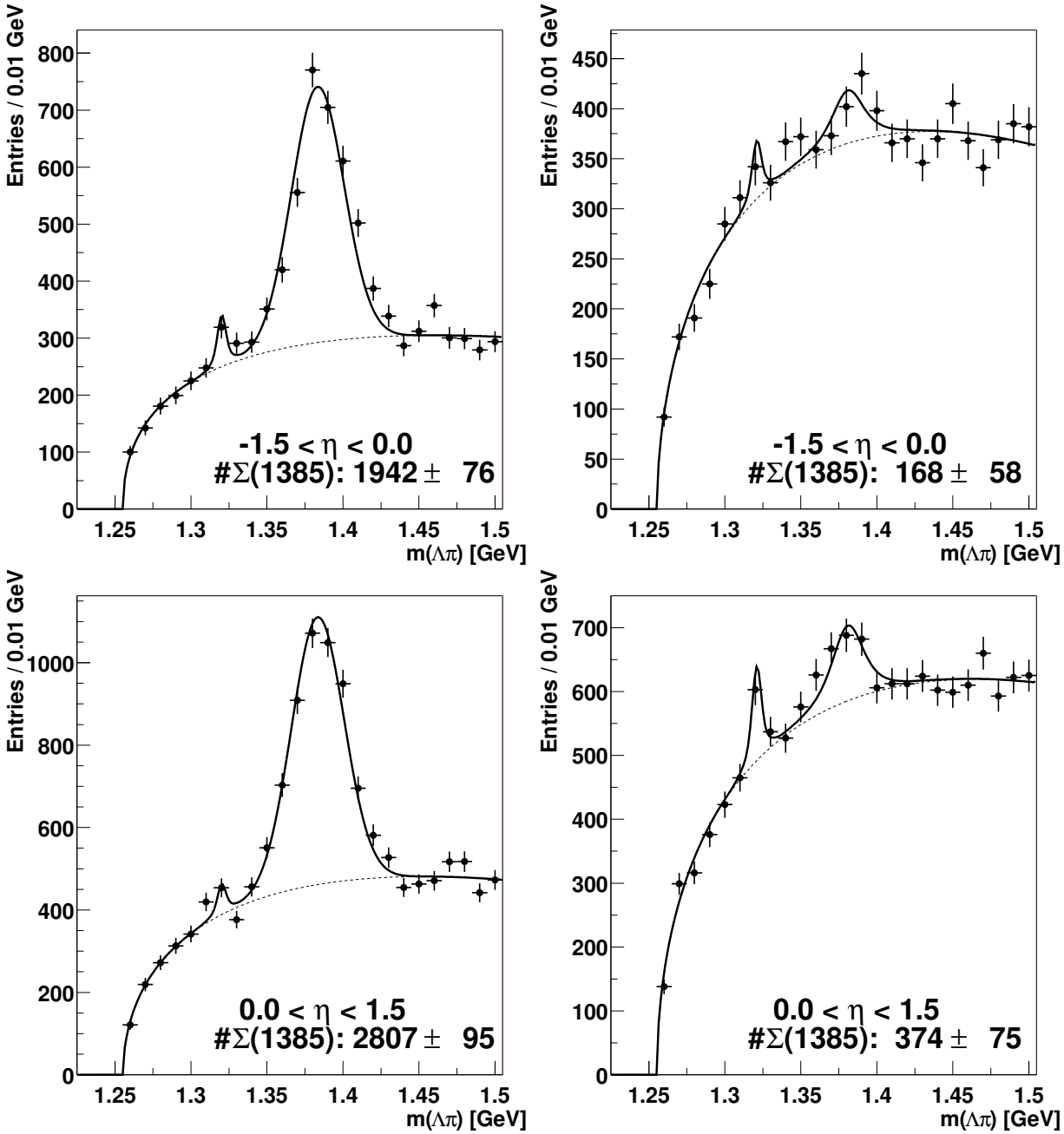

Figure A.8: Mass distribution $m(\Lambda\pi)$ in bins of $\eta(\Sigma\,(1385))$ for Σ–MC (left) and data (right). The full line describes the parameterisation which is found by the fit (Eq. 5.4), the dashed line represents the background parameterisation only.

Bibliography

[1] H. Abramowicz, A. Caldwell, R. Sinkus. Neural network based electron identification in the ZEUS calorimeter. *Nucl. Instrum. Meth.*, **A365**:508–517, 1995.

[2] ALEPH Collaboration (D. Buskulic *et al.*). Inclusive production of neutral vector mesons in hadronic Z decays. *Z. Phys.*, **C69**:379–392, 1996.

[3] B. Andersson, G. Gustafson, G. Ingelman and T. Sjöstrand. Parton fragmentation and string dynamics. *Phys. Rep.*, **97**:31, 1983.

[4] B. Andersson, G. Gustafson, T. Sjöstrand. Baryon Production in Jet Fragmentation and Υ-Decay. *Physica Scripta*, page 574, 1985.

[5] B. Andersson, G. Gustavson, L. Lönnblad, U. Petterson. Coherence effects in deep inelastic scattering. *Z. Phys.*, **C43**:625–632, 1989.

[6] J. Andruszków *et al.* (ZEUS Luminosity Group). Luminosity Measurement in the ZEUS Experiment, DESY-Note 01-041, DESY, Hamburg, 2001.

[7] P.S. Bailey, B. Foster, G.P. Heath, *et al.* The design and perfomance of the ZEUS central tracking detector z-by-timing system. *Nucl. Instrum. Methods*, **A396**:320–349, 1997.

[8] A. Bamberger *et al.* (ZEUS SRTD Group). The small angle rear tracking detector of ZEUS. *Nucl. Instrum. Methods*, **A401**:63–80, 1997.

[9] S. Bentvelsen, J. Engelen, P. Kooijman. Reconstruction of (x, Q^2) and extraction of structure functions in neutral current scattering at HERA. *Physics at HERA Proc.*, **1**:23–41, DESY, 1991.

[10] H. Bethe, W. Heitler. On the stopping of fast particles and on the creation of positive electrons. *Proc. Roy. Soc. Lond.*, **A146**:83–112, 1934.

[11] B.J. Bjorken and E.A. Paschos. Inelastic electron-proton and γ-proton scattering and the structure of the nucleon. *Phys. Rev.*, **185**:1975–1982, 1969.

[12] A. Blondel, F. Jacquet. *Proceedings of the Study of an ep Facility for Europe*, 1979. DESY-79-048.

[13] R. Brun *et al.* GEANT3, CERN DD/EE/84-1.

[14] S. Chekanov, B. Levchenko, J. Repond. Inclusive $\phi(1020)$-meson production in neutral current deep inelastic scattering at HERA, Internal ZEUS-Note 01-047, DESY, Hamburg, 2001.

[15] G. Corcella *et al.* HERWIG 6.1 Release note. *CAVENDISH-HEP-99-17*, 1999. hep-ph/9912396.

[16] DELPHI Collaboration (P. Abreu *et al.*). Measurement of inclusive $K^{\star 0}(892), \phi(1020)$ and $K_2^{\star 0}(1430)$ production in hadronic Z decays. *Z. Phys.*, **C73**:61–72, 1996.

[17] M. Glück, E. Reya and A. Vogt. Dynamical parton distributions revisited. *Eur. Phys. J.*, **C5**:461–470, 1998.

[18] H1 Collaboratin (C. Adloff *et al.*). Measurement of $D^{*\pm}$ Meson Production and F_2^c in Deep-Inelastic Scattering at HERA. *Phys. Lett.*, **B528**:199, 2002.

[19] H1 Collaboration (C. Adloff *et al.*). Photoproduction of K^0 and Λ at HERA and a Comparision with Deep Inelastic Scattering. *Z. Phys.*, **C76**:213–221, 1997.

[20] H1 Collaboration (S. Aid *et al.*). Strangeness production in deep-inelastic positron-proton scattering at HERA. *Nucl. Phys.*, **B480**:3–34, 1996.

[21] R. Hall-Wilton, N. McCubbin, *et al.* The CTD tracking resolution, Internal ZEUS-Note 99-027, DESY, Hamburg, 1999.

[22] G.F. Hartner. VCTRAK briefing: Program and math., Internal ZEUS-Note 98-058, DESY, Hamburg, 1998.

[23] G.F. Hartner, Y. Iga, J.B. Lane, N.A. McCubbin. VCTRACK (3.07/04): Offline Output Information, Internal ZEUS-Note 97-064, DESY, Hamburg, 1997.

[24] G. Ingelman *et al.* LEPTO. *Comp. Phys. Comm.*, **101**:108, 1997.

[25] A. Kwiatkowski *et al.* HERACLES 4.5.2. *Comp. Phys. Comm.*, **69**:155, 1992.

[26] H.L. Lai *et al.* Global QCD analysis of parton structure of the nucleon: CTEQ5 parton distributions. *Eur. Phys. J.*, **C12**:375–392, 2000.

[27] L. Lönnblad. ARIADNE. *Comp. Phys. Comm.*, **71**:15, 1992.

[28] G. Marchesini and B.R. Webber. Monte carlo simulation of general hard processes with coherent QCD radiation. *Nucl. Phys.*, **B310**:461, 1988.

[29] G. Marchesini *et al.* HERWIG: a monte carlo event generator for simulating hadron emission reactions with interfering gluons. *Comp. Phys. Comm.*, **67**:465, 1992.

[30] A.D. Martin, R.G. Roberts, W.J. Stirling, R.S. Thorne. Parton distributions: A new global analysis. *Eur. Phys. J.*, **C4**:463–496, 1998.

[31] A.D. Martin, R.G. Roberts, W.J. Stirling, R.S. Thorne. MRST2001: partons and α_S from precise deep inelastic scattering and Tevatron jet data, CERN-TH/2001-273, hep-ph/0110215.

[32] OPAL Collaboration (G. Alexander *et al.*). Strange baryon production in hadronic Z^0 decays. *Z. Phys.*, **C73**:569–585, 1997.

[33] OPAL Collaboration (P.D. Acton *et al.*). Inclusive neutral vector meson production in hadronic Z^0 decays. *Z. Phys.*, **C56**:521–535, 1992.

[34] Particle Data Group (D.E. Groom *et al.)*. Review of particle physics. *Eur. Phys. J.*, **C15**:1, 2000. and 2001 partial update for edition 2002 (URL:http://pdg.lbl.gov).

[35] F. Pelucchi. Λ^0 production in DIS events, Internal ZEUS-Note 99-031, DESY, Hamburg, 1999.

[36] T. Sjöstrand. Pythia 5.7 and Jetset 7.4 : Physics and Manual, CERN-TH. 7112/93, CERN, Geneva, 1993.

[37] H. Spiesberger *et al.* http://www.desy.de/∼hspiesb/djangoh.html.

[38] G. Wolf. HERA physics, In *High Energy Phenomenology*, Proceedings of the 42^{nd} Scottish Universities Summer School in Physics (St. Andrews, 1993), K.J. Peach and L.L.J. Vicks (Eds.), Institute of Physics, Philadelphia 1994, pp. 135–224, DESY-94-022.

[39] ZEUS Collaboratin (J. Breitweg *et al.*). Measurement of $D^{*\pm}$ production and the charm contribution to F_2 in deep inelastic scattering at HERA. *Eur. Phys. J.*, **C12**:53–68, 2000.

[40] ZEUS Collaboratin (J. Breitweg *et al.*). Measurement of open beauty production in photoproduction at HERA. *Eur. Phys. J.*, **C18**:625–637, 2001.

[41] ZEUS Collaboratin (M. Derrick *et al.*). Comparison of energy flows in deep inelastic scattering events with and without a large rapidity gap. *Phys. Lett.*, **B338**:483–496, 1994.

[42] ZEUS Collaboration (J. Breitweg *et al.*). Charged particles and neutral kaons in photoproduced jets at HERA. *Eur. Phys. J.*, **C2**:77–93, 1998.

[43] ZEUS Collaboration (M. Derrick *et al.*). Neutral Strange Particle Production in Deep Inelastic Scattering at HERA. *Z. Phys.*, **C68**:29–42, 1995.

[44] ZEUS Collaboration (S. Chekanov *et al.*). Measurement of the neutral current cross section and F_2 structure function for deep inelastic e^+p scattering at HERA. *Eur. Phys. J.*, **C21**:443–471, 2001.

[45] ZEUS Collaboration (S. Chekanov *et al.*). A ZEUS next-to-leading-order QCD analysis of data on deep inelastic scattering, DESY-Note 02-112, DESY, Hamburg, 2002, to be submitted to Phys. Review D.

[46] ZEUS Collaboration (U. Holm (Ed.)). The ZEUS Detector : Status Report 1993, DESY, Hamburg, 1993.